Characterization of Laser Light Propagation in Fibers using Optical Correlation Filters

Dissertation

zur Erlangung des akademischen Grades
doctor rerum naturalium (Dr. rer. nat.)

vorgelegt dem Rat der Physikalisch-Astronomischen Fakultät der Friedrich-Schiller-Universität Jena

von Robert Brüning, M.Sc.
geboren am 10.08.1988 in Jena.

Gutachter

1. Prof. Dr. Richard Kowarschik
   (Institut für Angewandte Optik,
   Friedrich-Schiller-Universität Jena)
2. Prof. Dr. Hartmut Bartelt
   (Leibniz-Institut für Photonische Technologien, Jena)
3. Prof. Dr. Axel Schülzgen
   (CREOL, The College of Optics & Photonics,
   University of Central Florida)

Tag der Disputation: 30. August 2017

Zusammenfassung

Die Möglichkeit, Licht nahezu verlustfrei auf kleinen Raum zu führen, macht optische Fasern heutzutage zu einer zentralen Schlüsseltechnologie mit vielfältigen Anwendungen in Bereichen wie Lichterzeugung, Telekommunikation oder Sensorik. Wurden zu Beginn monomodige Systeme bevorzugt, werden diese zunehmend durch multimodige Fasern ersetzt, um die steigenden Ansprüche an die Leistungsfähigkeit solcher Systeme zu erfüllen und insbesondere Einschränkungen durch nicht-lineare Effekte zu umgehen. Die sich daraus ergebende Möglichkeit des gleichzeitigen Führens von mehreren individuellen räumlichen Strahlungsverteilungen bringt - je nach Anwendung - positive oder negative Effekte mit sich. Für Faserlaser oder Faserverstärker ist das Auftreten von höheren Moden unerwünscht, da diese zu einer Verschlechterung der Stahlqualität führen. Anders sieht es im Bereich der Telekommunikation aus, hier ermöglicht die Nutzung von höheren Moden eine Steigerung der übertragbaren Datenmenge durch die zusätzliche Parallelisierung von Datenkanälen innerhalb einer Faser.

In beiden Fällen ist das Verständnis der modalen Übertragungseigenschaften von Licht in multimodalen Fasern von wesentlicher Bedeutung für zukünftige Entwicklungen, weshalb zuverlässige modenauflösende Charakterisierungsmethoden benötigt werden. Aus dieser Motivation heraus wurde eine Vielzahl von Ansätzen vorgeschlagen. Einer der potentiell vielseitigsten Ansätze ist die Korrelationsfiltermethode, welche die Grundlage dieser Arbeit bildet. Als erstes wurden dabei die gegebenen Möglichkeiten des etablierten Konzeptes zur Bestimmung der Übertragungseigenschaften von Fasern ausgenutzt und die erzielten Ergebnisse erfolgreich zur Kompensation von Übertragungseffekten angewandt. Zusätzlich wurde der Übergang zwischen Freistrahl- und Fasermoden beim Ein- und Auskoppeln von Licht in Fasern untersucht. Die daraus resultierenden Ergebnisse führten schließlich zur erstmaligen Realisierung eines passiv kombinierten Faser-Freiraum Kommunikationskanals, in dem mittels modalem Miltiplexings Daten übertragen werden konnten.

Ein weiterere wesentlicher Fokus dieser Arbeit lag auf der Überwindung von konzeptionellen Einschränkungen der existierenden Korrelationsfiltermethode.

Dabei wurde im ersten Schritt die Methode auf den allgemeineren Fall von partiell kohärenten Faserstrahlen erweitert. Dafür wurden zusätzliche Filterfunktionen zur Bestimmung des modalen Interferenzverhaltens eingeführt und das Auswerteverfahren entsprechend modifiziert. Dies ermöglichte neben der Zerlegung von partiell kohärenten modalen Überlagerungen auch die Untersuchung des Einflusses von Übertragungseffekten wie modaler Dispersion oder Modenkopplung auf die Kohärenzeigenschaften von Faserstrahlen. So konnte die Kohärenzlänge zwischen zwei verschiedenen Modengruppen bestimmt und eine Steigerung des Kohärenzgrades durch Modenkopplung nachgewiesen werden.

Eine weiter wesentliche Erweiterung der Korrelationsfiltermethode konnte erzielt werden durch die Implementation von Vektormoden in den Korrelationsfilter und die daraus resultierende Möglichkeit Faserstrahlen in ihren natürlichen Modensatz zu zerlegen. Dieser ist charakterisiert durch Moden mit räumlich inhomogenen Polarisationsverteilungen, welche mittels der üblicherweise genutzten computergenerierten Hologramme nicht adressierbar waren. Durch den Einsatz spezieller inhomogen anisotroper Phasenplatten, sogenannter q-plates, konnte diese Einschränkung überwunden und die Korrelationsfiltermethode auf hybride Fasermoden verallgemeinert werden. Die Leistungsfähigkeit des erweiterten Ansatzes konnte bei der Bestimmung der Übertragungseigenschaften einer speziellen Vortex-Faser demonstriert werden. Insbesondere war es möglich, die für vielfältige Anwendungen nützlichen, radial polarisierten Feldverteilungen mit verschiedener radialer Ordnung zu unterscheiden und aufzuzeigen, dass lediglich der radial polarisierte Mod niederer Ordnung störungsfrei übertragen werden kann.

Die genannten Ergebnisse der Arbeiten zeigen, dass die Korrelationsfiltermethode erfolgreich zur Charakterisierung von modalen Übertragungseigenschaften von komplizierten optischen Fasern angewandt werden kann. Zudem war es möglich durch Anpassung der Art der Filterfunktionen sowie deren Implementation als Filterelement das prinzipielle Messkonzept auf beliebige quasimonochromatische Faserstrahlen zu erweitern. Dies unterstreicht insbesondere den universelle Charakter der Korrelationsfiltermethode, was diese anderen, meist auf spezielle Fälle beschränkte Methoden, überlegen macht.

Contents

1 Introduction **3**

2 Mode Analysis **7**

2.1 Modal Description of Optical Fields 8

2.1.1 Hybrid Modes in Optical Fibers 9

2.1.2 Linearly Polarized Fiber Modes 12

2.2 Creation of Modes 16

2.2.1 Extra-Cavity Beam Shaping 16

2.2.2 Intra-Cavity Beam Shaping 18

2.3 Modal Decomposition 19

2.3.1 Modal Decomposition Techniques 20

2.3.2 Optical Correlation Analysis 22

2.3.3 Holographic Techniques 24

2.3.4 Modal Stokes Measurement 27

3 Decomposition into Linear Polarized Fiber Modes **31**

3.1 Fiber Mode Analysis 31

3.1.1 Reconstruction of Fiber Beams 32

3.1.2 Measurment of the Fiber Transmission Matrix 34

3.2 Mode System Matching 39

3.2.1 Scale Depending Overlap 40

3.2.2 Excitation of LP Fiber Modes by a Digital Laser 47

3.3 Combined Free-Space Fiber Communication Link 52

3.3.1 Properties of Gradient Index Fiber Links 53

3.3.2 Data Transmission through a Free-Space to Fiber Communication Link 56

4 Modal Decomposition of Partial Coherent Optical Fields **61**
4.1 Partial Coherent Superposition 61
4.1.1 Multi-Mode Interference 62
4.1.2 Determination of the Degree of Coherence 63
4.2 Experimental Results 66
4.2.1 Reconstruction of Partial Coherent Superpositions 66
4.2.2 Determination of Modal Coherence Length 69
4.2.3 Mode Coupling Induced Change of Coherence 72

5 Decomposition into Hybride Fiber Modes **77**
5.1 Vector Modes of a Vortex Fiber 78
5.2 Creation and Detection of Vector Modes 81
5.2.1 Vectorial Manipulation with Q-Plates 82
5.2.2 Vectorial Beam Shaping 86
5.2.3 Vectorial Correlation Analysis 89
5.3 Vector Mode Transmission Matrix 91
5.3.1 Measurement Procedure 91
5.3.2 Determination of Modal Transmission Purity 93

6 Conclusion **99**

1 Introduction

Nowadays optical fibers represent one of the worlds key technologies by enabling stable and flexible transmission and control of light. Beyond doubt, the intercontinental communication network built by more than 1 billion kilometers of optical fibers has made possible the triumph of the Internet [1]. Besides this global application, a plethora of fiber based technologies has entered nearly all fields of optics. The present applications include efficient light sources like fiber lasers [2], supercontinuum sources [3], optical sensors [4–6], different types of fiber-based imaging techniques [7] and platforms for experimental quantum physics [8], to name only a few. In order to meet the required demands for the different applications, a variety of fiber concepts has been designed and manufactured, offering the adjustment of fiber parameters like dispersion, the number of supported eigenstates, or propagation and bending losses. The existing fiber architectures are ranging from conventional step-index [9], graded-index [10], to sophisticated micro-structured designs like multicore [11] or photonic-crystal fibers [12,13].

For many fiber applications an important feature is the high beam quality delivered from so called single-mode fibers, where only a Gaussian-like field distribution is guided, allowing for high coupling efficiencies and nearly diffraction limited output beams. However, in the last decade, multi-mode fibers which support a certain number of higher-order transverse eigenfunctions, called "modes", were frequently applied in the field of high-power fiber lasers [14] and fiber optical communication [15,16], to overcome nonlinear limitations. In the latter field, the parallelization of independent data channels in multi-mode fibers offers a promising solution to ensure a further increase in data capacity per single fiber [17–20]. In contrast, for the development of high power fiber lasers and amplifiers, unwanted multi-mode interferences are currently the main limiting factor [21–24] due to an associated degradation of the spatial beam quality.

These two prominent examples emphasize the importance of a reliable modally resolved analysis tool for the determination of the fiber's modal transmission properties. To tackle this problem, a plethora of modal characterization techniques were proposed in literature. One of the most universal approaches is the correlation filter method [25] which was proven to be excellently suited for the modal resolved investigation of optical systems due to its wide and general applicability [26–30]. Thus, this thesis will be based on the underlying concept of an optical correlation analysis. Consequently, the first goal of this thesis is to make use of the existing abilities to investigate light propagation in fibers and combined fiber–free-space systems. A special focus is directed to the intersection point between fiber and free-space propagation with respect to their different sets of eigenfunctions and their interrelation. In order to realize an effective and selective interconnection the mode matching problem between both system has to be solved. To address this problem, two solutions are outlined: first the scale adaptation of the free-space mode set, and second the usage of a gradient index fiber with a specific parabolic index distribution. This leads finally to the first realization of a passively combined fiber–free-space communication link for mode division multiplexing. A second objective of this thesis is to overcome restrictions regarding the optical fields that can be investigated and thus to remove limitations of the applicability caused by the practical realizations of the state of the art correlation filter method. In particular, the established experimental implementation is restricted to coherent or incoherent modal superpositions only. To overcome this limitation, a novel scheme for the modal interference measurement and evaluation will be introduced which allows the decomposition and reconstruction of fields without any restrictions regarding their degree of coherence. Hence, this modification yields access to the exploration of the general class of partially coherent light fields and to associated propagation effects like modal dispersion by the advanced version of the correlation filter method. A second fundamental limitation occurs regarding the mode sets that could be investigated, which were limited to scalar mode sets only by the ability of the applied filter elements to encode only amplitude and phase information. Although, these types of modes are

very good approximations for waveguides with a small refractive index contrast, for the characterization of light propagation in arbitrary fibers, the decomposition into vectorial modes requieres the natural fiber modes. To address these generalized type of modes, a modification of the used filter elements is performed by introducing special non-uniform anisotropic wave plates which allow the additional implementation of spatial varying polarization information into the filter element. Thus, the characterization of fiber beams using the correlation filter method becomes possible for the first time in terms of their natural mode set and without any limiting assumptions regarding the fiber guidance. The versatility of the new capabilities is proven by the investigation of fiber propagation properties which were not accessible before and should be invaluable for the modal characterization of fiber beams under generalized optical conditions.

To reach the outlined objectives, in Ch. 2 the concept of modes will be introduced in detail, whereby their fundamental properties are discussed. Additionally, the actual state of the art techniques for beam shaping and modal decomposition using computer generated holograms are presented with respect to the required coding techniques and their experimental realization. In Ch. 3, the correlation filter method is applied to decompose coherent modal superpositions in weakly guiding fibers and characterize their propagation and mode excitation properties. To overcome the restriction of complete coherent conditions, a modified version of the correlation filter method will be established in Ch. 4, which allows the decomposition of partially coherent fiber beams. Furthermore, that extended capability is used to investigate the effect of modal dispersion during propagation on the degree of coherence. The approximation of linear polarized modes will be overcome in Ch. 5 by adding special non-uniform anisotropic phase plates within the correlation filter setup which enables the modal decomposition in terms of the natural hybrid mode set of optical fibers. Finally, the new vectorial correlation filter method will be used to evaluate the transmission purity of vector modes propagating through a special, strong guiding, so called "vortex fiber".

2 | Mode Analysis

The dynamics of physical systems is typically described by characteristic partial differential equations. Special solutions of these equations are eigenfunctions, the so called "modes", which represent stationery solutions of the system and build an orthogonal and complete set of basis functions. For linear systems these modes can be combined to form all possible solutions by the superposition principle. These superimposed states are the general case, which can be found in experiments, and results in a spatial variation of the field properties. To characterize such a state, all properties have to be measured spatially resolved, which requires a large amount of discrete measurement points. Here the modal analysis provides a great advantage in cases of discrete mode spectra, which typically arise for limited boundary conditions. In these cases the information of the spatial distribution of a physical property can be represented by the expansion coefficients of the modal superposition and results in a tremendous reduction of the required data, which has to be measured, by substituting the two- or three-dimensional field problem by the one dimensional mode analysis problem. Another advantage of the mode picture can be found by the theoretical modeling of physical systems. For that, the application of a one-time determined evolution matrix onto mode resolved initial states yields the resulting mode spectra and thus the final states for each possible initial state, instead of calculating each individual evolution.

Particularly in optics the mode picture is beneficial, since discrete modes can be found in many cases like paraxial laser beams and resonators or optical waveguides and fibers, to note only a few. By this reason the mode picture for optical fibers will be introduced in the following chapter. For that, a short overview about the existing mode sets in optics will be given in Sec. 2.1 followed by a detailed introduction of the mode sets of radially symmetric optical fibers in Sec. 2.1.1 pp. 9 and Sec. 2.1.2 pp. 12 for the general vectorial case and under consideration of a

scalar approximation, respectively. Afterwards two experimental methods for the generation of pure modal states as well as for arbitrary modal superpositions will be outlined in Sec. 2.2 pp. 16. Finally the working principle of the applied modal analysis technique, the correlation filter method, will be discussed in detail regarding the theoretical background and the experimental realization.

2.1 Modal Description of Optical Fields

In optics the characteristic equation describing the evolution of optical fields in time and space is the wave equation, which derives from the Maxwell-equations [31]. Depending on the refractive index distribution (which acts as a potential function) the used coordinate system, or additional applied approximations, different types of mode sets can be found. In the simplest case of a homogeneous, isotropic medium such as a vacuum and the usage of Cartesian coordinates the eigenfunctions of the wave-equation are the well known plane waves, which form a continuous and infinite mode set [32]. From the physical point of view, these modes are not realizable due to the infinite spatial extension and amount of energy contained in each plane wave and thus forms only a mathematical solution. However, for the theoretical description of simple optical systems and for the approximation within a limited spatial region, they are commonly applied. However, by suitable superpositions of plane wave spectra, physical field distributions can also be constructed. The analog problem occurs for the description in cylindrical coordinates, where the famous non-diffracting Bessel-beams occur as the solutions of the wave-equation [33]. By restricting the main propagation direction of the light, as done by the paraxial approximation, a set of physical realizable modes can be found, which are the Hermit-Gaussian [31], Laguerre-Gaussian [31] or Inc-Gaussian modes [34] in Cartesian, cylindrical or elliptical coordinates, respectively. Besides the finite amount of energy contained in each mode, a second benefit of this mode set is its discrete nature. However, the amount of possible modes is still infinite and has to be restricted for practical application. Here, commonly modes of increasing order will be considered until the used modes

represent a certain power ratio of the beam, e.g. 98%. In laser resonators with intra-cavity elements, which prescribe the respective symmetry, these mode sets are in good approximation realizable. The amount of oscillating modes in such resonators is typically limited by gain competition and an increasing lase threshold due to diffraction losses at finite sized resonator elements [31]. Another well known example of systems with a discrete and finite mode set are optical fibers, where an inhomogeneous refractive index distribution confines the propagating light within a certain plane transverse to the propagation direction [35]. Additionally, only a limited amount of modes is required to describe all possible guided light fields due to the finite refractive index contrast, which confines the light. Hence, for the description of optical fiber beams the mode picture is well suited for the reduction of the degrees of freedom which are required for the complete description of emerging beams.

In the following section, two types of solutions for mode sets occurring in an optical fibers will be outlined. At first the exact vectorial solution of the wave-equation will be discussed and example modes of a step index fiber are shown. Afterwards the weak guidance approximation will be introduced leading to the commonly used linearly polarized fiber modes and the interrelation of both mode sets is demonstrated.

2.1.1 Hybrid Modes in Optical Fibers

Optical fields in general are represented by a time dependent electric vector field $\hat{\mathbf{E}}(\mathbf{r}, t)$ and a magnetic vector field $\hat{\mathbf{H}}(\mathbf{r}, t)$, which can be described by the Maxwell's equations. For the modeling of confined light fields in optical fibers under monochromatic conditions a harmonic dependency of the electromagnetic wave in propagation direction z and time t is assumed [36,37]:

$$\hat{\mathbf{E}}(\mathbf{r}, t) = \mathbf{E}(\mathbf{r}_t) \exp[i(\beta z - \omega t)], \tag{2.1}$$

$$\hat{\mathbf{H}}(\mathbf{r}, t) = \mathbf{H}(\mathbf{r}_t) \exp[i(\beta z - \omega t)], \tag{2.2}$$

with $\beta = k_z = \mathbf{k}\cdot\mathbf{e}_z$ the z component of the wave vector, ω the angular frequency of light, $\mathbf{r} = (x, y, z)$ the spatial coordinate and $\mathbf{r}_t = (x, y, 0)$ its transverse projection. Considering the optical (glass) fiber as non-magnetic and without free charges or currents leads to the vectorial wave equation for the transverse magnetic field components, which takes the form [36, 37]:

$$\left\{\nabla_t^2 + k^2\epsilon(\mathbf{r}_t) + [\nabla_t \ln\epsilon(\mathbf{r}_t)] \times \nabla_t \times\right\} \mathbf{H}_t(\mathbf{r}_t) = \beta^2 \mathbf{H}_t(\mathbf{r}_t), \tag{2.3}$$

where k is the absolute value of the wave vector $\mathbf{k}$, $\nabla_t = (\partial_x, \partial_y, 0)$ is the transverse Nabla operator and $\partial_j = \partial/\partial_j$ is the partial derivative. Here the relative permittivity distribution $\epsilon(\mathbf{r})$ presets the spatial distribution of the transverse magnetic field $\mathbf{H}_t(\mathbf{r}) = (H_x, H_y)$, which has to satisfy the coupled system of differential equations [36]

$$\left(\partial_x^2 + \partial_y^2 + \epsilon k^2\right) H_x + \left(\partial_x H_y - \partial_y H x\right) \partial_y \ln\epsilon = \beta^2 H_x, \tag{2.4}$$

$$\left(\partial_x^2 + \partial_y^2 + \epsilon k^2\right) H_y + \left(\partial_y H_x - \partial_x H y\right) \partial_x \ln\epsilon = \beta^2 H_y. \tag{2.5}$$

From those calculated transverse magnetic field components (H_x, H_y) the complete electromagnetic field vector is determinable. The longitudinal i.e. z-component of the magnetic field follows from the solenoidality of the magnetic field $\nabla \cdot \mathbf{H}(\mathbf{r}) = 0$ by

$$H_z = (i\beta)^{-1} \left(\partial_x H_x + \partial_y H_y\right). \tag{2.6}$$

Finally the electric field vector can be obtained using the Maxwell-Faraday's equation and takes the form

$$\mathbf{E}(\mathbf{r}) = [-i\omega\epsilon_0\epsilon(\mathbf{r})]^{-1} \nabla \times \mathbf{H}(\mathbf{r}), \tag{2.7}$$

with ϵ_0 as vacuum permittivity. Since the operator on the left hand side of the eigenvalue problem Eq. (2.3) is Hermitian [37], the resulting modes fulfill the

general orthogonality relation of forward propagating waveguide modes [35]

$$\iint\limits_{\mathbb{R}^2} \mathrm{d}^2\mathbf{r}\,(\mathbf{E}_m^* \times \mathbf{H}_n) \cdot \mathbf{e}_z = \iint\limits_{\mathbb{R}^2} \mathrm{d}^2\mathbf{r}\left(E_{m,x}^* H_{n,y} - E_{m,y}^* H_{n,x}\right) = \delta_{mn}, \tag{2.8}$$

where "*" denotes complex conjugation, $\mathbf{e}_z$ is the unit vector in z-direction and $\mathrm{d}^2\mathbf{r}$ is the surface element. For modal vector fields $\mathbf{H}_n$ and $\mathbf{E}_n$ of the nth mode order normalized to unit power, the Kronecker symbol δ_{nm} can take the following two values

$$\delta_{nm} = \begin{cases} 1, & \text{if } m = n \\ 0, & \text{otherwise.} \end{cases} \tag{2.9}$$

The knowledge about all guided modes of a fiber enables the description of all possible field distributions following the superposition principle by weighted sums

$$\mathbf{E}(\mathbf{r}) = \sum_{n=0}^{n_{max}} c_n \begin{pmatrix} E_{n,x} \\ E_{n,y} \\ E_{n,z} \end{pmatrix} \qquad \text{and} \qquad \mathbf{H}(\mathbf{r}) = \sum_{n=0}^{n_{max}} c_n \begin{pmatrix} H_{n,x} \\ H_{n,y} \\ H_{n,z} \end{pmatrix}, \tag{2.10}$$

with n_{max} being the maximum number of modes and c_n the complex expansion coefficient.

Depending on the geometry of the underlying refractive index distribution, there are several techniques known to solve Eq. (2.4) and (2.5) allowing the determination of all six field components, by rigorous or numerical methods. A rigorous calculation for example is possible for the vector modes supported in step-index fibers [35, 38], which show a cylindrically symmetric refractive index distribution $n(\mathbf{r}) = n(\mathrm{r})$. In this special case the solution can be expressed by combinations of Bessel and Hankel basis functions [35, 38] and leads to solutions with six in general non-vanishing vector field components. The intensity distributions of the lowest order hybrid modes together with their spatial polarization distribution, marked by green arrows, are depicted in Fig. 2.1 of such a common step index

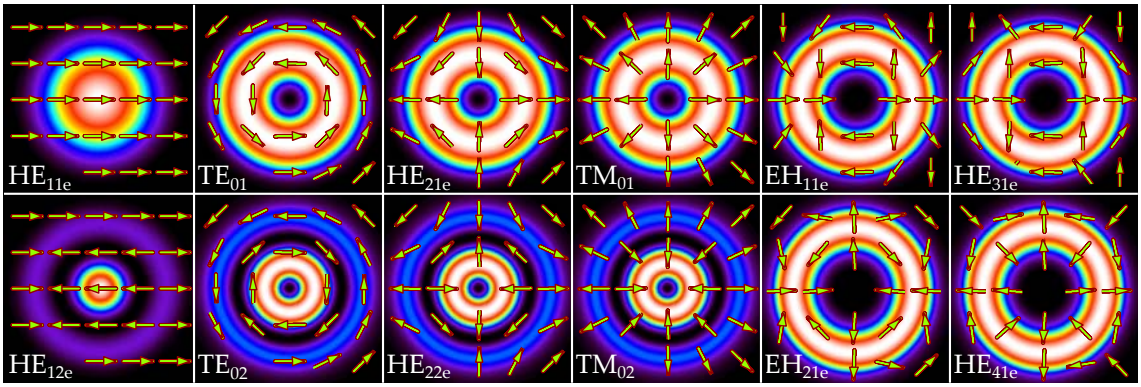

Figure 2.1: Intensity and polarization distributions of the lowest order hybrid modes of a step index fiber. In case of degenerated mode pairs only the even one is shown.

fiber. It can be seen that the fundamental mode HE_{11e} shows a typical Gaussian like intensity distribution and a spatially constant linear polarization state. For modes with non-zero azimuthal order, identifiable by the zero intensity on the optical axis, the polarization distribution becomes spatially varying, whereas the complexity of the polarization pattern increases with increasing mode order. For microstructured fibers like photonic crystal fibers [12] or multi-core fibers [39] the rigorous approach can be expanded for periodically arranged cylindrically symmetric holes or cores in a homogeneous background material [40, 41]. Numerical approaches such as finite differences [42] or finite elements methods [43,44] can be applied to solve Eq. (2.3) for arbitrary structured fibers and enable the calculation of all six corresponding vector components.

2.1.2 Linearly Polarized Fiber Modes

Although the hybrid mode set derived in the previous section represents in general the natural fiber modes, in many cases a simplification can be applied. This is the so called weakly guiding approximation, where the medium is assumed to be slowly varying with $\mathbf{r}$ or at least piecewise constant and ignoring any sudden change. In this case the derivative of the permittivity in Eq. (2.3) becomes $\nabla \ln \epsilon(\mathbf{r}) = 0$ and the coupled differential equations, Eq. (2.4) and Eq. (2.5), simplify

to the scalar wave equation

$$\left[\nabla_t^2 + k^2\epsilon(\mathbf{r}_t)\right]\psi(\mathbf{r}_t) = \beta^2\psi(\mathbf{r}_t), \tag{2.11}$$

where ∇_t is the transverse Nabla operator, k is the the absolute value of the wave vector $\mathbf{k}$ and β the propagation constant. Here, the scalar field ψ represents the transverse components of $\mathbf{H}$ and $\mathbf{E}$, equally. Following the reduction of the eigenvalue problem to scalar fields, the orthogonality relation given in Eq. (2.8) simplifies into

$$\iint_{\mathbb{R}^2} \mathrm{d}^2\mathbf{r}\psi_m^*\psi_n = \langle\psi_m|\psi_n\rangle = \delta_{mn}, \tag{2.12}$$

where "*" denotes complex conjugation, $\mathrm{d}^2\mathbf{r}$ is the surface element and ψ_n represents the nth-order mode, which can be identified as the component of the vector mode fields $E_{n,x}$ and $H_{m,y}$ respectively. For modal field distributions normalized to unit power, the Kronecker symbols δ_{nm} is defined as previously in Eq. (2.9).

Due to the completeness of the solution all optical field distributions can be composed by a linear superposition, similar to Eq. (2.10),

$$U(\mathbf{r}) = \sum_{n=0}^{n_{max}} c_n\psi_n, \tag{2.13}$$

where the complex expansion coefficient c_n is defined using the orthogonality relation given by Eq. (2.12),

$$c_n = \rho_n e^{i\Delta\varphi_n} = \langle\psi_n|U\rangle, \tag{2.14}$$

with ρ_n denoting the relative modal weights and $\Delta\varphi_n$ the inter-modal phase differences.

The most famous example of such a scalar mode set is given by the linear polarized (LP) modes of the step index fibers, which are completely defined by the core diameter d_{cor} and the numerical aperture $NA = \sqrt{n_{co}^2 - n_{cl}^2}$. In Fig. 2.2 the intensity and phase distributions of the lowest order LP modes are illustrated,

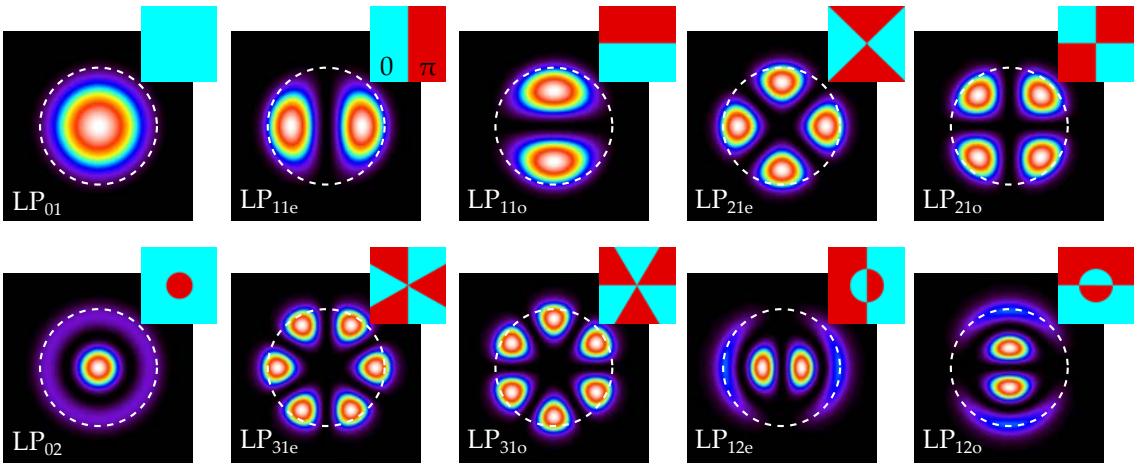

Figure 2.2: Intensity and Phase distribution of the ten lowest order LP modes of a typical step index fiber, the dashed circle marking the core to cladding boundary.

where the dashed circle denotes the core to cladding boundary. For this mode set the higher order azimuthal modes is twofold degenerated with respect to the cosine and sine solutions in cylindrically symmetric systems and are labeled as even and odd modes, respectively.

Despite the fact that the developed mode set itself is strictly scalar, it can be used to describe vectorial beams. For that two independent and degenerated solutions of the scalar Helmholtz equation, Eq. (2.11), and two orthogonal polarization states, e.g. vertical and horizontal polarized, have to be considered. Thus the superposition principle for vectorial fields leads to

$$\mathbf{U}(\mathbf{r}) = \sum_{n=0}^{n_{max}} \psi_n(\mathbf{r}) \begin{pmatrix} c_{n,x} \\ c_{n,y} \end{pmatrix} = \sum_{n=0}^{n_{max}} \psi_n(\mathbf{r}) \begin{pmatrix} \rho_{n,x} \\ \rho_{n,y} e^{i\delta_n} \end{pmatrix} e^{i\Delta\varphi_n}, \tag{2.15}$$

where the modal expansion coefficient c_n becomes a vector, with $c_{n,x}$ and $c_{n,y}$ describing the contribution of the horizontally and vertically polarized n-th order mode, respectively. Besides the individual modal weights for each component $\rho_{n,x}$ and $\rho_{n,y}$, and the inter-modal phase difference $\Delta\varphi_n$, an additional parameter δ_n, which describes the phase difference between the polarization components of the individual modes, has to be considered and is called intra-modal phase difference.

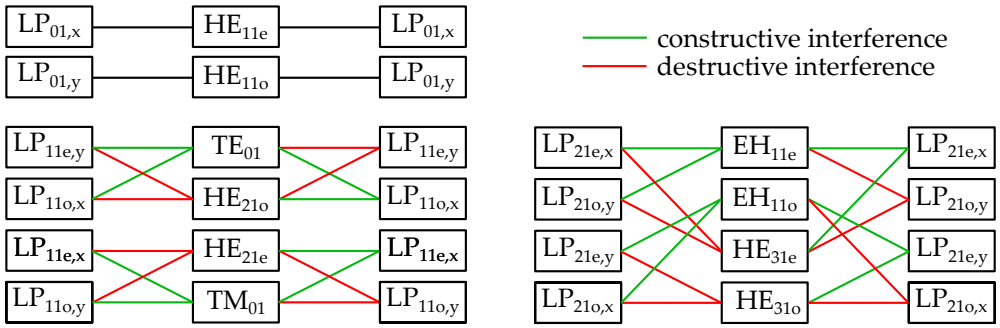

Figure 2.3: Interferometric relation between LP and hybrid modes to form the corresponding mode set, where the case of constructive interference is denoted by green lines and the case of destructive interference by red lines.

Using the vectorial expansion given by Eq. (2.15) of the LP modes, it is possible to rebuild the intensity and polarization distribution of the natural vector modes discussed in Sec. 2.1.1 in good approximation. For that, the even and odd LP mode solutions with different polarization directions have to be combined with a specific intra-modal phase difference. For example, the radially polarized TM_{01} mode results from the superposition of the LP_{11e} and the LP_{11o} polarized in x- and y-directions, respectively, with a phase difference of zero. Changing the intra-modal phase to π results in the hybrid mode HE_{21e}. This procedure works also in the other direction, where the LP modes can be constructed by a superposition of the hybrid modes. In that case the x-polarized LP_{11e} and the y-polarized LP_{11o} modes are formed by constructive and destructive interference, respectively, between the TM_{01} and the HE_{21e} modes. The corresponding modal superpositions to form the hybrid modes by the LP modes, and vise versa, are illustrated in Fig. 2.3 for the ten lowest order step-index fiber modes, where constructive and destructive interference refer to an intra-modal phase difference of 0 and π, respectively. The fundamental modes $LP_{01,x/y}$ and $HE_{11e/o}$, respectively, equal each other and no superposition is necessary to form the counterpart in the other mode set. It has to be noted that the z-component of the approximated hybrid mode set has to be calculated by the solenoidality of the electric field $\nabla \cdot \mathbf{E}(\mathbf{r}) = 0$, since in the LP mode set picture the z-component is not considered.

2.2 Creation of Modes

After discussing the appearance of discrete mode sets in optical fibers and their properties, the following section introduces two techniques for the generation of scalar mode fields or arbitrary coherent superpositions of them. At first a passive beam shaping method will be outlined, which enables the creation of the design field distribution out of a well known input beam. As a second technique, an intra-cavity beam shaping of a laser source is introduced, where a solid state laser cavity is actively forced to oscillate on the desired mode. Both methods rely on the usage of a liquid-crystal-on-silicon-based phase-only spatial light modulator in combination with special phase coding techniques, which are discussed as well.

2.2.1 Extra-Cavity Beam Shaping

A well established method to generate arbitrary optical field distributions from a known reference field are computer generated holograms (CGH). Since the during this thesis applied holographic techniques work either in amplitude- or phase-only regime a suitable encoding is required because the applied mode functions are in general complex valued (amplitude and phase). There are several phase-only [45–48] or amplitude-only [47,49,50] coding techniques known. The highest flexibility for the realization of the required holograms is given by digitally controllable spatial light modulators (SLM), where the phase value of the incoming field can be pixel-wise modulated. Hence, such devices are able to display phase-only holograms provided that an appropriate amplitude-to-phase coding procedure is applied.

For this the coding technique proposed by Arrizón et al. [48] was used, where a phase hologram $H(\mathbf{r}) = \exp[i\Psi(\mathbf{r})]$ encodes the complex valued functions $T(\mathbf{r}) = A(\mathbf{r})\exp[i\Phi]$, with $A \in [0,1]$ and $\Phi = [-\pi, \pi]$. Several phase modulation functions $\Psi(A, \Phi)$ were proposed in literature to provide the desired field information in a certain diffraction order. In this work a phase modulation of

$$\Psi(A, \Phi) = f(A)\sin(\Phi) \tag{2.16}$$

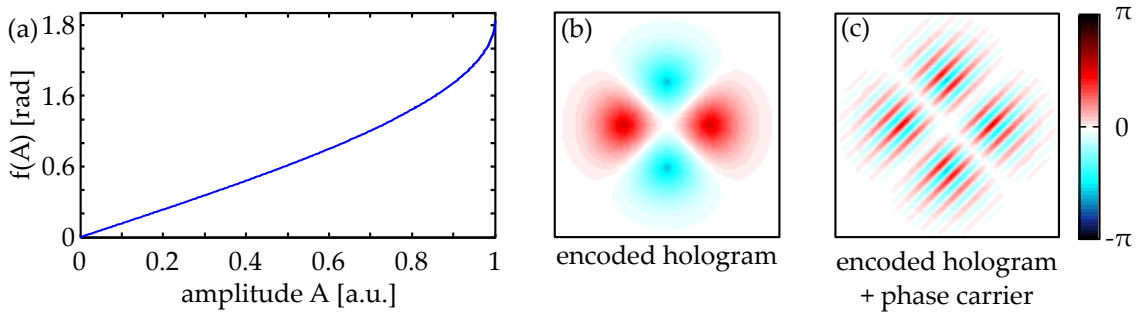

Figure 2.4: Coding principle of the phase-only coding technique; (a) amplitude function of Eq. (2.16), (b) the encoded transmission function and (c) the final hologram with additional sinusoidal phase grating.

was chosen [48], which generates the shaped field in the first order of diffraction. Using the Jacobi-Anger identity [51], the encoding condition is fulfilled if $f(A)$ is inverted from

$$J_1\left[f(A)\right] = a_0 A, \tag{2.17}$$

with J_1 being the first-order Bessel function and $a_0 = J_1^{max} \cong 0.58$. The exact dependency of $f(A)$ is depicted in Fig. 2.4 (a) and was numerically determined by using a line-search algorithm [48]. Using the once determined amplitude coding function $f(A)$ as a look-up table, it enables the calculation of the needed phase holograms in real-time. An example of a phase only encoded field distribution H using Eq. (2.16) of the LP_{21e} mode is shown in Fig. 2.4 (b). Throughout this work an additional sinusoidal phase grating was applied to separate the shaped field in the Fourier plane of the hologram from the undiffracted light and yielded the finally used holographic transmission function, which is depicted in Fig. 2.4 (c) for the example LP_{21e} mode. A side effect of the outlined coding technique is that only a restricted dynamic range of $\approx 1.2\pi < 2\pi$ is required for the phase modulation, enabling the manipulation of light at different wavelengths in cases where uncoated SLMs are used.

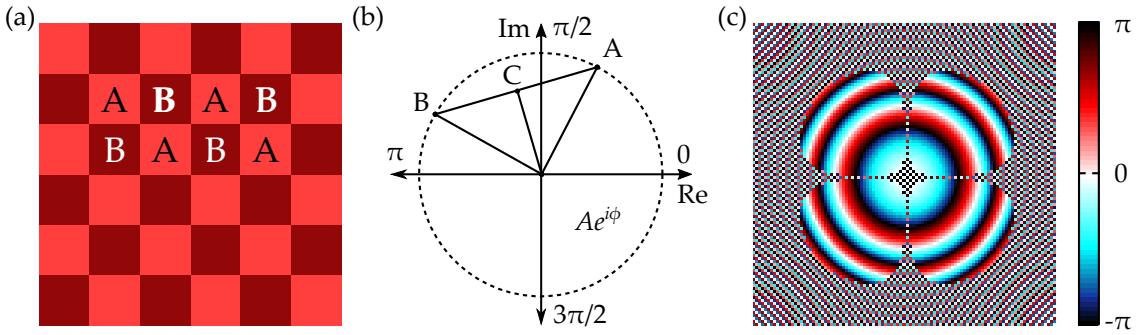

Figure 2.5: Working principle of the zero order coding technique; (a) Coded information will be represented by a checkerboard phase patter with values A and B, (b) the superposition of both creates an effective encoded value C, (c) shows an example of a coded hologram.

2.2.2 Intra-Cavity Beam Shaping

Besides the aforementioned approach of shaping optical beams out of a known incident field distribution, the direct creation of the desired modes out of a laser cavity is also possible. To do so, several design techniques are available [52–54] using customized optical elements to force the oscillating mode into the desired transverse field distribution. Successfully realized are approaches working in the phase-only [55–57], amplitude-only [58, 59] or phase-amplitude combination [60] regime. A high flexibility in the application of intra-cavity beam shaping can be achieved by the concept of the digital laser introduced by Ngcobo et al. [61], where one of the cavity mirrors is replaced by a reflective phase-only SLM working as a rewritable holographic mirror. Thus, an on-demand mode selection becomes possible by a dynamical adaption of the displayed phase function with respect to the wanted field distribution.

Since the applied SLM is restricted to phase-only modulation, similar to the free space case, an appropriate coding technique is required to manipulate also the amplitude distribution. For that, the on-axis coding technique proposed by Arrizón [62] is used, where a high spatial frequency modulation in the form of a checkerboard pattern carries the complex field information. An example of such a pattern is depicted in Fig. 2.5 (a) with the alternating phase values A and B. For the encoding of an arbitrary complex value $C = a_0 e^{i\phi}$ each hologram pixel consists of two neighboring SLM pixels, where the first pixel has the phase value

$A = e^{i(\phi-\alpha)}$ and the second $B = e^{i(\phi+\alpha)}$. Here ϕ is the mean phase value and 2α defines the modulation strength of the checkerboard pattern. Thus, the encoded complex value C results from the averaged field of both pixels

$$C = \frac{1}{2}\left(e^{i\phi-i\alpha} + e^{i\phi+i\alpha}\right) = e^{i\phi}\cos(\alpha), \tag{2.18}$$

with $\cos(\alpha) = a_0$ the encoded amplitude. Figure 2.5 (b) depicts a graphical illustration of this coding scheme. By a position dependent variation of this checkerboard pattern, the realization of complex field distributions becomes possible. For the selective creation of modes within the digital laser holograms, coded holograms like those depicted in Fig. 2.5 (c) for the LP_{21e} mode, are used. To achieve this, a phase modulation of π between neighboring pixels is applied to realize areas with zero amplitude in the on-axis reflection. Hence, artificial apertures and high loss lines corresponding to the zeros of the optical field are created. Accordingly, only the desired mode is able to oscillate above the laser threshold in the cavity and all other modes are suppressed by the additional introduction of high losses. The size of the resulting mode is controllable by adjusting the size of the aperture with respect to the phase curvature within this. By this procedure, a high flexibility in terms of addressable mode orders and beam sizes are possible directly from the light source itself without the need of additional passive beam shaping elements.

2.3 Modal Decomposition

After the introduction of beam shaping techniques for the generation of arbitrary optical fields in the previous section, in the following section the reverse direction of decomposing a beam into its underlying mode set will be discussed. For that, a short review and comparison of different modal analysis techniques will be given at first. Afterwards the correlation filter method, which is applied and further improved within this thesis, will be discussed in detail with respect to the theoretical working principle and the experimental realization.

2.3.1 Modal Decomposition Techniques

The great advantage of describing optical beams in terms of the underlying mode set is emphasized by the development of a plethora of different modal analysis techniques in the past. They all aim on the determination of the complex valued modal expansion coefficients or at least on the relative modal power content. For a first classification of the existing modal decomposition techniques, they can be divided in methods which require a priori information about the modal field distribution and those which do not. The latter kind typically relies on the propagation properties and especially in optical fibers on modal dispersion effects. The most widely used technique of this type is the spatially and spectrally resolved imaging techniques called S^2 imaging as proposed by Nicholson et al. [63]. For that, the modal interference in a broad wavelength range is spatially evaluated to reveal the modal strength and field distribution of higher order modes with respect to their different dispersion properties $\beta_n(\omega)$. Related techniques are cross-correlation (C^2-) imaging [64] or low-coherence interferometry [65]. The difference in the group or phase velocities of higher order modes can be exploited for modal decomposition by time of flight measurements applying a pulsed laser source [66] or by the usage of fiber gratings [67], respectively. Within the class of decomposition techniques that relay on the knowledge of the modal field distribution all numerical modal decomposition approaches can be found. Thereby the modal content is either obtained by numerical phase retrieval algorithms using intensity measurements [68–71] or by calculating the inner product relation from an interferometrically measured complex field distribution [72,73]. A direct determination of the modal coefficients is done by the correlation filter method, which optically performs the inner product relation between the laser beam and mode fields [25,74,75] by using matched filters.

All available methods have their peculiarities which have to be considered for the intended applications. One advantage of the dispersion-sensitive methods is the possibility to extract the mode fields from the measurement data instead of being reliant upon theoretically calculated fields as they have been used for the numerical and correlating techniques. Hence, these are in particular suited

for the characterization of novel or unknown fiber architectures where the actual mode set is unknown. The drawback of all propagation property based methods are the indistinguishability of degenerated modes and the restricted application on disperse media like optical fibers. In contrast, the modal field based methods are very general in their application and can be applied to laser resonators and passively shaped beams. Such techniques can resolve the entire mode spectrum including degenerated modes. For the last point it has to be noted that the intensity based numerical methods suffer from an unambiguousness regarding the sign of the topological charge in the case of pure vortex modes [69].

The technical and temporal effort of the different methods has to be taken into account for evaluating their field of application. Here, the S^2-imaging technique requires the most effort on the technical side (broad-band light source or tunable laser, optical spectrum analyzer, two-axis mechanical shifter) as well as the highest time consumption of several minutes for spatial and spectral scanning. In contrast the intensity based numerical methods require only a simple setup (cameras and imaging system) and, depending on the minimization algorithm, the measurement time is in the range of a few seconds or even lower [69, 76]. Real-time or one shot measurements become possible by the correlation filter methods, where the entire mode spectrum can be extracted from a single camera recording. The main technical effort of this technique lies in the matched correlation filters and depends on their concrete realization (details see Sec. 2.3.3).

The aforementioned features of the correlation filter method highlight the promising capabilities of it as a universal applicable modal analysis tool. Additionally, also in direct comparison with a numerical phase retrieval algorithm [77] and the S^2 imaging technique [78] it has shown its reliability and flexibility. By this reasons the correlation filter method was chosen as the technique of choice during this thesis and will be furthermore introduced in detail.

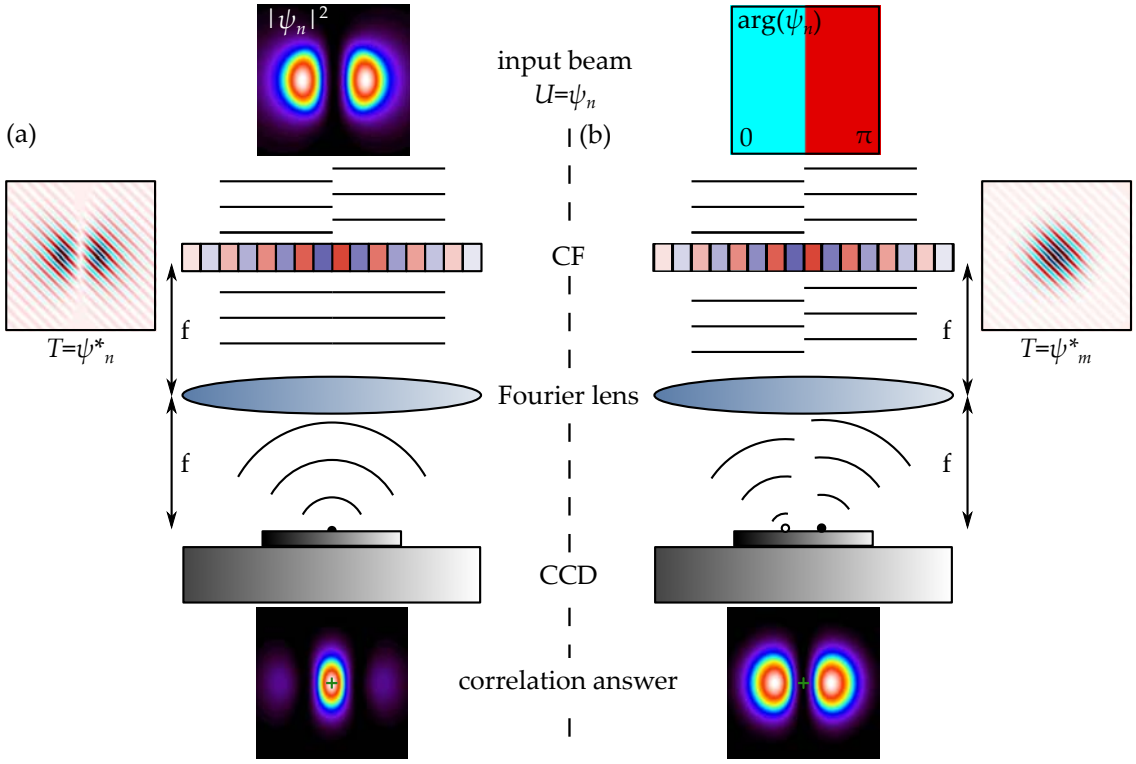

Figure 2.6: Scheme of the correlation filter principle. An incident field ψ_n undergoes a phase cancellation when it is matched to the correlation filter's (CF) transmission function and produce a bright spot on the optical axis in the detection plan (a). If the filter is not matched, no phase cancellation occurs and no signal is measurable on the optical axis (b).

2.3.2 Optical Correlation Analysis

The optical correlation analysis is based on the all optical performance of the inner product $\langle U|T\rangle$ relation between the unknown field U and a designed transmission function T, realized by the holographic correlation filter (CF). The qualitative working principle is illustrated in Fig. 2.6, where the input field is given by the LP_{11e} mode with a characteristic phase step of π between the right and the left side of the beam. In Fig. 2.6 (a) the illuminated CF has the complex conjugated field distribution of the LP_{11e} mode implemented as the transmission function, which causes a cancellation of the phase step in the transmitted field. After focusing the modified field distribution with a Fourier lens in a $2f$ configuration, a bright spot on the optical axis is observable in the detection plane, marked by the green cross, which indicates the presence of the encoded LP_{11e} mode in the investigated beam.

The opposite case of an incoming field which does not match the CF is shown in Fig. 2.6 (b), where the LP_{01} mode is encoded as the transmission function. In this case no phase cancellation takes place and consequently no intensity is measurable on the optical axis in the detection plane, marked by the green cross. This reveals the absence of the LP_{01} mode within the input field. For a mixed input field distribution composed of the LP_{01} and LP_{11e} modes, in both cases measurable intensities would occur on the optical axis whereby the relative strength of those correlation signals corresponds to the power ratio between both modes.

From the quantitative point of view the signal in the detection plane represents the two-dimensional correlation integral between the illuminating field $U(\mathbf{r})$ and the CF transmission function $T(\mathbf{r})$

$$C(\mathbf{r}) = A_0 \iint_{\mathbb{R}^2} \mathrm{d}^2\mathbf{r}' \tilde{T}\left[\frac{2\pi}{\lambda f}\mathbf{r}'\right] \tilde{U}\left[\frac{2\pi}{\lambda f}(\mathbf{r}-\mathbf{r}')\right], \tag{2.19}$$

where A_0 is a constant factor, λ is the wavelength, f is the focal length of the Fourier lens and $\tilde{T}$, $\tilde{U}$ are the Fourier transform of U and T, respectively. For $\mathbf{r} = 0$ at the optical axis the correlation integral $C(0)$ becomes proportional to the inner product relation $\langle U|T^*\rangle$ between the Fourier transformed incident field U and the complex conjugated CF transmission function T. By the implementation of suitable transmission functions the CF method yields access to the complex modal coefficients c_n defined in Eq. (2.14). Following this definition the modal weight ρ_n can be determined using the complex conjugated mode fields ψ_n^* itself as a transmission function. In this case the intensity on the optical axis is given by $|C_n(0)|^2 = |A_0|^2\rho_n^2$, where the completeness of the mode set $\sum \rho_n^2 = 1$ yields the relative modal power. For the measurement of the inter-modal phase difference $\Delta\varphi_n$, specific transmission functions are applied which realize an interferometric superposition between the mode of interest ψ_n and a reference mode ψ_0. Due to the ambiguity of the cosine and sine relations, two transmission functions of the kind

$$T_n^{\cos} = \frac{1}{\sqrt{2}}\left(\psi_0^* + \psi_n^*\right) \qquad \text{and} \qquad T_n^{\sin} = \frac{1}{\sqrt{2}}\left(\psi_0^* + i\psi_n^*\right) \tag{2.20}$$

are necessary to determine the intra-modal phase difference unambiguously as

$$\Delta\varphi_n = -\arctan\left[\frac{2I_n^{\sin} - I_0(\rho_n + \rho_0)}{2I_n^{\cos} - I_0(\rho_n + \rho_0)}\right] \in [-\pi, \pi]. \tag{2.21}$$

Here, $I_n^{\sin}$ and $I_n^{\cos}$ are the correlation signals which correspond to the transmission functions $T_n^{\sin}$ and $T_n^{\cos}$, respectively. By the complete knowledge of the modal weights and the intra-modal phase differences of all guided modes, the entire scalar transverse field distribution can be reconstructed following the superposition principle [Eq.(2.13) p. 13].

2.3.3 Holographic Techniques

The key element of the aforementioned correlation filter method for the model decomposition is the CF, which provides the matched transmission function T. As mentioned in Sec. 2.2 the required complex valued modal field distributions can be provided by CGHs. In contrast to the beam shaping approaches discussed in Sec. 2.2, the CFs applied during this thesis are realized using both types of holograms, phase-only and amplitude-only. The phase-only CFs are implemented by the coding technique proposed by Arrión et al [48] as previously described in Sec. 2.2.1 and displayed with a phase-only SLM. For the amplitude-only elements Lee-encoded binary holograms [49] are applied.

The Lee-algorithm for encoding complex values into a binary amplitude structure uses the notation of a complex value in terms of its real and imaginary part instead of an amplitude and a phase value applied for the phase-only techniques, see Fig. 2.7 (a). Considering that each hologram cell embodying one pixel of the complex transmission function T, it is split into four parts: positive, negative real and, imaginary parts

$$T = T_{re}^{+} + T_{im}^{+} + T_{re}^{-} + T_{im}^{-} \tag{2.22}$$

and is represented by one of the four horizontally divided sub-cells in the holo-

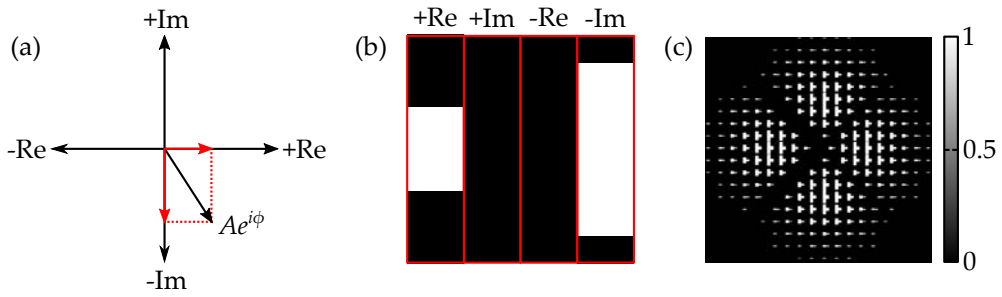

Figure 2.7: Working principle of the Lee coding technique, (a) representation of a complex number by its real and imaginary part, (b) unit cell of the hologram with correspondingly opened sub-pixels where white and black represents transparent and opaque sections respectively, (c) example of a modal transmission function for the LP_{21e} mode.

gram, depicted in Fig. 2.7 (b). The division in four equal horizontal sub-cells corresponds to a splitting of the phase space in four sectors as followed by Eq. (2.22). To control the transmittance of each cell, it is patterned with an opaque (black) and a transparent (white) section (binary amplitude hologram). Thus, the value of the real and imaginary parts are fixed by ratio between both sections, i.e., the opening of the sub-cell aperture. Figure 2.7 (c) shows an example of the Lee encoded transmission function for the LP_{21e} mode. The Lee-coded holograms were fabricated via laser-lithography where the binary structure was written into a chromium layer deposited on a glass substrate.

Since the proposed modal decomposition technique is based on the completeness of the underlying mode set, transmission functions for all guided modes and their interferometric superpositions have to be realized and applied on the investigated beam. To avoid the splitting of the beam in several copies and the usage of multiple filter elements, suitable multiplexing strategies have to be applied to implement all needed transmission functions in one single element. Throughout this work two different types of multiplexing were performed depending on the realization of the CF. Due to the possibility of a dynamical change of the transmission functions with the SLM, a time multiplexing procedure was used for the decomposition with phase-only transmission functions. That means that each required transmission function is displayed subsequently and the correlation signals are measured at different times but at the same detector position. This kind of

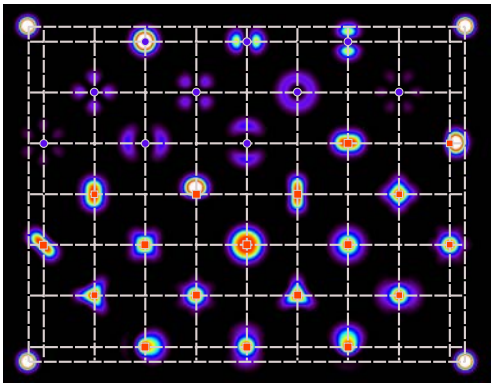

Figure 2.8: Correlation signals in the Fourier plane of a spatially multiplexed CF, illuminated with fundamental Gaussian like mode, where 28 channels are implemented for the determination of the modal weights (purple circle) and intra-modal phases (red squares) illuminated. The adjustment channels in the corners define the coordinate system for the local optical axes. The image is oversaturated for better visibility.

multiplexing can only be used under static conditions to ensure that all individual filter functions are applied on the same beam. Since the amplitude-only filters are statically written into the chromium layer, a time multiplexing is not possible. Instead a spatial multiplexing technique is used. To do so, all needed transmission functions T_n are multiplied by an additional individual phase gradient $\mathbf{K}_n$ and combined to one fixed total transmission function

$$T_{ges}(\mathbf{r}) = \sum_{n=0}^{n_{max}} T_n \exp(i\mathbf{K}_n\mathbf{r}). \tag{2.23}$$

By this technique the individual correlation signals will be shifted in the Fourier plane of the CF by $\mathbf{r}_n = \frac{\lambda f}{2\pi}\mathbf{K}_n$. Hence, the detection of all implemented correlation signals at the same time but at different positions becomes possible and enables the real-time measurement of dynamic processes. The drawback here is the limitation by the amount of implemented transmission functions. Throughout this thesis a 1/1.8" CCD sensor was used, which allows the implementation of up to 30 individual correlation channels with sufficient lateral spacing to avoid channel crosstalk. Figure 2.8 shows the occurring intensity distribution in the Fourier plane of the CF, where 28 transmission functions are implemented for the determination of the modal weights (purple circles) and intra-modal phases (red

squares) of ten modes. The additional channels in the corners are required to define the coordinate system of the local optical axes.

All binary Lee-coded holograms used within this thesis were fabricated by laser lithography at the Leibniz Institute of Photonic Technology Jena. For that 512×512 Lee cells were inscribed on a chromium film on glass wafer, where each cell had an extension of 16 μm × 16 μm and a minimal structure size of 700 nm.

2.3.4 Modal Stokes Measurement

The aforementioned holographic realization schemes of the CF are restricted to scalar beams only, due to the fact that the applied holograms contain no polarization information. To overcome this limitation, a combination of the holographic correlation filter method and a Stokes parameter measurement can be performed. In classical optics the polarization state of a beam is completely described by its Stokes vector

$$\mathbf{S} = \begin{pmatrix} S_0 \\ S_1 \\ S_2 \\ S_3 \end{pmatrix} = \begin{pmatrix} I(0°) + I(90°) \\ I(0°) - I(90°) \\ I(45°) - I(135°) \\ I_{\frac{\lambda}{4}}(45°) - I_{\frac{\lambda}{4}}(135°) \end{pmatrix} \propto \begin{pmatrix} |U_x|^2 + |U_y|^2 \\ |U_x|^2 - |U_y|^2 \\ 2|U_x||U_y| \cos \delta_{rel} \\ 2|U_x||U_y| \sin \delta_{rel} \end{pmatrix} \tag{2.24}$$

where $|U_x|$ and $|U_y|$ are the field components in horizontal and vertical orientation, respectively, and δ_{rel} the phase difference between both components. This stokes vector is directly accessible by six intensity measurements [79], four with different polarizer orientation at 0°, 45°, 90° and 135°, and two after a quarter wave plate oriented at 0° and a polarizer at 45° and 135°, respectively. This concept can be easily extended by spatially resolved intensity measurements, which results in a spatially resolved polarization distribution $\mathbf{S}(\mathbf{r})$ [80, 81].

Analogously, an expansion to a modally resolved Stokes vector $\mathbf{S}_n$ is also possible by the determination of the relative weights ρ_n using the CF method for the six different configurations of polarization manipulating elements in the light

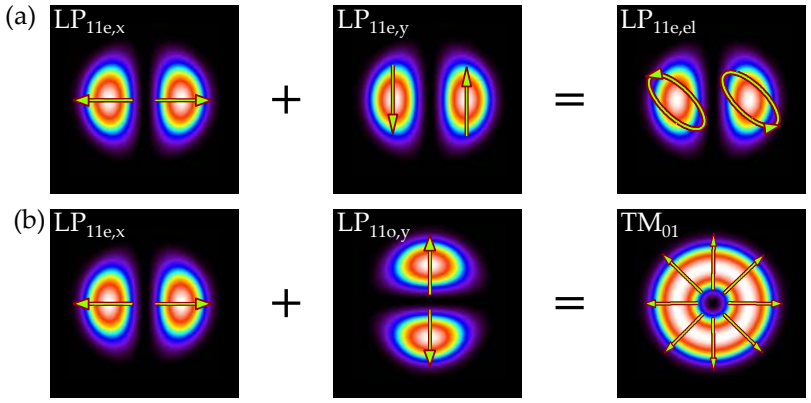

Figure 2.9: Superposition of different polarized LP modes, (a) the superposition of the x and y polarized LP_{11e} modes form a general elliptical but uniformly polarized field distribution (b) the superposition of the x polarized LP_{11e} and y-polarized LP_{11o} modes results in the TM_{01} mode distribution

path. The resulting Stokes vector for the n-th mode reads as follows [82]

$$\mathbf{S}_n = \begin{pmatrix} S_{0,n} \\ S_{1,n} \\ S_{2,n} \\ S_{3,n} \end{pmatrix} = \begin{pmatrix} \rho_n^2(0°) + \rho_n^2(90°) \\ \rho_n^2(0°) - \rho_n^2(90°) \\ \rho_n^2(45°) - \rho_n^2(135°) \\ \rho^2_{n,\frac{\lambda}{4}}(45°) - \rho^2_{n,\frac{\lambda}{4}}(135°) \end{pmatrix} \propto \begin{pmatrix} \rho_{n,x}^2 + \rho_{n,y}^2 \\ \rho_{n,x}^2 - \rho_{n,y}^2 \\ 2\rho_{n,x}\rho_{n,y}\cos\delta_n \\ 2\rho_{n,x}\rho_{n,y}\sin\delta_n \end{pmatrix}. \tag{2.25}$$

Using this n-th order modal Stokes vector $\mathbf{S}_n$, the intra-modal phase difference between the two polarization degenerated modes is calculated from

$$\delta_n = \arctan\left(\frac{S_{3,n}}{S_{2,n}}\right) \in [-\pi, \pi]. \tag{2.26}$$

Together with the directly measured relative modal weights $\rho_{n,x}$ and $\rho_{n,y}$ of the independent vector components, the polarization state of each guided mode is completely characterized. To illustrate this procedure, Fig. 2.9 (a) shows an equally weighted superposition of the $LP_{11e,x}$ and $LP_{11e,y}$ mode with an intra-modal phase difference $\delta_n = \frac{\pi}{4}$, which results in an elliptically but uniformly polarized and thus still scalar $LP_{11e,el}$ mode. Further, the determination of the intra-modal phase differences enables the reconstruction of vectorial fields with spatially varying polarization distributions following Eq. (2.15) p. 14, as exemplary depicted in

Fig. 2.9 (b) for a equally weighted superposition of the $LP_{11e,x}$ and the $LP_{11o,y}$ mode forming the radially polarized TM_{01} mode.

Chapter Summary

In this chapter the concept of modes was introduced, which are the eigenfunctions of the characteristic equation describing the underlying physical system. Their fundamental properties, such as orthogonality, completeness and field distribution were outlined and simple examples were given. In the beginning (Sec. 2.1) the occurrence of hybrid vector mode fields in optical fibers was discussed and the weak guiding approximation leading to a scalar modes set was performed. Additionally, the interrelation of both mode sets by modal superpositions was shown. Afterwards, a holographic approach for the creation of pure mode fields and arbitrary superposition of them was outlined in Sec. 2.2. Finally, the correlation filter method for the complete modal analysis was introduced in Sec. 2.3. Since both techniques rely on the holographic realization of modal transmission functions, suitable coding algorithms were discussed to realize the complex valued modal field distribution by phase-only or amplitude-only holograms.

3 Decomposition into Linear Polarized Fiber Modes

Although the exact solution of optical fiber modes are in general hybrid vector fields, for most fiber applications the weak guidance approximation is valid and applied, resulting in the easy accessible set of linear polarized (LP) modes. By this reason the decomposition into LP modes is of great practical importance for applications ranging from fiber lasers and amplifiers, fiber sensors, to optical fiber communication. Therefore the correlation filter method will be applied for the decomposition of fiber beams into linearly polarized modes to investigate fiber propagation and fiber-to-free space coupling effects. Finally, a mode-division multiplexing procedure through a multiple media communication link will be introduced.

3.1 Fiber Mode Analysis

The fiber mode analysis provides a direct access to the modal coefficients and thus presents a powerful tool for the characterization and quality evaluation of optical fiber beams. In many applications multi-mode fibers are used for power scaling purpose but only the fundamental mode operation is intended to preserve a high spatial beam quality and beam-pointing-stability. Such applications range from material processing (cutting, drilling) [83], fiber laser [84] and amplifier [85] development, fiber alignment or splicing [86,87], to laser microscopy [88]. In those cases the determination of the higher-order mode content, which causes unwanted beam distortion, provides a kind of quality test. A detailed investigation on how the detected higher order modes influence the beam quality becomes possible by

the reconstruction of the complete optical field and for example by a subsequent virtual caustic measurement, which delivers the M^2-parameter [28]. Besides the consideration of higher-order modes as a perturbation source they can also be used to advantage, e.g. for robust and bend-resistant propagation in fibers [89] or for increasing the sensitivity of fiber sensors [90–92]. Additionally, for mode-division multiplexing strategies in the field of optical communication, where the spatial fiber modes are utilized as a new degree of freedom for carrying parallel data links, higher order mode spectra have to be evaluated [15, 19].

In this section the ability of the correlation filter method to modally decompose and reconstruct fiber beams will be presented. Afterwards the CFM is used to determine the fiber transmission properties by multiple-input-multiple-output measurements and the recorded fiber transmission matrix is applied for signal processing.

3.1.1 Reconstruction of Fiber Beams

At first the capability of the CFM for the decomposition of optical fiber beams will be presented by reconstruction of the intensity distribution using the measured modal coefficients. To evaluate the quality of the modal decomposition a closed loop procedure is applied, where the direct measured near field intensity distribution $I_{me}(\mathbf{r})$ of the investigated beam is compared with the reconstructed one $I_{rec}(\mathbf{r})$ using the measured modal coefficients. For the quantification of this comparison the two dimensional cross-correlation coefficient is used [93]

$$C = \frac{\iint\limits_{\mathbb{R}^2} \left[I_{me}(\mathbf{r}) - \bar{I}_{mes}\right] \left[I_{rec}(\mathbf{r}) - \bar{I}_{rec}\right] \mathrm{d}^2\mathbf{r}}{\sqrt{\iint\limits_{\mathbb{R}^2} \left[I_{me}(\mathbf{r}) - \bar{I}_{mes}\right]^2 \mathrm{d}^2\mathbf{r} \iint\limits_{\mathbb{R}^2} \left[I_{rec}(\mathbf{r}) - \bar{I}_{rec}\right]^2 \mathrm{d}^2\mathbf{r}}}, \tag{3.1}$$

where $\bar{I}_{me}$ and $\bar{I}_{rec}$ indicates the mean values of the measured and reconstructed intensity distribution, respectively. Thus, C is indicating the linear relationship between the measured and reconstructed intensities and accepts values within

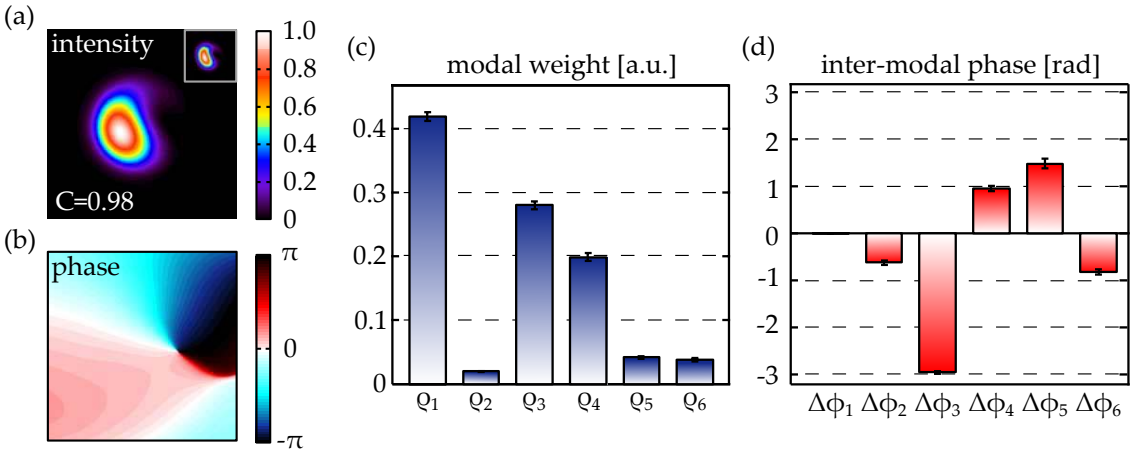

Figure 3.1: Model decomposition and field reconstruction of a step-index fiber beam, (a) reconstructed intensity distribution, (b) reconstructed phase distribution, (c) measured modal power spectrum and (d) measured inter-modal phase differences. The inset shows the measured near field intensity distribution.

$[-1, 1]$, which can be interpreted as

$$|C| = \begin{cases} 1 & \text{complete linear relationship} \\ 0 & \text{linear independancy} \\ \text{else} & \text{partial relationship} \end{cases} . \tag{3.2}$$

Within this work correlation coefficients higher than 0.95 will be classified as successful reconstruction.

Figure 3.1 shows an example decomposition and reconstruction of a beam emerging from a step-index fiber with a core diameter $d_{cor} = 25\ \mu$m and a V parameter of 6.5. It can be seen that the reconstructed intensity distribution depicted in Fig. 3.1 (a) has a high cross correlation coefficient of 0.98 in comparison to the direct measured near field intensity shown in the inset. Additionally, the spatial phase distribution illustrated in Fig. 3.1 (b) was reconstructed, which is commonly measured by elaborated interferometric procedures. The modal coefficients used for this reconstruction are shown in Fig. 3.1 (c) and (d), where the complex valued numbers are split into a modal power content and a inter-

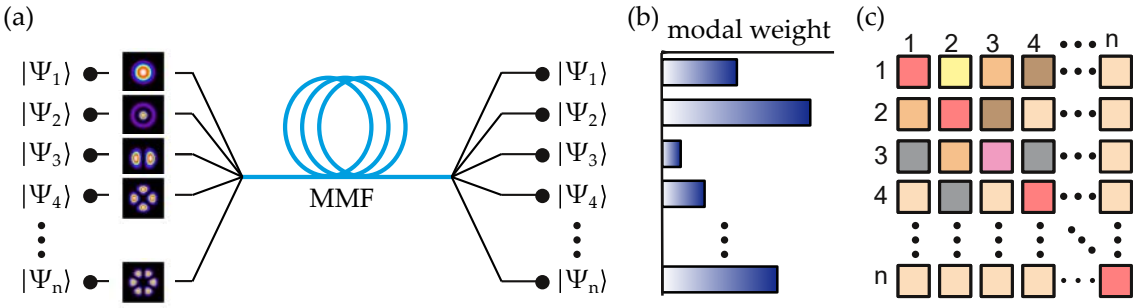

Figure 3.2: Principle scheme of the MIMO measurements for the determination of the fiber's transmission matrix, (a) illustrates the different input and output channels which are tests, (b) shows an exemplary mode spectrum and (c) the measured transmission matrix [97].

modal phase difference with respect to the fundamental mode, respectively.

These examples illustrate the benefit of the field reconstruction by modal decomposition, whereby the full 2D transverse field information can be represented by a discrete set of six complex valued modal coefficients. Furthermore, the knowledge of the complete complex field distribution enables the derivation of additional beam properties like the M^2-value [28, 94], the wave-front aberrations [26, 95], or the orbital angular momentum density [30, 96], to note only a few.

3.1.2 Measurment of the Fiber Transmission Matrix

The ability to reconstruct the modal content of light fields emerging from optical fibers in combination with the holographic beam shaping technique introduced in Sec. 2.2.1, which allows selective fiber mode excitation, leads to the possibility to explore the fiber's transmission properties by multiple-input-multiple-output (MIMO) experiments [98, 99] and the results from an optimized measurment scheme [97] will be presented in detail. Each possible guided mode will be offered to the fiber as excitation and subsequently the modal resolved fiber response will be determined by the CFM. The principle procedure is illustrated in Fig. 3.2, where the MIMO measurement scheme is shown in Fig. 3.2 (a). Recording for all excited modal inputs the response spectrum, depicted in Fig 3.2 (b), allows the construction of a fiber transmission matrix as illustrated in Fig. 3.2 (c). In

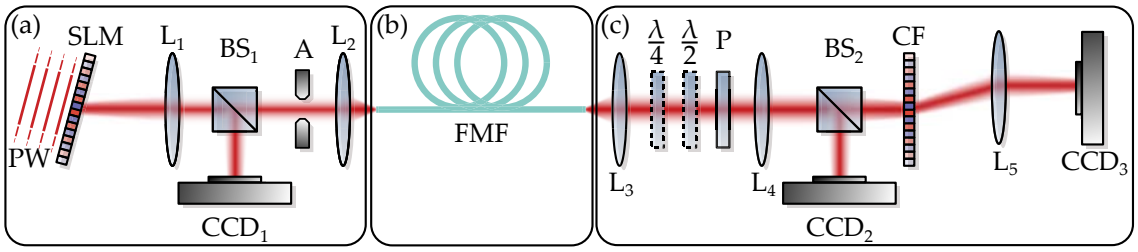

Figure 3.3: Setup for the determination of the fiber's transmission matrix [97]. PW, plane wave; SLM, spatial light modulator; L_{1-5}, lenses; $BS_{1,2}$, beam splitter; A, aperture; CCD_{1_3}, cameras; FMF, few mode fiber; $\frac{\lambda}{4}$, quarter wave plate; $\frac{\lambda}{2}$, half wave plate; P, polarizer; CF, correlation filter. Dashed elements are not always used.

principle, at least N × N measurements are necessary to determine all matrix components but in reality even more measurements are required to unambiguously assess the complex valued matrix elements [99]. However, the application of the spatial multiplexing strategy of the Lee-coded amplitude-only filters, allows a simultaneous decomposition into all guided modes and reduces the problem to only N measurements. Since the crosstalk in common fibers into the fundamental mode, which is typically assigned to be the reference for the phase measurement is usually low, a second set of measurements was performed where a superposition of the individual modes and the fundamental mode was excited for the reliable determination of the inter-modal phase differences [97]. Altogether the N × N complex elements of the fiber's transmission matrix could be reconstructed by 2N individual measurements. The finally received fiber's transmission matrix represents the complete linear transfer properties of the fiber, including mode coupling and beating as well as modal attenuation. For a perfect orthogonal lossless mode set, this matrix would be a diagonal one. However, in real fiber systems, due to modal crosstalk non-diagonal elements will also occur, which results in a disturbed transmitted mode profile with respect to a purely excited modal input.

For the determination of the fiber's transmission matrix, the setup illustrated in Fig. 3.3 was used. The first part of the setup [Fig. 3.3 (a)] allows the generation and excitation of pure fiber modes by the holographic beam shaping technique described in Sec. 2.2.1 pp. 16. Here a plane wave illuminated an SLM (Hamamatsu

LCoS X 10468-03 with 800 x 600 pixels of pitch 20 μm, calibrated for a 2π phase shift at λ = 1064 nm) with the modal field function encoded as a phase only hologram. Next the shaped field within the first diffraction order was downscaled with a telescope in $4f$ configuration comprising the lenses L_1 and L_2 (f_{L_1} = 400 mm; f_{L_2} = 4 mm). Additionally, an aperture at the intermediated Fourier-plane was used as low-pass filter to block non desired diffraction orders and stray light. To evaluate the quality and power of the generated beam the far-field intensity distribution was recorded by the camera CCD_1 using a 50:50 beam splitter BS_1 within the telescope. The second part [Fig. 3.3 (b)] contains the investigated fiber which perturbs the purely excited input stated according to its transmission properties. In this experiment a fiber with a core diameter of d_{co} = 30 μm and V-parameter $\approx$ 7 was investigated. In a final step the fiber response was determined by complete modal decomposition [Fig. 3.3 (c)] using the CFM described in Sec. 2.3 pp. 19.The fiber end face was magnified with the telescope formed by L_3 and L_4 in $4f$ configuration (f_{L_3} = 10 mm; f_{L_3} = 375 mm) onto the plane of the CF. Separated by a 50:50 beam splitter BS_2, the out coupled near field intensity distribution was recorded with the camera CCD_2 to enable the closed loop reconstruction validation and the determination of the transmitted power. After the CF, the modal decomposition was finished by Fourier-imaging of the transmitted light using lens L_5 in $2f$ configuration (f_{L_5} = 180 mm) and detection of the correlation signal by the camera CCD_3.

First, a short fiber piece of about 20 cm length was investigated to characterize a nearly ideal fiber only influenced by manufacturing imperfections. By applying the aforementioned measurement procedure the complex fiber's transmission matrix T was determined, which is depicted in Fig. 3.4 (a) and (b) showing its squared absolute values and the arguments, respectively. In this matrix representation each column represents the modal response for specifically offered input modes and was normalized according to the relative transmitted laser power of the core signal. It can be seen that for this ideal fiber case mainly diagonal elements occur. Only between mode three and four, representing the modes LP_{11e}

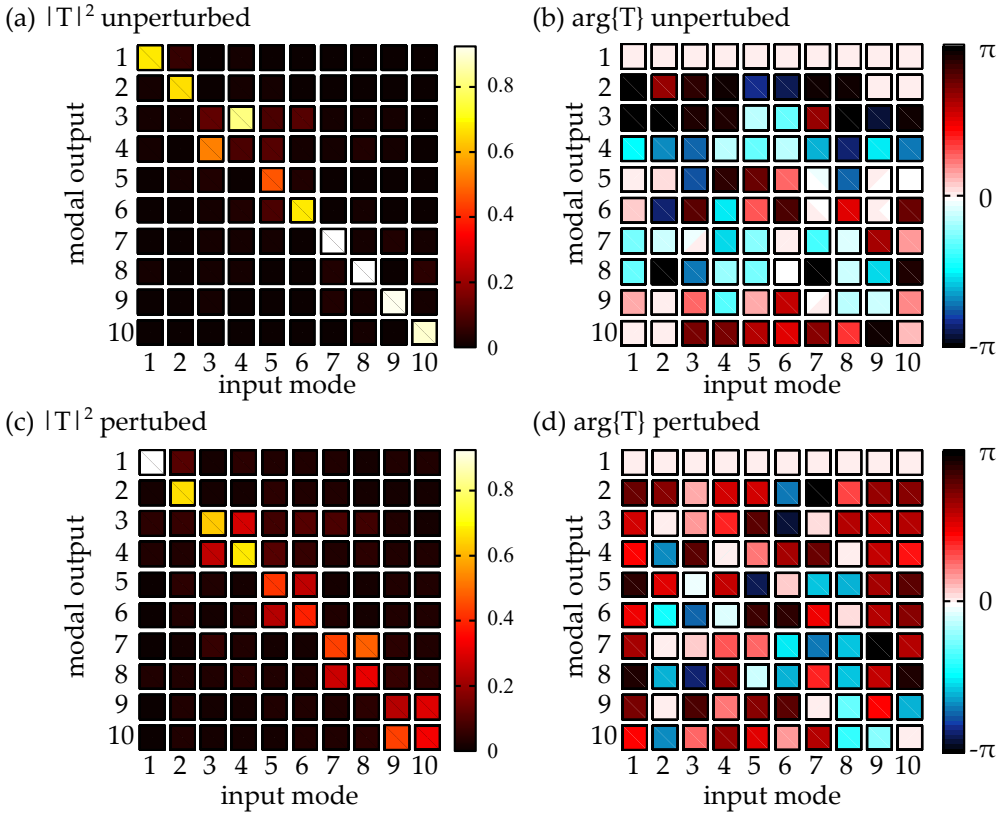

Figure 3.4: Fiber transfer matrix representing the linear transmission properties of a fiber with V≈ 7. (a) absolute value of an unperturbed fiber piece, (b) corresponding argument of the transmission matrix, (c) absolute value of a perturbed fiber (length ≈ 8 m) and (d) argument of the perturbed transfer matrix [97].

and LP_{11o} respectively, a strong crosstalk is observable. Since these modes are degenerated with respect to their propagation constant, they are likely to couple at fiber imperfections.

In the following, the fiber's transmission matrix of a "real" step-index fiber was investigated which was approximately 8 m long and coiled in several loops of ≈ 10 cm bending radius. As result, the recorded transmission matrix depicted in Fig. 3.4 (c) and (d), shows strong mode coupling between all degenerated mode pairs, which are the modes $LP_{11e/o}$ (mode 3 and 4) the modes $LP_{12e/o}$ (mode 5 and 6) the modes $LP_{21e/o}$ (mode 7 and 8) and the modes $LP_{31e/o}$ (mode 9 and 10). Additionally, a strong mode dependence of the propagation loss was detected. In fact the normalized transmitted power of the $LP_{31e/o}$ modes was attenuated by a

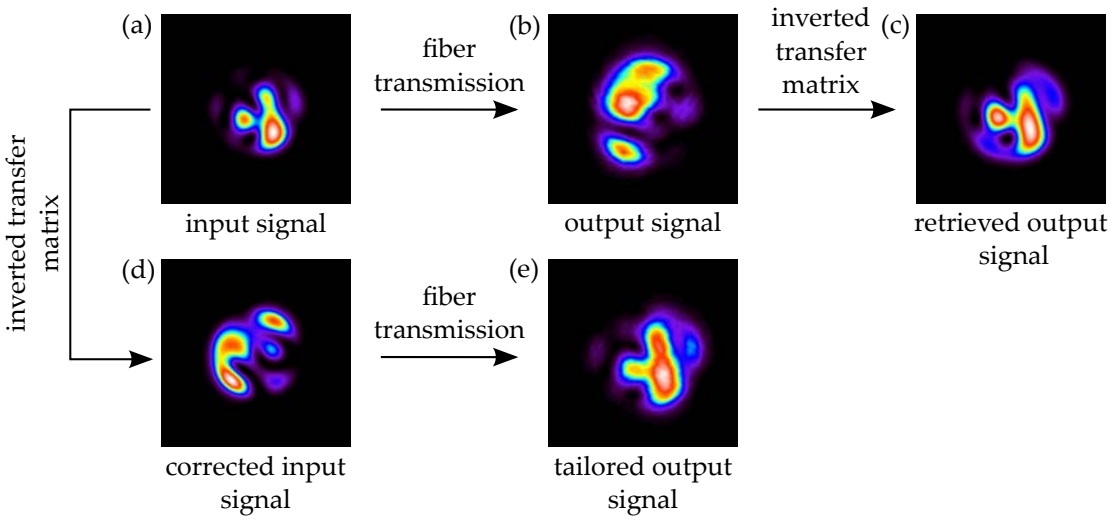

Figure 3.5: Signal correction by pre- and post processing applying the inverted transfer matrix, (a) the original input signal, (b) the uncorrected output signal, (c) the retrieved output signal, (d) corrected input signal and (e) tailored output signal.

factor of two in comparison to the fundamental mode.

The complete knowledge about the fiber transmission properties, including mode coupling, relative modal delay, and modal power loss is represented by the fiber's transfer matrix, which allows the description of the fiber impact on the transmitted signal by a matrix formalism,

$$\mathbf{b} = \mathrm{T}\mathbf{a}, \tag{3.3}$$

where **a** denotes the vector of the complex modal coefficients at the fiber input and **b** that of the fiber output. The effect on the transmitted beam can be seen in Fig. 3.5 (a) and (b), where an example input beam and the corresponding output beam are depicted. It can be seen that the intensity distribution of the transmitted beam differs clearly from that of the input beam. By applying the inverted transfer matrix $(T)^{-1}$, a pre- or post-signal processing of the input and output beam is possible. For post processing, the inverted transfer matrix is

applied on the modal coefficients of the output

$$\mathbf{b}^{cor} = (\mathrm{T})^{-1}\mathbf{b} = \mathbf{a}, \tag{3.4}$$

which retrieves a corrected output mode spectrum $\mathbf{b}^{cor}$ from the input spectrum $\mathbf{a}$ by using Eq. (3.3) and the identity $(\mathrm{T})^{-1}\mathrm{T} = \mathbb{1}$ with $\mathbb{1}$ the unit matrix. Thus, the original injected beam can be retrieved as illustrated in Fig. 3.5 (c). A second application of the inverted transmission matrix is the tailoring of the output beam by pre-compensation of all fiber effects already at the fiber input. For that, the inverted transmission matrix is applied on the desired modal superposition to determine a corrected input beam. After propagation through the fiber, the real propagation effects cancel out input correction and the desired beam is achieved at the output as it can be seen in Fig. 3.5 (d) and (e). By this example, it can be seen that besides the characterization of the fiber itself, the fiber transmission matrix can be used for signal processing, which enables the reconstruction of the original signal or the tailoring of the output beam profile. Additionally, the reliability of the fiber characterization procedure base on the CFM is validated by the successful application of the inverse transmission matrix.

3.2 Mode System Matching

Besides the possibility of all-fiber devices or the usage of imaging systems the connection between fiber and free-space modes is important to control the optical properties of fiber beams during free space propagation. This becomes necessary for applications dealing with beams emerging from optical fibers or for the excitation of fiber modes by free-space beams. The simplest connection can be realized by graded-index fibers with a parabolic refractive index profile, whose modes can be described by Laguerre-Gaussian (LG) functions, which are solutions of the free-space wave equation [35] and ensure stable free-space propagation. However, in all other cases, beams emerging from fibers will be distorted during free space propagation due to the non-matching of the fiber mode solutions with that

of free-space. In addition, a pure excitation of fiber modes by free-space modes is not suitable in general and additional beam shaping techniques are required, such as the use of computer generated holograms described in Sec. 2.2.1 pp. 16. Although a high modal purity is achievable, such holographic techniques [100] suffer from high transformation losses due to the low efficiency of the required coding techniques. For the common type of step-index fibers which show the same cylindrical symmetry as in the paraxial free-space case, it is possible to approximate the fiber modes by suitable free space modes. To evaluate the quality and the limitations of such an approximation, the overlap relation between step-index fiber modes and those of free space was experimentally and theoretically investigated [101] and will be presented here in detail. Afterwards an application of the introduced approximation will be demonstrated by the selective excitation of fiber modes with a digital controllable solid state laser source [102].

3.2.1 Scale Depending Overlap

The transition from free-space to fiber, and vice versa, is determined by the coupling between both mode sets and can reach nearly 100% for perfectly matched systems despite a small amount of Fresnel reflection due to the refractive index difference between the glass of the fiber and the air of the free space. In the case of weakly guiding fibers linearly polarized (LP) modes are the solution of the scalar Helmholtz-equation Eq. (2.11) p. 13. Considering a cylindrically symmetric and step wise constant refractive index profile, the field distribution $\mathrm{LP}_{lp}(r,\phi)$ for a fiber with a core radius a_0 is given by [35]

$$LP_{lp}(r,\phi) = N_{lp} e^{il\phi} \times \begin{cases} J_l\left(\frac{\nu_{lp} r}{a_0}\right) / J_l\left(\nu_{lp}\right) & \text{for } r < a_0 \\ K_l\left(\frac{\mu_{lp} r}{a_0}\right) / K_l\left(\mu_{lp}\right) & \text{for } r \geq a_0 \end{cases}, \tag{3.5}$$

where N_{lp} is a normalization constant, J_l denotes the lth-order Bessel-function of the first kind, and K_l denotes the lth-order modified Bessel-function of the second kind, with ν_{lp} and $\mu_l p$ being the normalized propagation constants of core and

cladding, respectively. For the description of the LP modes,additionally the fiber parameter V is required, which is defined as

$$V^2 = \nu^2 + \mu^2 = \left(\frac{2\pi}{\lambda} a_0\right)^2 \left(n_{co}^2 - n_{cl}^2\right), \tag{3.6}$$

with n_{co} and n_{cl} the refractive indices of the core and cladding material, respectively. This fiber parameter defines the number of modes and links the geometry and material parameters to the propagation constants. Hence, the fiber mode set is uniquely defined by this parameter.

Following the cylindrical symmetry of a step-index fiber, the adapted free-space mode set is given by Laguerre-Gaussian (LG) modes, which are solutions of the paraxial Helmholtz-equation in a cylindrically symmetric coordinate system. For that, the solution at the waist position is given by [31]

$$LG_{pl}(r, \phi) = M_{pl} e^{-\frac{r^2}{w_0^2}} \left(\frac{2r^2}{w_0^2}\right)^{\frac{|l|}{2}} L_p^{|l|}\left(\frac{2r^2}{w_0^2}\right) e^{il\phi}, \tag{3.7}$$

where $L_p^{|l|}$ are the associated Laguerre polynomials, w_0 is the fundamental Gaussian radius and $M_{pl} = \frac{1}{w_0}\left(\frac{2p!}{\pi(l+p)!}\right)^{\frac{1}{2}}$ is a normalization factor. Comparing Eq. (3.5) and Eq. (3.7), it can be seen that both solutions share the same azimuthal dependency and the radial order is characterized by the amount of root points in the intensity distribution. Hence, corresponding modes can be found by choosing modes of the same azimuthal order and with the same amount of roots in the radial direction. Despite the similarities between both solutions, the actual shape of the radial functions differs, which makes an adaptation of scale parameter necessary for the best possible matching. The matching of the scale can be evaluated by the overlap relation

$$\eta_n = \iint_{\mathbb{R}^2} LG_n(\mathbf{r}) LP_n^*(\mathbf{r}) \mathrm{d}^2\mathbf{r}, \tag{3.8}$$

where η_n defines the amount of power that is coupled from one mode into the

other at the transition between both mode sets. It can reach values between one when the fields are perfectly matched, and zero for orthogonal fields. The amount of power $1-\eta_n$ which is not coupled into the desired mode, goes in other overlapping, reflecting, or radiating modes to satisfy energy conservation. To find the optimal scaling ratio between the Gaussian width w_0 of the free space modes and the core radius a_0 of the optical fiber, an analytical expression for the overlap relation Eq. (3.8) was derived [101]. First, the problem was separated into a core and a cladding part, corresponding to the different types of solutions of the fiber modes Eq. (3.5). The phase term $e^{il\phi}$ ensures that LP and LG modes must have the same azimuthal index l for an overlap $\eta_n \neq 0$. Hence, the actual value of η_n for corresponding modes is completely determined by radial part of Eq. (3.8). For the integration of the core region the Bessel-function for the radial field dependency will be written as an infinite sum,

$$J_l(x) = \sum_{m=0}^{\infty} \frac{(-1)^m}{m!\Gamma(m+l+1)} \left(\frac{x}{2}\right)^{2m+l}, \tag{3.9}$$

with Γ the gamma function. Additionally, the Laguerre polynomials can be written as its generating function,

$$L_p^{|l|}(x) = \frac{1}{p!} \left(\frac{d}{d\xi}\right)^p \frac{1}{(1-\xi)^{|l|+1}} exp\left(\frac{-x\xi}{1-\xi}\right)\Bigg|_{\xi=0}. \tag{3.10}$$

Substituting Eq. (3.9) and Eq. (3.10) into the mode functions Eq. (3.5) and Eq. (3.7), respectively, the overlap of both mode sets within the core is given by [101]

$$\begin{aligned}\eta_{lp}^{co} =& \frac{N}{J_l(\mu)} \frac{M}{p!} \left(\sqrt{2}\right)^l \left(\tfrac{d}{d\xi}\right)^p \frac{1}{(1-\xi)^{|l|+1}} \sum_{m=0}^{\infty} \left\{ \tfrac{(-1)^m}{m!\Gamma(m+l+1)} \left(\frac{\mu w}{2a}\right)^{2m+l} \left(\tfrac{1-\xi}{1+\xi}\right)^{m+l+1} \right. \\ & \left. \times \left[\Gamma(m+l+1) - \Gamma\left(m+l+1, \tfrac{a^2}{w^2}\tfrac{1+\xi}{1-\xi}\right)\right]\right\}\Bigg|_{\xi=0}, \end{aligned} \tag{3.11}$$

with $\Gamma(\alpha, z)$ being the incomplete gamma function, N_{lp} and M_{pl} being the normalization constants of the LP and LG modes respectively, a_0 being the fiber core radius and w_0 the Gaussian radius. A similar substitution approach yields the

solution for the cladding region. For that the modified Bessel functions of the second kind K_l are initially expressed by the modified Bessel functions of the first kind I_l:

$$K_l(x) = \lim_{n \to l} \frac{\pi}{2\sin(n\pi)} \left[I_{-n}(x) - I_n(x) \right], \tag{3.12}$$

where the I_n can be written as an infinite sum similar to Eq. 3.9,

$$I_n(x) = \sum_{m=0}^{\infty} \frac{1}{m!\Gamma(m+n+1)} \left(\frac{x}{2}\right)^{2m+n}. \tag{3.13}$$

Using Eq. (3.5) and Eq. (3.9) for the description of the modal fields in the cladding region, together with the previously used representation of the LG modes given by Eq. (3.10), the overlap in the cladding region becomes [101]

$$\begin{aligned} \eta_{lp}^{cl} = \lim_{n \to n} & \frac{\pi}{2\sin(n\pi)} \frac{N}{K_n(\mu)} \frac{M}{p!} \left(\sqrt{2}\right)^n \left(\tfrac{d}{d\xi}\right)^p \frac{1}{(1-\xi)^{|l|+1}} \\ & \times \sum_{m=0}^{\infty} \left\{ \frac{-1}{m!} \left(\frac{vw}{2a}\right)^{2m-l} \left(\frac{1-\xi}{1+\xi}\right)^{m+1} \left[\frac{\Gamma\left(m+n+1, \frac{a^2}{w^2}\frac{1+\xi}{1-\xi}\right)}{\Gamma(m+n+1)} \right. \right. \\ & \left. \left. \left(\frac{vw}{2a}\right)^{2n} \left(\frac{1-\xi}{1+\xi}\right)^n \frac{\Gamma\left(m+1, \frac{a^2}{w^2}\frac{1+\xi}{1-\xi}\right)}{\Gamma(m-n+1)} \right] \right\} \Bigg|_{\xi=0}. \end{aligned} \tag{3.14}$$

Afterwards, the complete overlap relation is given by the sum of the core and cladding part, represented by the Eqs. (3.11) and (3.14), respectively.

To prove the validity of the presented analytical solution, the size dependent overlap relation was also determined experimentally for an exemplary few-mode fiber. For that, the correlation filter method was applied since this decomposition technique, introduced in Sec. 2.3 pp. 19, realizes the required integral relation optically. Hence, the size dependency can be measured by illuminating different scaled LG modes, shaped by an SLM, onto a corresponding static LP mode transmission function. The setup used for this procedure is shown in Fig. 3.6, where a plane wave illuminated a phase only SLM (Holoeye, HEO1080-P with 1920×1080

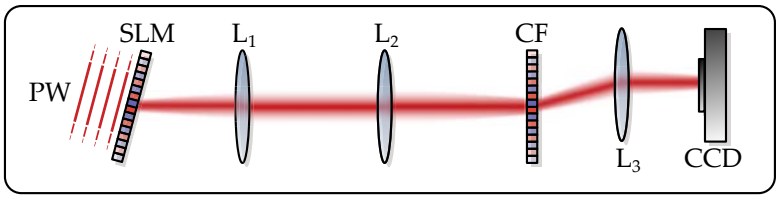

Figure 3.6: Setup for the determination of the size depending overlap between corresponding LG and LP modes [101]. PW, plane wave; SLM, spatial light modulator, L_{1-3}, lenses; CF, correlation filter; CCD, camera.

pixels of pitch 8 μm and calibrated for a 2π phase shift at $\lambda = 1064$ nm) in order to produce the scale variant LG modes. The shaped field was afterwards imaged by a telescopic $4f$ setup formed by lens L_1 and L_2 onto the correlation filter. After an optical Fourier-transformation with lens L_3 in $2f$ configuration the correlation signal could be detected with a CCD camera. Since the encoding method for the holograms displayed on the SLM required all the generated LG modes to be normalized to unit amplitude, see Sec. 2.2.1 pp. 16, energy conservation is therefore violated. By this reason an appropriated power scaling was required to ensure the comparability of the measured results. For that, a correction parameter for each mode field was introduced, followed by the renormalization of the encoded fields. Since the basis mode fields $\psi_n(\mathbf{r})$ are normalized to unit power, the encoded mode fields $\tilde{\psi}_n(\mathbf{r})$ differ only by a constant factor, $\tilde{\psi}_n(\mathbf{r}) = \psi_n(\mathbf{r})/\alpha_n$, where $\alpha_n = \max\{|\psi_n(\mathbf{r})|\}$. Thus an appropriate power scaling and correction of the measured intensity I_{mes} were achieved by multiplying it by the square of the correction parameter α_n to produce the normalized intensity $I_{norm} = I_{meas}\alpha_n^2$ [100].

The experimentally determined overlap values for an example LP mode set of a step index fiber with an underlying V parameter of 4.72 results in the appearance of six guided modes as shown in Fig. 3.7. It can be seen that the measured data resembles very well the theoretical calculated size dependent overlap behavior between LG and LP modes. Additionally, it shows that the LG modes are a very good approximations of the LP modes at a beam-to-core radius ratio of about 0.75. In this case, the overlap is about 0.99 for the LP_{01}, LP_{11} and, LP_{21} modes, and about 0.98 for the LP_{02} mode. A comparison of the scale-dependency reveals some

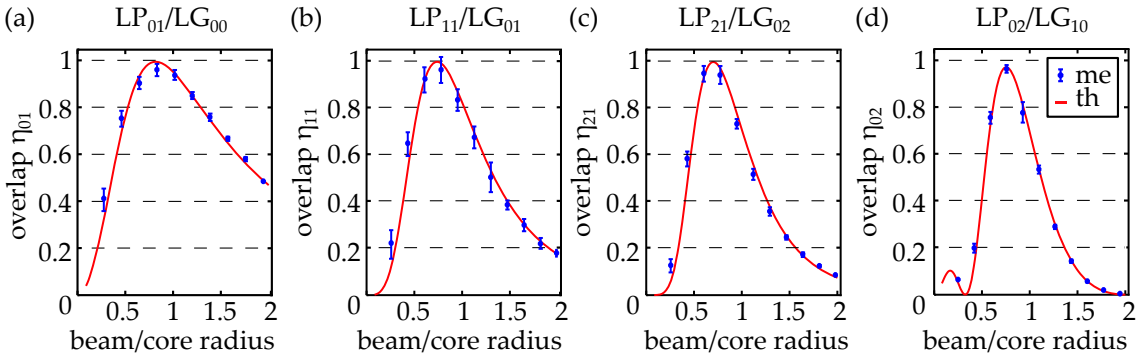

Figure 3.7: Comparison between the theoretically and experimentally determined overlap relation between LG and the corresponding LP modes of a step index fiber with $V = 4.72$ [101].

explicit differences between the four mode groups. An obvious difference is the rate of decrease of the overlap when the LG mode size is not perfectly matched. Whereas for the fundamental mode, LG_{01}, the overlap falls relatively slow, while with increasing mode order the decline becomes faster. Additionally, the best ratio between beam width and core radius for maximal overlap differs slightly for the investigated modes from 0.70 for the LP_{21} mode up to 0.81 for the LP_{01} mode.

Since the observed variations of the scale dependent overlap with respect to the mode order are not very strong for the investigated example, Fig. 3.8 shows the simulated overlap relations of the higher order modes for a theoretical fiber with $V = 50$ to demonstrate some interesting dependencies. Depicted are the dependencies of higher order radial modes with azimuthal order $l = 0$ as well as of higher order azimuthal modes with radial order $p = 1$, where the trend of the optimal beam size is indicated by the green line. It can be seen that the optimal beam-to-core ratio becomes smaller with increasing mode order. This behavior is explainable since the beam width of higher order LG modes follows $w = w_0\sqrt{2p + l + 1}$ with w_0 the Gaussian width, while on the other hand, the LP modes are well confined within the core. This results in the observable decrease of the needed Gaussian width to match the scale of the corresponding fiber mode. Furthermore, the region where a high overlap can be achieved shrinks with increasing mode order and makes the appropriated adaptation of the scale

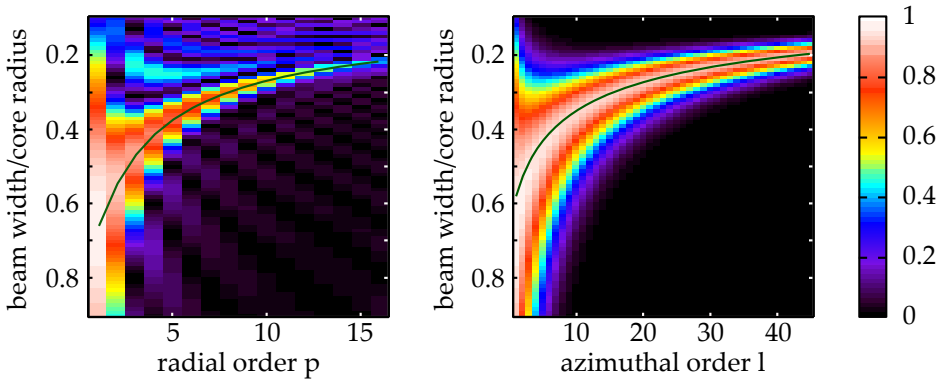

Figure 3.8: Size dependent overlap relations for modes with increasing radial and azimuthal order of a step index fiber with $V = 50$ [101]. The trend of the optimal beam size is highlighted by a green line.

parameter more crucial. In case of the higher order radial modes, it can be seen that the maximal achievable overlap decreases strongly with increasing mode order, indicating the fundamental limitation of the applied approximation. In the case of very high radial mode orders, the LP modes might be better approximated by Bessel-beams due to the Bessel-like mode solutions within the core [103].

Finally, the influence of the fiber's V-parameter on the discussed approximation is investigated. For that, the optimal beam-to-core radius ratios and the maximal achievable overlap were determined, whereas the found dependencies are illustrated in Fig.3.9. In Fig. 3.9 (a), a decrease of the optimal beam-to-core radius ratio with increasing V parameter is observable. For low V values, in the case of the LP_{01} mode or V values close to the cutoff of the higher order modes, the beam-to-core radius ratios are comparatively large indicating the bad confinement of the modes within the core. At first, the optimal beam-to-core radius ratio rapidly decreases for higher V-parameters, due to the improved light confinement. Following this, the decrease slows down for further increasing V values. In Fig. 3.9 it can be seen that for the bad confined modes, i.e. V values close to the cutoff frequency, the maximal achievable overlap is very low but increases quickly to an overall maximum at mode specific V-parameters. Afterwards the maximal overlap decreases slowly for increasing V-values allowing the application of the performed approximation over a wide V-parameter range above the modal cutoff

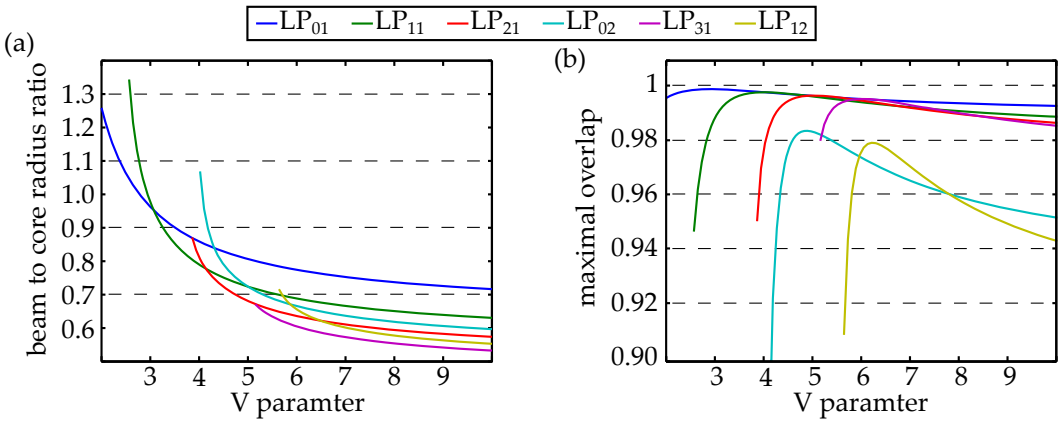

Figure 3.9: V parameter dependence of the overlap relation between the LP and corresponding LG modes [101]. (a) Optimal ratio between the Gaussian beam width and the core radius. (b) Maximal achievable overlap.

frequencies. The previously observed trend of a decline of the approximation for modes of higher radial order is also observable here.

Comprising the above discussed results it was shown that the LP modes of a step-index fiber can be approximated by a scale-adapted set of LG free-space modes. In addition, the validity of this approximation was proven experimentally for a fiber with a V parameter of 4.72. However, certain limitations have to be considered if this approximation should be applied. At first the LP modes have to be well confined within the core and to be of low radial order to provide a high overlap. Additionally, since the optimal beam-to-core radius ratio changes for each mode pair, a trade-off between required individual modal overlap and the accessible amount of modes realizable with one scale adaptation occurs. The last problem can be avoided by an individual modal size optimization for highly multi mode fibers, or at least for different groups of modes.

3.2.2 Excitation of LP Fiber Modes by a Digital Laser

The possibility to approximate the lower order LP modes of a step index fiber by LG modes, as shown in the previous section, enables fiber excitation directly by free-space resonator laser sources to overcome the low efficiency issue of free-space beam shaping techniques. For that, the intra-cavity beam shaping technique

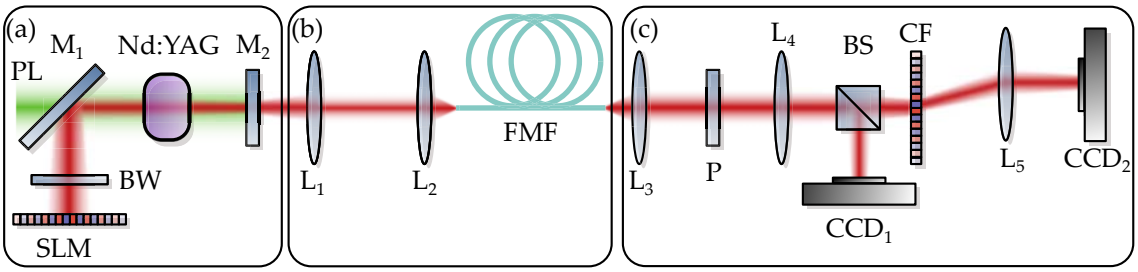

Figure 3.10: Setup for the selective excitation of fiber modes by a intra-cavity beam shaping and its characterization [102], (a) the digitally controlled solid state laser source for beam shaping, (b) the optical fiber link, (c) modal decomposition setup. SLM, spatial light modulator; BW, Brewster window; PL, pump light; $M_{1,2}$, Mirrors; Nd:YAG, laser crystal; L_{1-5}, lenses; FMF, few mode fiber; P, polarizer; BS, beam splitter; CF, correlation filter; $CCD_{1,2}$, camera

introduced in Sec. 2.2.2 pp. 18 is used to generate adapted LG modes directly by the light source, which correspond to the intended fiber modes. To evaluate the capabilities of this selective fiber mode excitation procedure, in a first step, the intra-cavity shaped mode fields are modally decomposed in terms of the LP mode set supported by the fiber. In a second step the generated modes are coupled into the fiber and the transmitted mode spectrum is analyzed. In the following, the achieved results will be presented [102].

The setup used for the direct fiber mode excitation with a solid state laser source is depicted in Fig. 3.10. The layout of the light source, the so called digital laser [61], is shown in Fig. 3.10 (a), where the 1% doped Nd:YAG crystal (4 mm diameter, 30 mm length) was placed in a L-shaped resonator built by a reflective spatial light modulator (SLM) (Hamamatsu LCoS X 10468 E with 800×600 pixels of pitch 20 μm and reflectivity > 90% on the vertical polarization calibrated for a 2π phase shift at $\lambda = 1064$nm) as a back reflector, a high reflective planar mirror M_1, and a plane 60% output coupler M_2. The output power could be varied by the adjustment of the diode pump PL (Jenoptik JOLD 75 CPXF 2 P W) power. Using the complex amplitude modulation technique at the SLM the mode order and size were controllable. Afterwards, the generated fields were coupled by a $4f$ telescope formed by the lenses L_1 and L_2 ($f_{L_1} = 200$ mm, $f_{L_2} = 10$ mm) into a

large mode area fiber (Nufern LMA-GDF-25/250-M) with a core diameter of 25 μm and an NA of 0.065. This results in a V parameter of 4.72 at the operation wavelength of 1064 nm and the existence of six guided modes. The fiber had a length of about 30 cm to avoid strong mode coupling and attenuation effects in order to investigate mainly the coupling process at the fiber front face without strong perturbation by the fiber propagation properties. In a last step, depicted in Fig. 3.10 (c), the fiber output was 40× magnified and imaged by a second telescopic $4f$ setup consisting of lenses L_3 and L_4 (f_{L_3} = 10 mm, f_{L_4} = 400 mm) into the plane of the correlation filter CF and the camera CCD_1, separated by the beam splitter BS, allowing for the simultaneous detection of the modal coefficients and the near-field intensity distribution. For the final measurement of the correlation signals the light after the CF was optically Fourier transformed by lens L_5 (f_{L_5} = 200 mm) in $2f$ configuration into the plane of the camera CCD_2. By leaving out the middle part of the setup the direct investigation of the digital laser output was possible.

At first the quality of the generated and excited modes is evaluated by imaging the laser and fiber output, respectively, on a CCD camera. The recorded intensity distributions for the five lowest order modes and the corresponding SLM phase patterns are depicted in Fig. 3.11. In Fig. 3.11 (a)-(e) the principle mode structure can be seen in the phase pattern by the high loss lines forcing the laser cavity to oscillate at the desired mode. The matching of the mode size for the maximum excitation efficiency is done by an appropriate choice of the aperture size and phase curvature. The intra-cavity shaped mode fields at the laser output are illustrated in Fig. 3.11 (f)-(j) and show a high compliance with the expected intensity distributions denoted in the insets. In a next step the generated fields are coupled into the step index fiber for selective mode excitation and the transmitted field distributions, shown in Fig. 3.11 (k)-(o), are recorded afterwards. It can be seen that the principle mode structure resembles the theoretical expectation, only the LP_{11} modes show a rotation of the lobe like pattern by nearly 45° with respect to the initially coupled orientation. In a second step, the generated and excited optical fields are analyzed by a complete modal decomposition applying the correlation

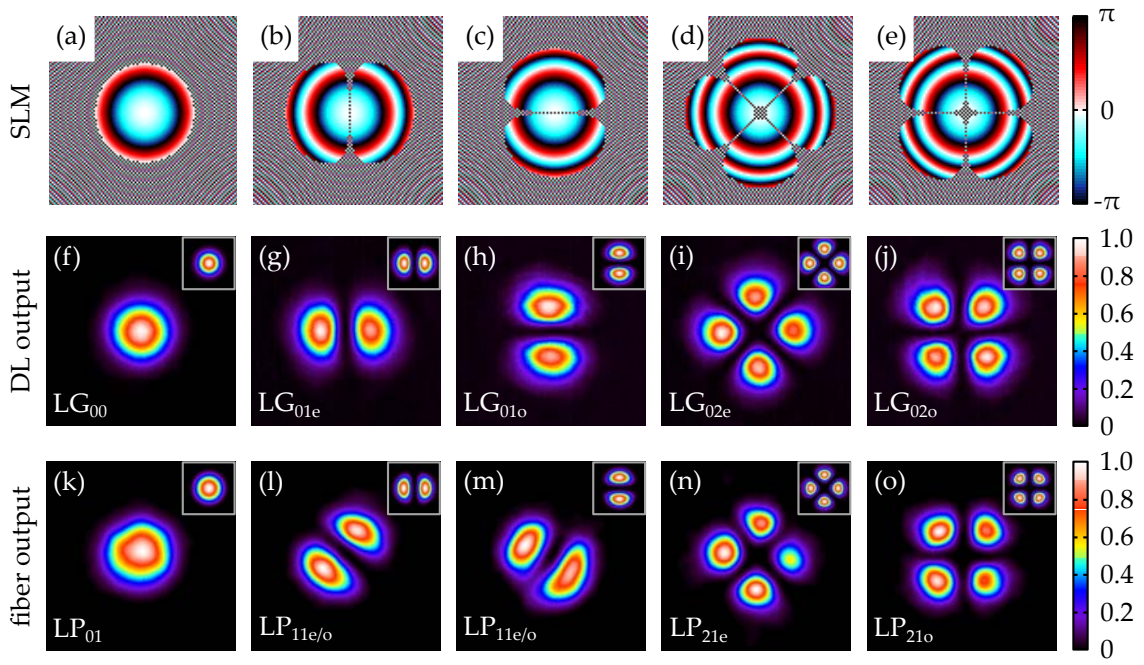

Figure 3.11: Results of the intra cavity beam shaping [102]; (a)-(e) applied phase holograms on SLM, (f)-(j) shaped modes at the laser output, (k)-(o) transmitted mode after selective fiber mode excitation. Insets denote the theoretical field distributions.

filter method. Both the laser and the fiber output, are decomposed in terms of the supported fiber modes, which enables the validation of the excitation strategy by comparison of the mode spectra, as depicted in Fig. 3.12. The modal power spectrum of the digital laser before coupling into the fiber is shown in Fig. 3.12 (a), where it can be seen that the desired modes, indicated by the red arrow, have the main contribution with > 90% of the mode spectrum. This confirms, beside the quality of the recorded intensity distribution [Fig.3.11 (f)-(j)], the ability of the digital laser to selectively address the different modes of the fiber. After injecting the mode fields into the fiber and the modal decomposition is performed on the transmitted beam. The resulting mode spectrum is shown in Fig. 3.11 (b). After the fiber, the high selectivity of the modal excitation is still preserved with exception of the LP_{11} modes, which show a nearly equal contribution by excitation with the LP_{11e} or LP_{11o} mode, respectively. As already discussed in Sec. 3.1.2, both modes are degenerated with respect to their effective indices. This makes

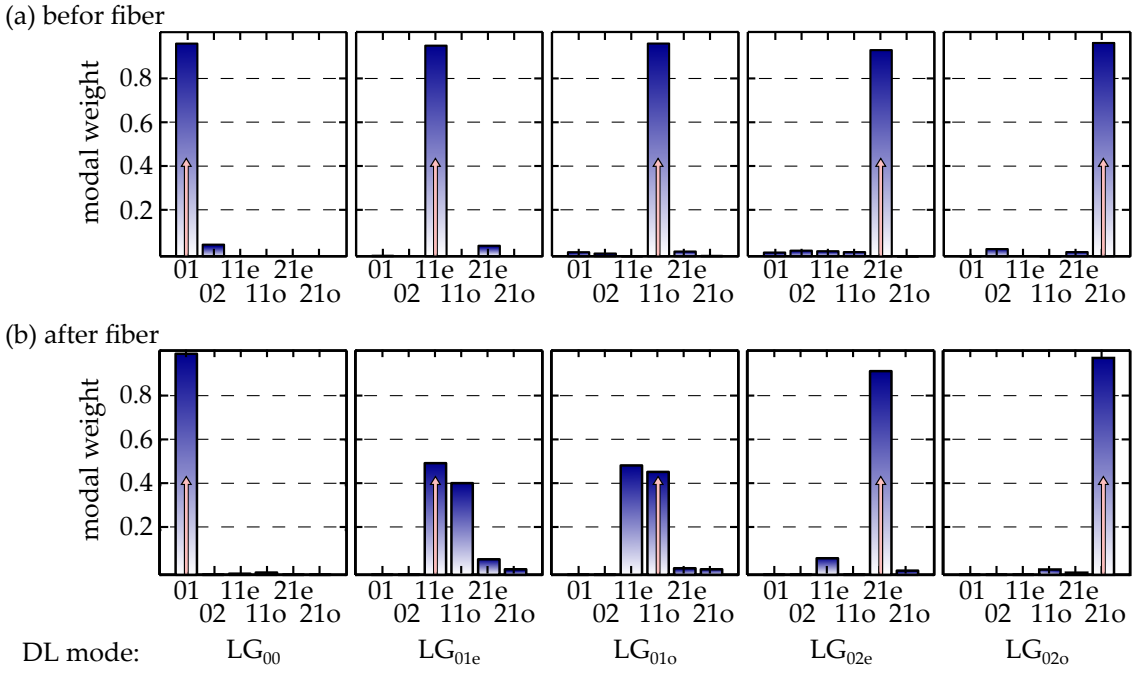

Figure 3.12: LP mode spectrum of the digital controlled laser cavity (a) before injecting into the fiber and (b) the transmitted fiber signal. The arrows are indicating the intended mode.

them likely to couple during propagation and explains the modal crosstalk, which causes the observed rotation of the intensity distribution, shown in Fig. 3.11 (l) and (m). Taking this well known crosstalk behavior into account, for the evaluation of the coupling purity of the LP_{11} mode, the added excitation strength of both the LP_{11e} and the LP_{11o} modes were considered. The quantitative evaluation and comparison of the selective excitation quality is done by using the completeness of the LP mode set $\sum_n \rho_n^2 = 1$ and calculating the modal purity (MP), which is given by

$$\mathrm{MP}_{lp} = 10 \log_{10} \left[\frac{\rho_{lp}^2}{1 - \rho_{lp}^2} \right], \tag{3.15}$$

where ρ_{lp}^2 is the individual power contribution of the intended mode. Table 3.1 summarizes the achieved modal purity for the laser output (upper row) and the transmitted signal (lower row). It can be seen that for all modes a high MP of about

Mode:	LP_{01}	LP_{11e}	LP_{11o}	LP_{21e}	LP_{21o}
MP_{lp} (DL):	12.8dB	11.9dB	12.8dB	10.6dB	12.8dB
MP_{lp} (at fiber output):	18.5dB	9.8dB	12.3dB	9.9dB	14.7dB

Table 3.1: Measured mode purity at the digital laser's output (upper row) and after passing the few mode fiber (lower row) [102].

10 db is achieved, demonstrating the ability of the presented intra-cavity mode shaping technique for selective fiber mode excitation. Besides the modal purity itself, the energy efficiency is a crucial point of beam shaping systems. Due to the additional losses introduced by the SLM which results in a increased threshold pump power in comparison to common laser systems, the energy efficiency is relatively low and decreases for higher order modes. The last fact is caused by the adding of cavity losses for the mode selection and producing a mode dependent loss (MDL) of about 7dB. This problem has to be solved in future developments and is not considered in this thesis. Without regard to the MDL of the DL, the MDL of the coupling process itself was below 1.5 dB.

In conclusion, the aim of addressing specific modes in an optical few-mode fiber directly from the laser source with a high modal purity of about 10 dB was successfully realized. Further improvements could be achieved by more sophisticated field generation approaches in the DL, like reverse propagation techniques [52] which enable the excitation of arbitrary modal superpositions.

3.3 Combined Free-Space Fiber Communication Link

A promising application of the spatial modes, for fiber as well as free-space beams, is the enhancement of the data transmission capacity in optical communication networks by introducing new degrees of freedom for data multiplexing [15]. To do so, similar to already established multiplexing techniques incorporating time- [104], wavelength- [105], amplitude-, phase-, and polarization-division [106] multiplexing, additional parallel and independent data channels can be introduced exploring the spatial domain either with independent light paths in space-division-

multiplexing [15] or co-propagating but orthogonal spatial modes, the so called mode-division-multiplexing (MDM). By the combination of multiple degrees of freedom, data transmission rates of about two petabits (10^{15} bits) per second were demonstrated through a single optical fiber [107, 108].

However, the majority of broadband users have no access to the fiber-optic networks and as such, alternative communication links are required to breach the so called 'last-mile' problem, i.e. bridging the main-stream communication links with those of businesses and households [109]. One solution is optical wireless communication that incorporates free-space optics (FSO) [110]. Such FSO communication links were demonstrated to enable more than 100 terabit (10^{12} bits) per second data capacity with three-dimensional multiplexing [111].

The successful conjunction of FSO and optical fibers was shown for optical code division multiplexing [112] as well as for wavelength-division multiplexing techniques [113]. In this section, a solution for the 'last-mile' problem is discussed which incorporates MDM and an integrated communication link consisting of free-space and fiber transmission [114]. For that a common mode set for both types of links, fiber and free-space, was used to avoid additional demultiplexing/multiplexing steps between the different media. Hence, a direct transmission of the signal from the sender to the transmitter was possible.

3.3.1 Properties of Gradient Index Fiber Links

For an optical link across two disparate media (free space and fiber), a core requirement is the existence of a common set of spatial modes that are eigenstates of both. In case of single mode fibers, this is easy due to the Gaussian like fundamental mode of typical fibers. However MDM requires multiple modes. Since in general the geometry of the two media differs, so do the corresponding modes. The commonly used step-index fiber lack this complete matching and can only be approximated by free-space modes with some limitations (see for details Sec. 3.2 pp. 39). However, to overcome this limitation a graded index fiber with parabolic refractive index profile [38] of the core was used to provide a mode set

that is a solution of the paraxial Helmholtz-equation in cylindrical coordinates too. These modes are also known as LG modes. The transverse field structure of the LG modes at the waist position is defined by Eq. (3.10) p. 42.

Graded index fibers with a nearly parabolic index profile are well known for short range communication networks, but typically have core diameters of 50 μm and are highly multi-mode. To reduce the number of modes of such a multi-mode system to a reasonable amount, a custom graded index fiber with a parabolic index profile and core diameter of 9.5 μm was fabricated at the Leibniz Institute of Photonic Technology. The refractive index difference between core center and cladding is $\Delta n \approx 3.3 \times 10^{-2}$. The customized fiber was fabricated by a rod-in-tube procedure starting with a primary germanium doped preform. Using the modified chemical vapor deposition technique, layers with an increasing amount of germanium were deposited in order to realize the needed continuous refractive index profile. The maximum GeO_2 concentration was 24 mol% in the core center. Afterwards the tube was collapsed to the final primary preform with an outer diameter of 26 mm and a core cladding ratio of 1:2. In an intermediate step the core preform was drawn to a cane of 2 mm diameter and stacked into a tube of pure quartz glass with an inner and outer diameter of 2.4 mm and 15 mm, respectively. Finally the resulting preform was drawn to the design fiber core diameter of 9.5 μm. In Fig. 3.13 (a) the measured refractive index profile of the fiber preform in comparison to the intended parabolic one is depicted, which shows a high agreement between both. This ensures the perfect matching between the mode sets of free-space and the fiber. The additional occurring refractive index peaks in the center of the core are caused by the evaporation and diffusion process of GeO_2 during the collapsing of the primary preform [115].

For the determination of the guided modes and the corresponding effective refractive indices of the used fiber, a finite differences numerical mode solver was used [42]. The resulting eigenvalue spectrum is shown in Fig. 3.13 (b). It can be seen that seven discrete well separated mode groups occur building a scalar mode set containing 28 modes. For the degenerated modes within such a mode group

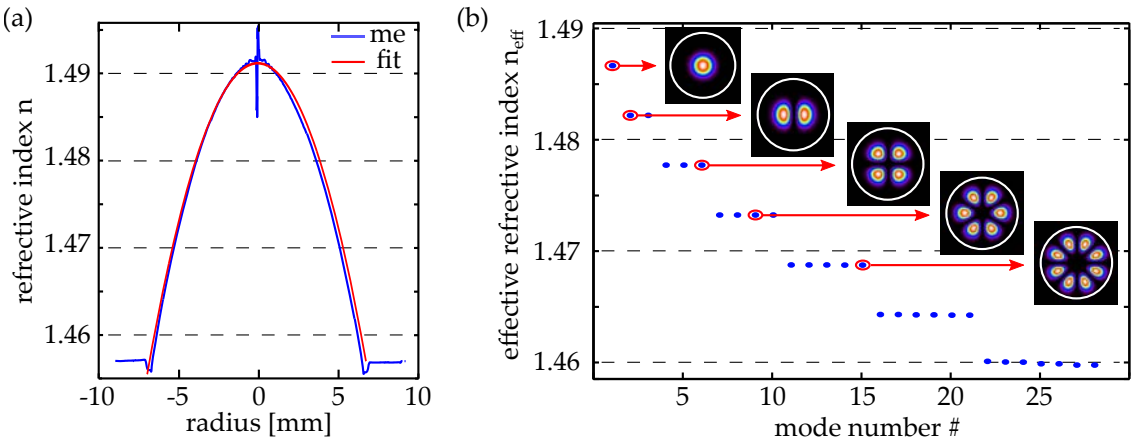

Figure 3.13: Refractive index profile of the parabolic graded index fiber (a) and the effective refrective index spectrum of the corresponding modes at a wavelength of 632 nm (b). Insets depict the intensity distribution of the fiber modes chosen for the MDM, where the white circles indicate the fiber core [114].

the value $2p + l$ is constant, which resembles the condition as for a constant Gouy phase in the corresponding free-space LG mode set. The occurrence of the same degeneracy condition with respect to the effective refractive index or the Gouy phase in the fiber and free-space modes, respectively, is an additional confirmation of the structural similarity of both mode sets. To prove the exact correspondence between the numerically determined fiber mode set and the analytical calculated free-space modes, the overlap relation between both sets was determined to be higher than 0.99 for the 21 lowest order modes. For higher order modes, especially for higher radial orders, the finite extension of the parabolic profile causes a distorted field distribution in the fiber cladding and thus a mismatch with respect to the free-space modes.

Since the modes forming a mode group are degenerated regarding their propagation constant, they are likely to couple during propagation, whereas the large eigenvalue spacing between the mode groups typically suppresses considerable modal crosstalk [99, 116]. This characteristic is taken into account by applying a mode group division multiplexing scheme where the information is encoded in one mode per mode group and decoded by considering the whole mode group

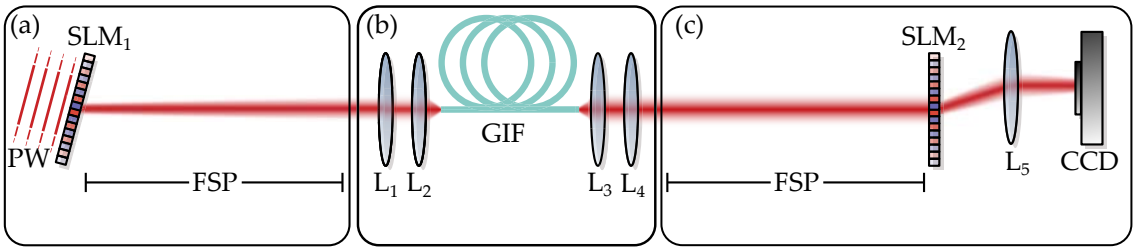

Figure 3.14: Setup for the data transmission through a free-space to fiber communication link, (a) the encoding of information into the spatial modes and first free-space part, (b) the transmission of the optical signal through the fiber link, (c) second free-space part and modal decomposition setup for the information decoding. PW, plane wave; $SLM_{1,2}$, spatial light modulator; FSP, free-space propagation; L_{1-5}, lenses; GIF, graded index fiber; CF, correlation filter; CCD, camera.

response. Hence, the crosstalk between the independent modal transmission channels can be minimized. The modes chosen from the first five mode groups, which are used for MDM, are depicted in the insets of Fig. 3.13 (b). Since the last two mode groups showed considerably high transmission losses, they were excluded from the experiment.

3.3.2 Data Transmission through a Free-Space to Fiber Communication Link

For the characterization of the composite communication link and the proof of principle of the transmission of information encoded into spatial modes, the setup depicted in Fig. 3.14 was used, where plane wave illumination at $\lambda = 633$ nm was applied as light source. In a first step the SLM_1 (Holoeye, HEO1080-P with 1920 $\times$ 1080 pixels of pitch 8 μm and calibrated for a 2π phase shift at $\lambda = 1064$ nm) was used to shape the required mode fields, as described in Sec. 2.2.1 pp. 16, which propagated through the free-space link of about 1.5 m. In order to provide the required matching of the beam size between the free-space and fiber link, the free-space beam was de-magnified by a telescopic setup in $4f$ configuration using lenses L_1 and L_2 ($f_{L_1} = 500$ mm and $f_{L_2} = 4$ mm). Afterwards the fiber link with a length of about 1.5 m followed before a second $4f$ telescope ($f_{L_3} = 4$ mm and

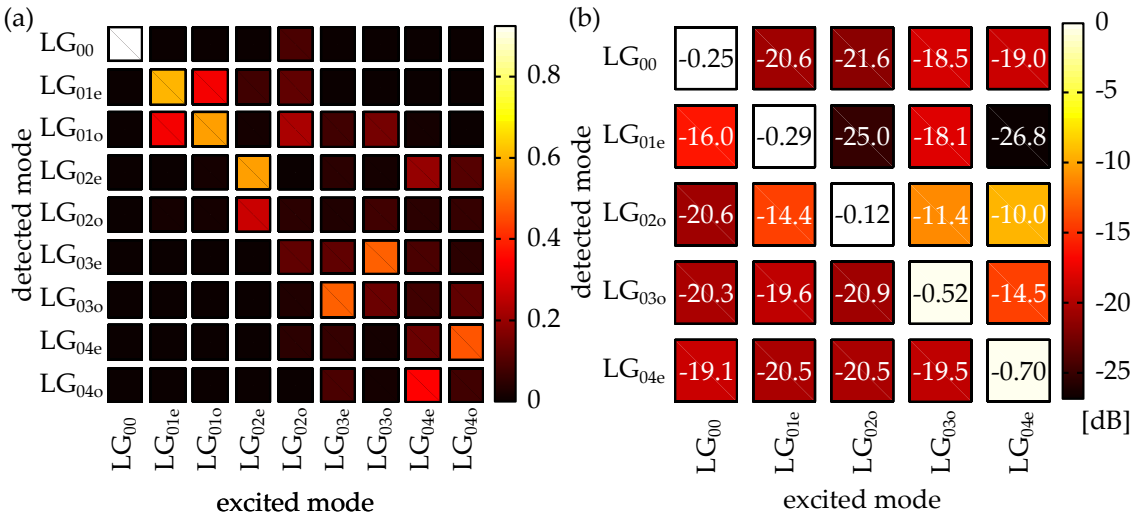

Figure 3.15: Transmission matrices of the combined free-space fiber link for (a) the azimuthal modes of the five lowest order mode groups and (b) the established communication link [114].

f_{L_4} = 400 mm) magnifies the fiber output back to a collimated free-space beam. In a last step after a second free-space link of about 1.5 m the beam was modally decomposed for retrieving the sent information. For that, the correlation filter method introduced in Sec. 2.3 pp. 19 was used, given by SLM_2 as a correlation filter, the L_5 in $2f$ (f_{L_5} = 200 mm) configuration, and the camera CCD as a detector.

At first the realized composite link of two free-space parts and one fiber part with an overall length of about 4.5 m was characterized by a MIMO measurement similar to that described in Sec. 3.1.2 pp. 34 to quantify deleterious effects like fiber stress, optical aberrations and turbulences. For that the transmission matrix for the azimuthal modes of the five lowest order mode groups was determined. The results are depicted in Fig. 3.15 (a). It can be seen that the transmission matrix has mainly contributions at the main and the two minor diagonals, indicating that in the case of crosstalk, mainly degenerated modes are involved. Considering the determined mode coupling, it was possible to determine for each mode group a pair of input and output modes which can be used for the MDM procedure and provide a sufficient signal purity. The pairs were chosen to be LG_{00}/LG_{00}, LG_{01e}/LG_{01e}, LG_{02o}/LG_{02e}, LG_{03e}/LG_{03o} and LG_{04o}/LG_{04e}. The

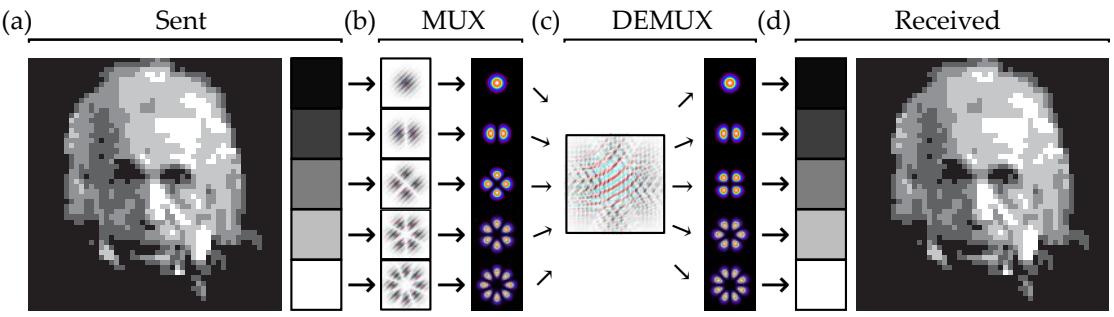

Figure 3.16: MDM scheme for the transmission of a gray scaled image of Einstein. (a) The image to be send and the contained gray levels, (b) the multiplexing step showing the applied SLM patterns for generating the corresponding modes, (c) de-multiplexing into the five detection mode channels and (d) reconstruction of the received image.

reduced transmission matrix describing the established links for the MDM procedure is illustrated in Fig. 3.15 (b). It shows that the link crosstalk is less than −10 dB, where the highest values were measured for higher mode groups. All additionally occurring crosstalk into non considered modes results in a overall power loss of the detectable signal strengths.

After characterizing the transmission link and identifying a suitable subset of modes to form an MDM procedure, a proof of principle realization of data transmission was done which follows the scheme illustrated in Fig. 3.16. For that, a 50-by-50 pixel gray-scale image of Einstein, shown in Fig. 3.16 (a), was transmitted pixel wise. Each pixel contained a particular gray level which was during the multiplexing step encoded into a specific mode group of the communication link. After sending the beam through the communication link, the transmitted beam was de-multiplexed in order to identify the gray value representing the received mode. For the de-multiplexing hologram, the spatial multiplexing technique introduced in Sec. 2.3.3 pp. 24 was applied for the simultaneous detection of all five mode channels. Finally, the received image was reconstructed by decoding the detected modes back into gray values of the image pixel. Since the five most distinct mode pairs were chosen from the crosstalk data the probability of an incorrect mode detection was expected to be low and a perfect image was received as shown in Fig. 3.16 (d).

Chapter Summary

In this chapter the capabilities of the correlation filter method to decompose scalar laser beams were demonstrated. At first an example decomposition and field reconstruction was shown and discussed in Sec. 3.1.1. The success of this procedure was proven by the high cross correlation value of 0.98 between measured and reconstructed intensity distribution. Afterwards the correlation filter method together with a holographic beam shaping technique was used to investigate the fiber transmission by multiple-input-multiple-output measurements. The gained information was subsequently used for signal-processing by applying the inverse fiber transmission matrix in Sec. 3.1.2. Here, the possibility for the reconstruction of the initial excited field distribution as well as the tailoring of arbitrary output field distributions highlight the validity of the determined transmission matrix. Additionally, the matching of free-space and fiber mode sets were theoretically and experimentally investigated in Sec. 3.2. This led to the selective fiber mode excitation by a digitally controlled solid state laser source with a modal selectivity of about -10 dB. Finally, the ability of shaping and decomposing optical modes was used for the realization of a proof of principle demonstration of mode division multiplexing through a multiple media communication link, comprising of free-space and fiber parts, by the suitable choice of a common mode set. To demonstrate the capabilities of this concept a gray-scale image was modally encoded and successfully transmitted and reconstructed through the combined communication link.

4 | Modal Decomposition of Partial Coherent Optical Fields

In the previous chapter the modal decomposition and reconstruction of coherent light fields was performed under the assumption of a single frequency light source. In reality this is only an approximation and each real light source possesses a finite spectral width. Consequently, for the description of modal superpositions partially coherent conditions have to be expected in general. To take account of this general case, a modified phase measurement procedure will be introduced to advance the correlation filter method and enable the reconstruction of partially coherent modal superpositions. Afterwards, this new capability will be used to reconstruct partially coherent fiber beams and to determine the effect of fiber propagation on this general class of optical beams.

4.1 Partial Coherent Superposition

In this section the picture of a multi-mode interference for the reconstruction of modal superpositions will be derived, including the introduction of the mutual modal degree of coherence. Additionally, the effect of the degree of coherence on the beam profile is discussed. Afterwards, a modification of the phase measurement procedure will be outlined which enables the determination of the additional required coherence parameter for the description of partially coherent superpositions.

4.1.1 Multi-Mode Interference

The measurable intensity distribution of a modal superposition is defined as the time averaged squared absolute value of the optical field $U(\mathbf{r}, t)$

$$I_{ges}(r) = \langle U(\mathbf{r}, t) U^*(\mathbf{r}, t) \rangle = \left\langle \left[\sum_n^{n_{max}} \rho_n e^{i\varphi_n(t)} \psi_n(r) \right] \left[\sum_n^{n_{max}} \rho_n e^{-i\varphi_n(t)} \psi_n^*(r) \right] \right\rangle , \quad (4.1)$$

with $\langle\rangle = \frac{1}{T} \int_0^T \mathrm{d}t$ expressing the time average. In terms of modal superpositions, the time dependence of the optical field introduced by the finite spectral width of the light source is constituted by a time dependent inter-modal phase delay $\Delta\varphi_n(t)$. This time delay has to be considered for the intensity reconstruction under quasi-monochromatic conditions. Considering each mode $\psi_n(\mathbf{r})$ as a single beam, Eq. (4.1) leads analogously to classical interferometry to a multi-mode interference law

$$I_{ges}(r) = \sum_{n,m}^{n_{max}} \rho_n \rho_m \left|\psi_n(r)\right| \left|\psi_m(r)\right| |\gamma_{nm}| \cos\left[\Delta\varphi_{nm} + \Delta\chi_{nm}(r)\right] , \quad (4.2)$$

where ρ_n denotes the power contribution of the respective mode, $\Delta\phi_{nm}$ is the inter-modal phase difference, and $\Delta\chi_{nm}(\mathbf{r}) = \arg[\Psi_n(\mathbf{r})] - \arg[\Psi_m(\mathbf{r})]$ defines the phase difference between the individual spatial mode functions. The consequence of the time averaging is given by the mutual modal degree of coherence $|\gamma_n m|$ and can take values of

$$\begin{aligned} |\gamma_{nm}| &= 1 && \text{coherent limit,} \\ 0 < |\gamma_{nm}| &< 1 && \text{partial coherence,} \\ |\gamma_{nm}| &= 0 && \text{incoherent limit.} \end{aligned} \quad (4.3)$$

Typically the coherent limit is assumed for a single frequency laser with narrow spectral line width as used in the experiments in Ch. 3 pp. 31 i.e. only optical path differences occur which are small compared to the coherence length. The lower limit of incoherent light is typically found for broad band light sources, e.g. white light, or large path differences compared to the coherence length, respectively.

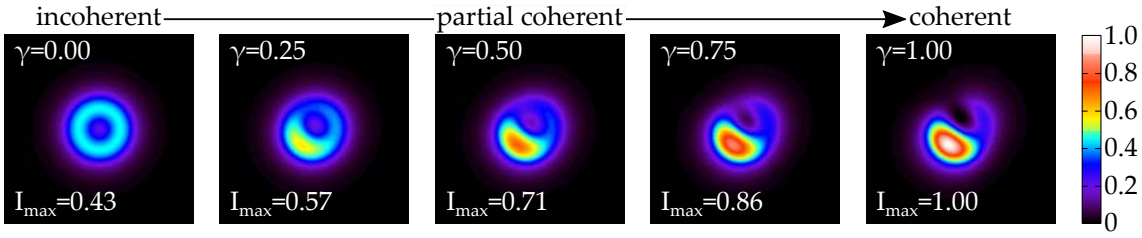

Figure 4.1: Example of modal superposition of LP_{01}, LP_{11e} and LP_{11o} modes with increasing degree of coherence

In all intermediate cases, partially coherent conditions have to be considered in general. A typical mode system where an incoherent superposition can be found are multi-mode beams originate from free space resonators. Within these, different modes oscillate independently and no stable phase difference exists. On the other hand, the coherent case occurs for example by diffractive mode shaping out of a spatial coherent input beam like a plane wave. Hence, depending on the origin of the multi mode character of a beam, only one of these limiting cases is considered. The general case of partially coherent superpositions is of importance for propagating multi-mode beams in media which suffer from modal dispersion as given by optical fibers. The impact of the modal degree of coherence on the intensity distribution of a modal superposition and the associated changes are shown in Fig. 4.1. For an increasing degree of coherence a decrease of symmetry can be observed, starting from a perfect point symmetric distribution in the incoherent limit. A second effect concerns the maximum intensity value. Due to the asymmetry of the coherent superposition, the appearance of local hot spots with increased peak intensity is possible.

4.1.2 Determination of the Degree of Coherence

For the reconstruction of partially coherent superpositions in addition to the knowledge about the modal weights and the inter-modal phases used in Ch. 3 pp. 31, the mutual degree of coherence between the individual modes has to be determined. Ferreira and Belsley [117] have shown that the required spatial coherence analysis is realizable by dual-mode holographic interferometry. Analogous to this, additional filter functions for the phase measurement procedure of

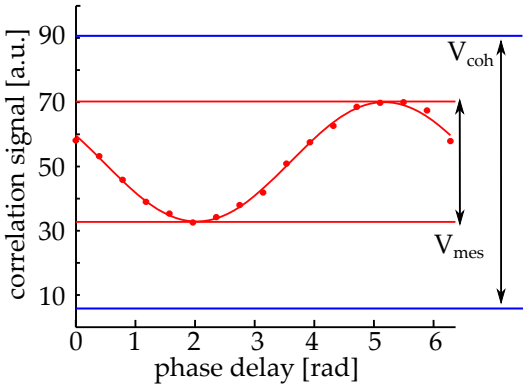

Figure 4.2: Example of a two mode interferogram with denoted measured visibility in comparison to the expected one for a coherent superposition

the CFM are required, where the complete two mode interference is evaluated for each mode pair $\psi_n(\mathbf{r})$ and $\psi_m(\mathbf{r})$. To do so, interferometric transmission functions of the form

$$T(\mathbf{r}, \phi) = \psi_n(\mathbf{r}) + e^{i\phi}\psi_m(\mathbf{r}), \tag{4.4}$$

with ϕ being the additionally introduced phase shift between the modes, are applied. Following Eq. (2.19) p. 23, the correlation signal in the detection plane becomes

$$I(\phi) = \rho_n^2 + \rho_m^2 + 2\rho_n\rho_m|\gamma_{nm}|\cos(\Delta\varphi_{nm} + \phi), \tag{4.5}$$

which is the classical two beam interference law for the two implemented modes. The implementation of multiple channels for the two beam interference transmission functions [Eq. (4.4)] with different additional phase shifts ϕ, enables the recoding of the full two beam interference pattern as depicted in Fig. 4.2 where the two beam interference of a partially coherent superposition between the LP_{01} and LP_{11e} mode is depicted. The high quality of the measured interferogram is indicated by the nearly perfect accordance between the experimental data and the theoretical cosine fit. Comparing the measured visibility V, defined as

$$V = \frac{I_{max} - I_{min}}{I_{max} + I_{min}}, \tag{4.6}$$

of the two beam interference, indicated by the red lines, with the theoretically expected one for the coherent case, highlighted by blue lines, reveals the partially coherent character of the investigated superposition. Like in classical interferometry, the inter-modal phase difference $\Delta\varphi_{nm}$ and the mutual modal degree of coherence $|\gamma_{nm}|$ are determinable by the application of appropriate phase shift procedures. During this thesis, a four step algorithm with $\frac{\pi}{2}$ phase steps was used which resulted in phase shifts of 0, $\frac{\pi}{2}$, π and $\frac{3\pi}{2}$, respectively. Hence, the mutual modal interference could be evaluated to

$$A_{nm} = \rho_n^2 + \rho_m^2 = \frac{1}{4}\left[I(0) + I\left(\tfrac{\pi}{2}\right) + I(\pi) + I\left(\tfrac{3\pi}{2}\right)\right] \tag{4.7}$$

$$B_{nm} = 2\rho_n\rho_m|\gamma_{nm}| = \frac{1}{4}\sqrt{[I(0) - I(\pi)]^2 + \left[I\left(\tfrac{\pi}{2}\right) - I\left(\tfrac{3\pi}{2}\right)\right]^2} \tag{4.8}$$

$$\Delta\varphi_{nm} = \arctan\left[\frac{I\left(\frac{\pi}{2}\right) + I\left(\frac{3\pi}{2}\right)}{I\left(0\right) - I\left(\pi\right)}\right], \tag{4.9}$$

where A_{nm} are the sums of the individual modal powers, B_{nm} expressing the modulation strengths which contain the information about the degrees of coherence, and $\Delta\varphi_{nm}$ the inter-modal phase differences. Thus the mutual modal degree of coherence could be determined by the ratio between modulation strength and the separately measured modal weights ρ_n and ρ_m to

$$|\gamma_{nm}| = \frac{B_{nm}}{\sqrt{B_{nn}B_{mm}}} = \frac{B_{nm}}{2\rho_n\rho_m}. \tag{4.10}$$

As a result of this new phase measurement procedure, all required parameters for the reconstruction of quasi-monochromatic optical fields in terms of a partially coherent superposition are accessible by the advanced correlation filter method. The drawback of this improved measurement capability is an tremendous increased amount of $2n^2 - n$ needed transmission functions in the filter for the partially coherent field reconstruction compared with $3n - 2$ for the full coherent case, where n defines the amount of possible modes.

4.2 Experimental Results

After introducing the required modification of the phase measurement procedure for the determination of the mutual modal degree of coherence, the advanced correlation filter method will be exploited to decompose and reconstruct partially coherent modal superpositions. Additionally the impact of modal dispersion and mode coupling on the degree of coherence will be investigated, which enables useful insights into the fiber's transmission properties.

4.2.1 Reconstruction of Partial Coherent Superpositions

To evaluate the performance of the new decomposition and reconstruction scheme, partially coherent modal superpositions were coupled into a short piece of a common step index fiber ($V = 2.67$, $d_{core} = 7.7\mu$m), which supports the three lowest order LP modes. Since the direct creation of partially coherent superpositions is quite challenging, although it is the most general case, the preparation of the coherent and the incoherent contributions was separated into two steps. For the creation of the incoherent part, an end pumped Nd:YAG laser emitting at 1064 nm with adjustable pump positioning was used. This special laser design enables the generation of Hermite-Gaussian (HG) modes of higher orders in the horizontal direction [118] at certain pump positions. At intermediate positions the laser cavity emits beams composed by an incoherent superposition of two HG modes of neighboring order. Following the results found in Sec. 3.2 pp. 39 that low order free-space modes are good approximations for step index fiber modes, an incoherent superposition of HG_{00} and HG_{10} modes was used to excite an incoherent superposition of the corresponding LP_{01} and LP_{11e} modes in the fiber. The excitation of an additional coherent contribution was performed by a phase plate which shifted the phase of a spatial region of the beam by π. By a transversal movement of the phase plate, the phase shifted amount of the beam was changeable and thus the LP_{01} to LP_{11e} excitation ratio could be adjusted by controlling the overlap of the modified beam with the corresponding modes. The combination of both techniques allows the excitation of partially coherent modal superposition, where

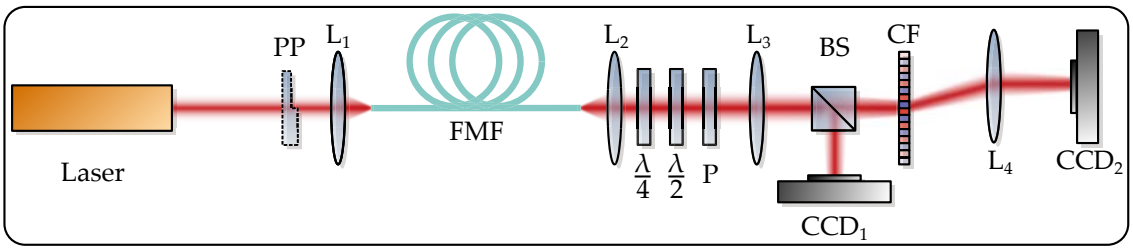

Figure 4.3: Setup for the determination of the modal degree of coherence. Laser, Nd:YAG laser; L_{1-4}, lenses; PP, phase plate; FMF, few mode fiber; $\frac{\lambda}{4}$, quarter wave plate; $\frac{\lambda}{2}$, half wave plate; P, polarizer; BS_1, beam splitter; CF, correlation filter; CCD_{1_3}, cameras. Dashed elements not always used.

the degree of coherence is controlled by adjusting the strength of the coherent and incoherent contribution.

Figure 4.3 depicts the setup for the creation and decomposition of the partially coherent fiber mode superpositions. The laser and the phase plate were used to generate partially coherent input states, as described. Afterwards the light field was coupled into the fiber by a microscopic objective (f_{L_1} = 10mm). On the evaluation side, a $4f$-setup consisting of the lenses L_2 and L_3 (f_{L_2} = 4mm, f_{L_3} = 600mm) provides an 150× magnified image of the fiber end face in the plane of the CF for modal decomposition and in the plane of CCD_1 for classical near-field imaging simultaneously due to the beam splitter. The CF was realized by an SLM (Hamamatsu LCoS X 10468-03 with 800 x 600 pixels of pitch 20 μm calibrated for a 2π phase shift at λ = 1064nm). Finally the optical Fourier transformation of the transmitted light was performed by the lens L_4 (f_{L_4} = 375mm) in $2f$ configuration and the correlation signals were recorded with the second camera CCD_2. The polarization state of the analyzed beam was controlled by a combination of a quarter-wave plate, half-wave plate and polarizer P.

A selected decomposition result with the corresponding reconstructed intensity distribution is shown in Fig. 4.4. To visualize the necessity of the applied partially coherent reconstruction, the measured intensity distribution emerging from the fiber is compared to all three reconstruction cases, i.e. incoherent, coherent and partially coherent assumption, as seen in Fig. 4.4 (a) and (b) respectively. For the

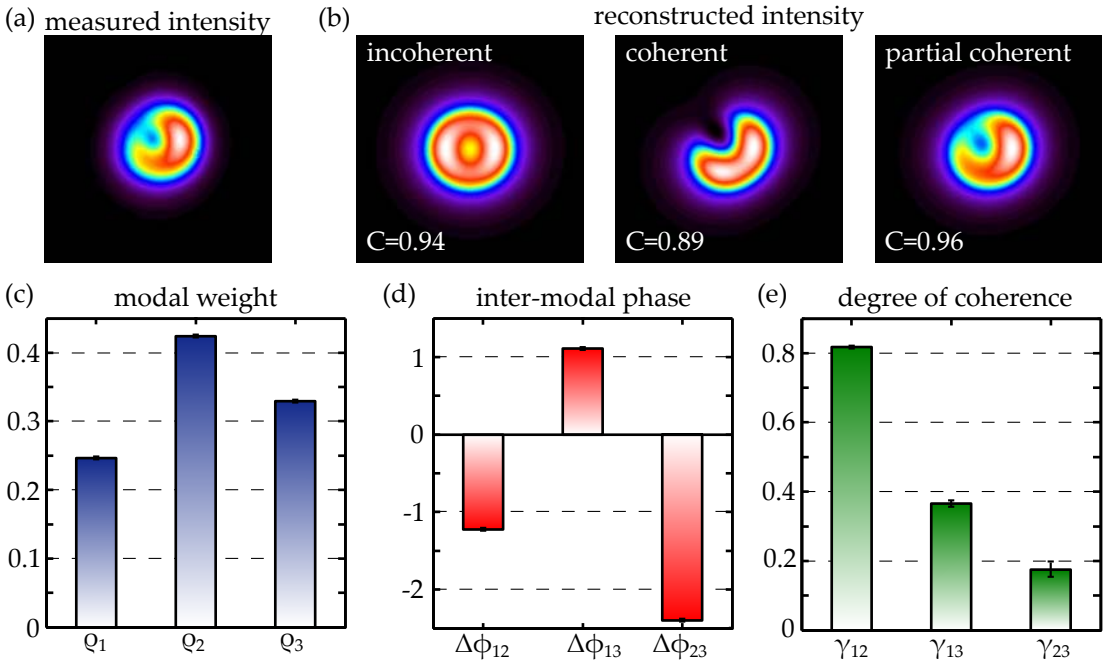

Figure 4.4: Partial coherent modal decomposition with (a) the measured intensity distribution, (b) the reconstructed intensity distribution, (c) the modal weights, (d) the inter-modal phases and (e) the mutual degree of coherence.

incoherent case, only the measured modal weights spectrum depicted in Fig. 4.4 (c), is considered and the individual modal intensities are accordingly added to a perfectly symmetric intensity distribution. Assuming a coherent superposition, the reconstruction procedure according to Ch. 3 pp. 3 was performed, which additionally takes the inter-modal phase differences depicted in Fig.4.4 (d) into account. Finally the best reconstruction is achieved by incorporating the mutual modal degree of coherence, which is shown in Fig.4.4 (e), for the reconstruction of a partially coherent superposition. Only in this last case a satisfactory intensity reconstruction is possible, which nearly equals the measured one.

It has to be noted that the determined inter-modal phase differences in the partially coherent measurement procedure are overdetermined. On the one hand they are directly measured during the determination of the modal degree of coherence, but on the other hand they also could be calculated indirectly from the relative phase differences with respect to a certain reference mode as done for the coherent measurement procedure in Ch. 3 pp. 31. This fact enables to prove

the high reliability of the phase-measurement technique by comparing both the direct and the indirect values with each other. From the phase differences of the two LP_{11} modes with respect to the fundamental mode as the reference, $\Delta\varphi_{12}$ and $\Delta\varphi_{13}$, follows a phase difference between both modes of $\Delta\varphi_{23}^{cal} = -2.3 \pm 0.1$. This equals the direct measured value of $\Delta\varphi_{23}^{me} = -2.4 \pm 0.1$ within the tolerance range of measurement error. In Fig. 4.4 (d) this high accordance can be also seen by comparing the difference of the depicted bars illustrating $\Delta\varphi_{12}$ and $\Delta\varphi_{13}$, with that showing $\Delta\varphi_{12}$.

4.2.2 Determination of Modal Coherence Length

In Ch. 2 pp. 7, the modal functions are derived under the assumption of a harmonic dependence in propagation direction z and time t. Hence, the mode field distribution ψ_n itself stays constant during propagation and only a phase difference will be accumulated

$$\psi_n(\mathbf{r}_t, z) = \psi_n(\mathbf{r}_t, 0)\exp(i\beta_n z), \tag{4.11}$$

with $\mathbf{r}_t$ the transverse coordinate. Since the propagation constant β_n represents the eigenvalue of the modes, the accumulated phase difference will be varying for each individual mode over a fixed propagation distance z. Thus, the optical path length seen by the individual modes also differs and results in the well known mode beating; the periodic change of the modal interference pattern. Due to the occurring path length difference, the fiber acts as a common path interferometer between the guided modes where the interferometric path difference between two modes is given by

$$\Delta L_{path} = \frac{\lambda\Delta\beta_{nm}}{2\pi} z_{prop}, \tag{4.12}$$

with the wavelength λ, the eigenvalue difference $\Delta\beta_{nm} = \beta_n - \beta_m$ and the propagation distance z_{prop}. Assuming complete monochromatic conditions the mode beating would be the only observable propagation effect. But natural light sources

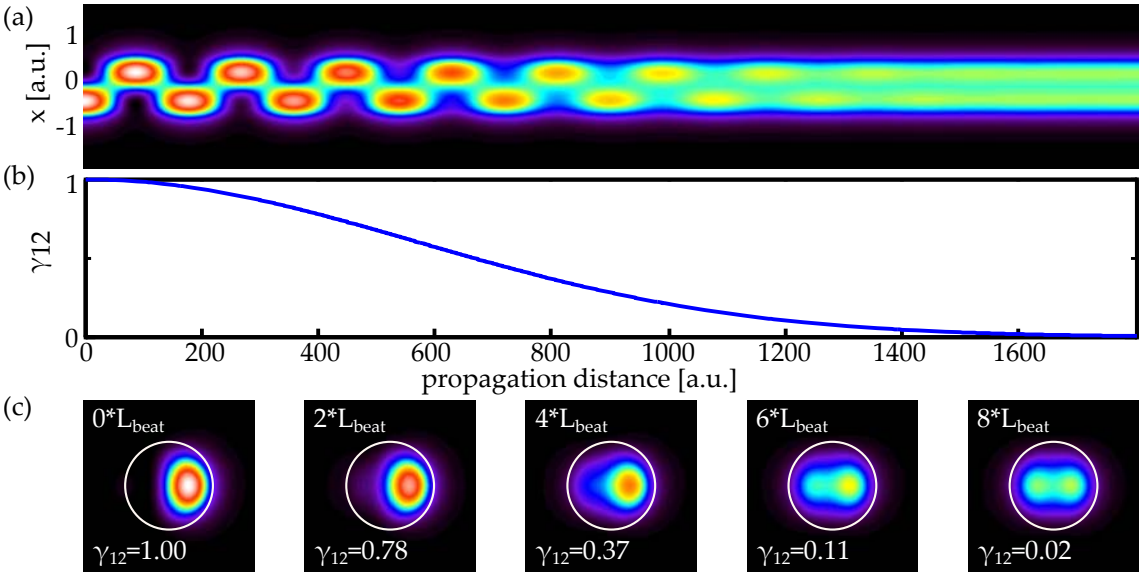

Figure 4.5: Simulation of the modal dispersion induced decrease of the degree of mutual coherence between LP_{01} and LP_{11e} during propagation; (a) fiber cross section along propagation direction, (b) degree of degree of coherence in dependence of propagation length and (c) transversal intensity distributions at a distance of zero, two, four, six and eight modal beat lengths (L_{beat}), the white circle indicates the core boundary.

and even lasers exhibit a finite spectral width which results in a limited coherence length of the modal interference during propagation. From statistical optics it is known that the degree of coherence γ is proportional to the Fourier transform of the light's spectral density $S(\nu)$ [32]

$$\gamma(\Delta L) = \left| \frac{\int_0^\infty \mathrm{d}\nu S(\nu) \exp(-2\pi i \nu \Delta L/c)}{\int_0^\infty \mathrm{d}\nu S(\nu)} \right|, \tag{4.13}$$

where ν is the frequency of light, c the speed of light and ΔL denotes the optical path difference. Hence, the visibility of the modal interference pattern will decrease with increasing propagation length and finally vanish. In Fig. 4.5 the change of the mutual modal interference pattern with respect to the propagation length is illustrated. Figure 4.5 (a) depicts the longitudinal cross section along z where at the beginning of the fiber due to the degree of coherence, the typical periodic mode beating can be observed. But with an increasing propagation

distance and a consequently decreasing high degree of coherence, as shown in Fig.4.5 (b), this interferometric modulation becomes blurred and vanishes nearly completely. The transversal fiber cross sections for some selected fiber lengths of zero, two, four, six and eight times the beat length are illustrated in Fig. 4.5 (c) and show an increase of symmetry with a simultaneous decrease of peak intensity. The positions of the shown cross sections were chosen to highlight the effect of the coherence loss. At the beginning, the light is clearly concentrated on the left half of the core and starts to smear toward the center and right side with increasing propagation length. Finally, the resulting intensity distribution will be perfect point symmetric and stable during further propagation.

For the experimental exploration of this effect, a cut back measurement at the three mode fiber used in the aforementioned section with an initial length of 53 m was performed. As input, a full coherent modal superposition between the LP_{01} and the LP_{11e} mode was excited using a step like phase plate as described in Sec. 4.2.1. Afterwards the mutual modal degree of coherence of the transmitted light was measured for various fiber lengths. Figure 4.6 depicts the observed behavior of coherence for different fiber lengths. For the mutual modal coherence between the fundamental LP_{01} and the first higher order modes LP_{11e} and LP_{11o}, respectively, a clear drop of coherence for an increasing propagation length is observable in Fig. 4.6 (a) and (b), respectively. Both curves show a similar behavior with a coherence length of $l_{12}^{\mathrm{coh}} = 36.15 \pm 0.55\mathrm{m}$ and $l_{13}^{\mathrm{coh}} = 36.10 \pm .48\mathrm{m}$. Completely different behavior is observable for the degree of coherence between the degenerated LP_{11e} and LP_{11o} modes, depicted in Fig. 4.6 (c). For these modes the mutual modal degree of coherence is nearly constant and shows only a slight decrease for longer fibers lengths. The non-occurrence of a coherence loss is caused by the degeneracy of the two modes. Since both modes have the same propagation constant, consequently, the accumulated optical path length difference is zero. To highlight the distinct similarity between the curves for γ_{12} and γ_{13} all results are plotted together in Fig. 4.6 (d). Since the degenerated LP_{11} modes are always effected by mode coupling between them (see Sec. 3.1.2 pp. 34), the power ratio between the modes was not constant and causes a varying signal-to-noise ratio

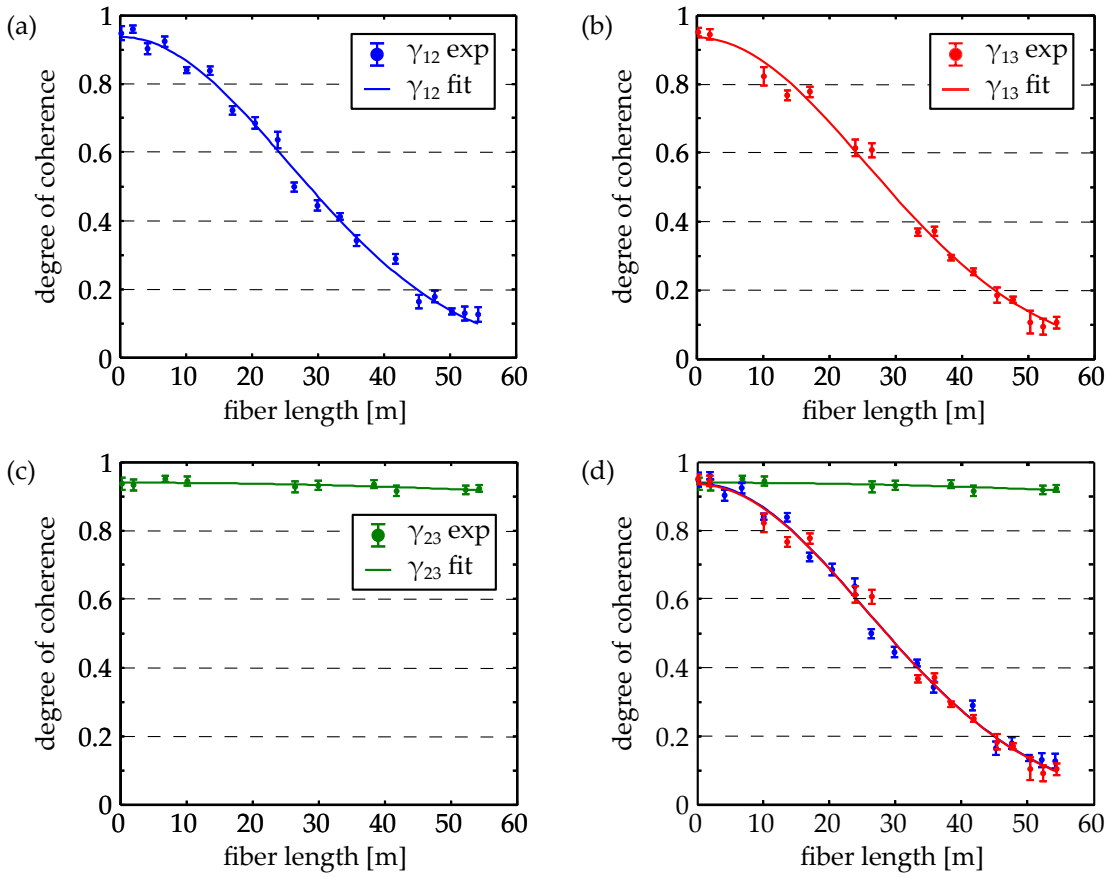

Figure 4.6: The dependency of the mutual degree of coherence on the fiber length between the (a) LP_{01} and LP_{11e}, (b) LP_{01} and LP_{11o} and (c) LP_{11e} and LP_{11o} modes, respectively; (d) shows an overlay of the three curves for a better comparability.

between the measurement positions. In order to achieve a reliable evaluation of the coherence loss, the values for modes with a power ratio below 0.2 were canceled. Thus data points not for all measured fiber lengths can be provided.

4.2.3 Mode Coupling Induced Change of Coherence

One of the fundamental properties of modes is their orthogonality ensuring stable propagation through the fiber. As discussed in Sec. 3.1.2 pp. 34, this orthogonality can be broken by perturbations of the refractive index distribution. Between non-degenerated modes, the coupling is typically weak due to the missing phase matching which is required for an effective modal crosstalk. By introducing a periodic index perturbation, for those periodicities equals to the beat lengths between

two non-degenerated modes, the phase matching condition can be fulfilled and mode coupling becomes possible. Such a periodic perturbation can be realized by mechanical stress induced by long period gratings [119].

This technique for an enforced mode coupling was used to exchange energy between modes of an initially incoherent superposition between the LP_{01} and LP_{11e} modes. For the initial case the resulting intensity is the simple sum of both individual modal intensities

$$I = \left\langle \tilde{c}_{01}\widetilde{LP}_{01} + \hat{c}_{11}\widehat{LP}_{11} \right\rangle = \tilde{\rho}_{01}^2 \left|\widetilde{LP}_{01}\right|^2 + \hat{\rho}_{11}^2 \left|\widehat{LP}_{11}\right|^2, \tag{4.14}$$

where˜and^denote mutual incoherent field components. By the induced coupling for each field component, some amount of energy from one mode is coupled into the other resulting in

$$I = \left\langle \tilde{c}_{01}\widetilde{LP}_{01} + \tilde{c}_{11}\widetilde{LP}_{11} + \hat{c}_{01}\widehat{LP}_{01} + \hat{c}_{11}\widehat{LP}_{11} \right\rangle \tag{4.15}$$

$$= \left|\tilde{c}_{01}\widetilde{LP}_{01} + \tilde{c}_{11}\widetilde{LP}_{11}\right|^2 + \left|\hat{c}_{01}\widehat{LP}_{01} + \hat{c}_{11}\widehat{LP}_{11}\right|^2, \tag{4.16}$$

which represents an incoherent superposition of two individually coherent superpositions between the LP_{01} and LP_{11} modes. Evaluating the interference within each coherent superposition leads to

$$I = \tilde{\rho}_{01}^2|\widetilde{LP}_{01}|^2 + \tilde{\rho}_{11}^2|\widetilde{LP}_{01}|^2 + 2\tilde{\rho}_{01}\tilde{\rho}_{11}|\widetilde{LP}_{11}||\widetilde{LP}_{11}|\cos\Delta\tilde{\phi}_{12} \tag{4.17}$$

$$+ \hat{\rho}_{01}^2|\widehat{LP}_{01}|^2 + \hat{\rho}_{11}^2|\widehat{LP}_{01}|^2 + 2\hat{\rho}_{01}\hat{\rho}_{11}|\widehat{LP}_{11}||\widehat{LP}_{11}|\cos\Delta\hat{\phi}_{12}. \tag{4.18}$$

Assuming now that the modal field functions of the independent field components and the accumulated phase differences are identical, which is justified by the quasi-monochromatic conditions, the interferometric superposition can be summarized to

$$I = \rho_{01}^2|LP_{01}|^2 + \rho_{11}^2|LP_{11}|^2 + 2|LP_{01}||LP_{11}|(\tilde{\rho}_{01}\tilde{\rho}_{11} + \hat{\rho}_{01}\hat{\rho}_{11})\cos\Delta\phi_{12}, \tag{4.19}$$

where $\rho_{01}^2 = (\tilde{\rho}_{01}^2 + \hat{\rho}_{01}^2)$ and $\rho_{11}^2 = (\tilde{\rho}_{11}^2 + \hat{\rho}_{11}^2)$ are the combined excitation strength

of the LP_{01} and LP_{11} mode, respectively. This gives the final interference between the four field components. To determine the effect for the resulting degree of coherence, the visibility of the derived interference law has to be compared with the general two beam case of partial coherence

$$V = \frac{2(\tilde{\rho}_{01}\tilde{\rho}_{11} + \hat{\rho}_{01}\hat{\rho}_{11})}{\rho_{01}^2 + \rho_{11}^2} = \frac{2\rho_{01}\rho_{11}}{\rho_{01}^2 + \rho_{11}^2}|\gamma|. \tag{4.20}$$

Dissolving the above equation for the degree of coherence yields

$$|\gamma| = \frac{(\tilde{\rho}_{01}\tilde{\rho}_{11} + \hat{\rho}_{01}\hat{\rho}_{11})}{\sqrt{\left(\tilde{\rho}_{01}^2 + \hat{\rho}_{01}^2\right)\left(\tilde{\rho}_{11}^2 + \hat{\rho}_{11}^2\right)}}. \tag{4.21}$$

It can be seen that for an incoherent input state without coupling, i.e. $\tilde{\rho}_{11}^2 = \hat{\rho}_{01}^2 = 0$, the output state stays incoherent with $|\gamma| = 0$. The opposite case occurs if no incoherent contributions exist, i.e. $\hat{\rho}_{01}^2 = \hat{\rho}_{11}^2 = 0$, and the coherent input field preserves the also coherence after mode coupling with $|\gamma| = 1$. An interesting situation occurs if the input state contains equal contribution of both incoherent modes and crosstalk of 50%. In that case, the resulting state contains an equal power content for all modes of $\tilde{\rho}_{01}^2 = \tilde{\rho}_{11}^2 = \hat{\rho}_{01}^2 = \hat{\rho}_{11}^2 = 0.25$ and the modal degree of coherence is increased from zero to $|\gamma| = 0.5$. An example of such an increase of coherence by modal coupling is depicted in Fig. 4.7 (c), where the modal degree of coherence of an unperturbed fiber beam without mode coupling is compared with the same input state after enforced crosstalk. It can clearly be seen that the degree of coherence increases from below 0.1 up to about 0.5. The higher modal degree of coherence can also be seen in the beam profiles depicted in Fig. 4.7 (a) and (b), where the highly symmetric intensity distributions of the unperturbed fiber becomes asymmetric after perturbation.

A second effect of the mode coupling is a possible decrease of the modal degree of polarization. This effect occurs when the coupled energy is not only transferred into the LP mode of the initial polarization direction, but also in the degenerated second one. As a result an incoherent vertical field component is added to the

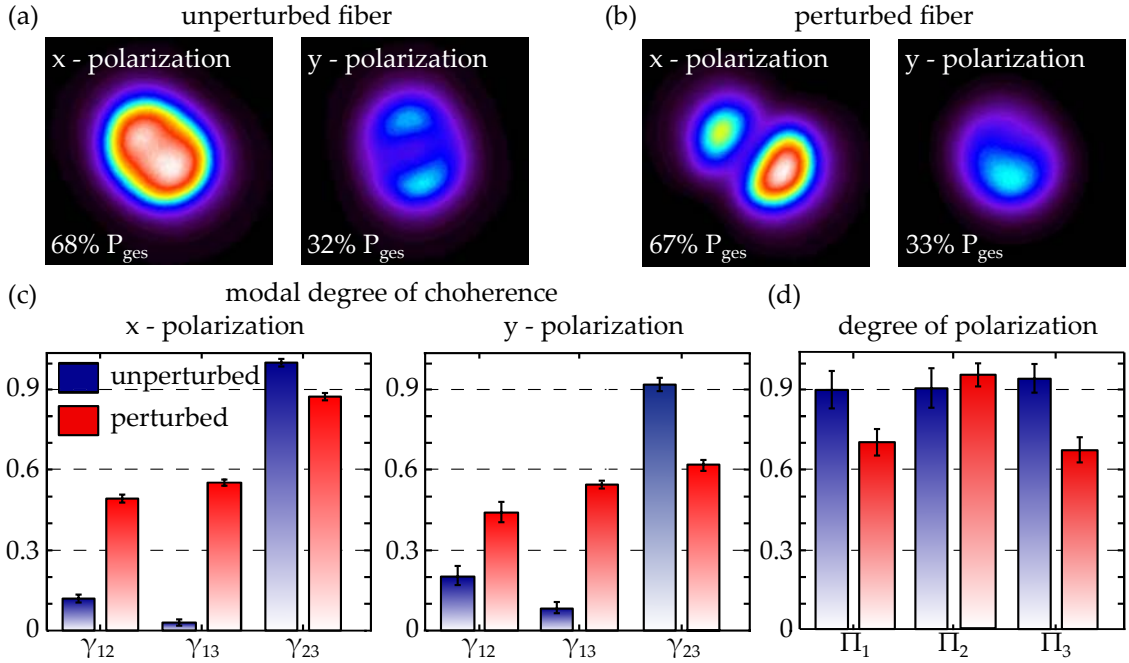

Figure 4.7: Reconstructed intensity distributions for (a) the unperturbed fiber and (b) the perturbed fiber. The mutual degree of coherence is shown in (c) for x polarization and (d) for y polarization; (e) depicts the modal degree of polarization.

original horizontally polarized mode, which results in an unpolarized field contribution. To investigate the effect of the mode coupling on the polarization state, the modal resolved Stokes-measurement introduced in Sec. 2.3.4 pp. 27 was performed. Expressing the resulting Stokes-vector in its spherical representation leads to

$$\mathbf{S}_n = \begin{pmatrix} S_{0,n} \\ S_{1,n} \\ S_{2,n} \\ S_{3,n} \end{pmatrix} = \begin{pmatrix} \rho_{0,n}^2 \\ \rho_{p,n}^2 \cos 2\vartheta_n \cos 2\chi_n \\ \rho_{p,n}^2 \sin 2\vartheta_n \cos 2\chi_n \\ \rho_{p,n}^2 \sin 2\chi_n \end{pmatrix}, \tag{4.22}$$

where $\rho_{0,n}$ are the modal power strengths, $\rho_{p,n}$ the polarized power contributions, and θ_n and χ_n are the shape parameters of the polarization ellipse. Using this notation of the Stokes-vector, the ratio between polarized and total power

contributions, that defines the degree of polarization can be calculated by

$$\Pi_n = \frac{I_{p,n}}{I_{0,n}} = \frac{\sqrt{S_{1,n}^2 + S_{2,n}^2 + S_{3,n}^2}}{S_{0,n}}. \tag{4.23}$$

This procedure allows the determination of the degree of polarization of each LP mode. The results of such measurements with and without coupling of the incoherent modes are depicted in Fig. 4.7 (d). It can be seen that in the case of an unperturbed fiber, the degree of polarization Π_n is about 0.9 indicating nearly perfect polarized modes. After applying the perturbation, which results in the mode coupling between the incoherent field components, the degree of polarization markedly decreases below 0.70 for the first and third guided mode of the fiber.

Chapter Summary

In this chapter the applicability of the correlation filter methods was extended to partially coherent modal superpositions. This was possible by an advancement of the original phase measurement procedure to a four-step phase shifting procedure. It was shown that this new capability is necessary for the reconstruction of partial coherent superposition under quasi-monochromatic conditions. Furthermore, the new capability was applied to investigate the loss of modal coherence during fiber propagation due to modal dispersion. Thus, the determination of the modal coherence length between the fundamental mode and the next higher order mode group to 36 m was possible. Finally, the effect of mode coupling on the modal degree of coherence and on the modal degree of polarization was investigated. It could be shown that the coupling between initially incoherent modes can lead to an increasing modal coherence with a simultaneous decrease of the modal degree of polarization. This effect was demonstrated by the enhancement of the coherence of an initially incoherent superposition up to an degree of coherence of about 0.5. Simultaneously a reduction of the modal degree of polarization to about 0.7 could be observed.

5 Decomposition into Hybride Fiber Modes

Although scalar mode sets are well established and widely utilized in a plethora of applications, they exhibit some limitations for the description of optical fibers due to the underlying weakly guiding approximation. In fact, the fourfold degeneracy of higher order azimuthal LP modes regarding horizontal and vertical polarization, as well as even and odd solutions of the scalar wave equation, are at least partially revoked for the natural hybrid modes of an optical fiber. Hence, while the LP modes can still be formed by well defined vector mode superposition, they are no longer stable during fiber propagation due to the mode beating between the non-degenerated vector modes. Therefore, the scalar LP modes are no longer suitable for the description of the propagation characteristics in strong guiding optical fibers. In addition to the rematching of the mode sets after overcoming the weakly guiding approximation, the vector modes are also used in many kinds of applications and thus a corresponding description of optical beams is also of general interest [80]. Such applications are ranging from high NA focusing [120], high resolution scanning microscopy [121, 122], particle manipulation and acceleration [123, 124], optical communication [125], plasmon surface excitation [126] to material processing [81, 127]. With respect to the aforementioned necessity of describing optical beams in terms of vector modes, in the following chapter the further development of the correlation filter method for this new field of application will be introduced. To do this a special type of strongly guiding fiber and the occurring modes will be discussed. Afterwards the required modification of the correlation filter procedure for the vectorial mode detection will be outlined by incorporating non-uniform anisotropic wave plates. Finally, the capability of the

new vectorial decomposition scheme will be demonstrated by the determination of the fiber transmission matrix of a strong guiding fiber.

5.1 Vector Modes of a Vortex Fiber

A newly developed fiber concept, which leaves the weakly guiding approximation, is the so called "vortex fiber" proposed by Bozinovic et al. for mode coupling free MDM in optical telecommunication systems [19]. Here the strong guidance regime was chosen to lift the near degeneracy between modes within one mode group and consequently avoid the disturbing modal crosstalk. It was shown that 1.6 Tb/s data transmission over 1.1 km at about 1550 nm is possible without the need of an additional digital signal processing for crosstalk compensation. The measured refractive index (RI) profile of such an "vortex fiber" is depicted in Fig. 5.1 (a). The measurement was done at the Fraunhofer Institute for Applied Optics and Precision Engineering with an "IFA-100 Fiber Index Profiler". In contrast to conventional step index fibers the "vortex fiber" exhibits a characteristic RI profile, consisting of a central core and an additional high-index ring structure. For a better visualization of this RI structure a two dimensional RI distribution was modeled out of the measured profile data and is shown in Fig. 5.1 (b). Whereas the break of the debilitating near-degeneracy between the modes is caused by the high-index ring, the central core serves to provide a high Gaussian-shaped fundamental mode enabling low-loss coupling. It was shown that this fiber concept enables mode purities as high as $\sim$ 30 dB at the design wavelength of 1550 nm between the vector modes of the LP_{11} mode group [66].

Besides MDM in the field of optical fiber communication, the stable propagation of vector modes can also be beneficial for other optical applications. Due to the strong z-component of the TM_{01} mode it can be used to detect the longitudinal field component in a scanning near-field optical microscope (SNOM) [122]. The fiber is conically tapered and gold coated, which realizes a "plasmonic tip". At this tip a longitudinal optical field excites a longitudinally polarized surface plasmon

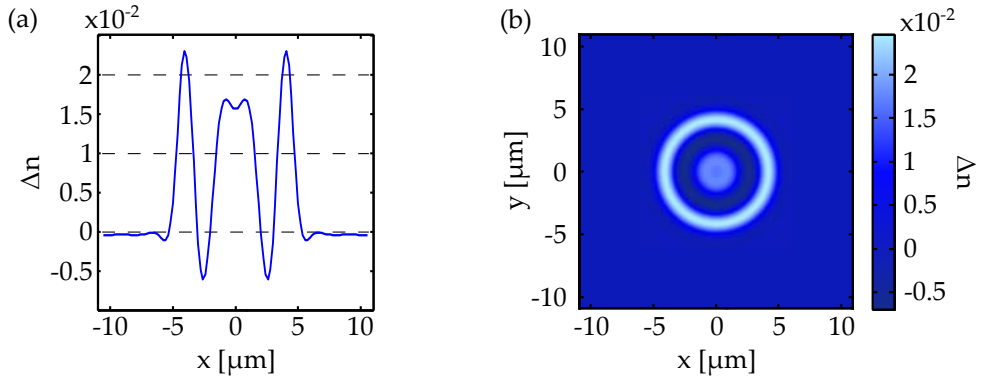

Figure 5.1: Refractive index profile of the vortex fiber; (a) measured refractive index profile, (b) modeled refractive index distribution

polariton (SPP) which is transformed by propagation along the tapered fiber into a radially polarized SPP, and couples finally into the TM_{01} fiber mode. The conical taper ensures that the phase matching condition for efficient coupling will be fulfilled at a defined fiber radius [122]. Also, the reverse process of exciting longitudinal optical fields is possible by propagating a pure TM_{01} mode within the fiber to the "plasmonic tip" [122]. To ensure a high efficiency of this fiber based SNOM application, the required radially polarized TM_{01} mode should have as low as possible crosstalk to other modes. By this reason, the concept of the "vortex fiber" seems to be very promising and has already proven its potential.

A direct transfer of the determined propagation properties, from the studies done at the design wavelength of 1550 nm, to the SNOM applications with an operating wavelength of 784 nm is not possible. This is due to notable changes of the number and shape of the guided modes associated with the wavelength shift, and a corresponding reduction of the effective refractive index (ERI) spacing. By this reason a new characterization of the propagation properties at 784 nm is necessary to evaluate the applicability of the vortex fiber for plasmonic SNOM measurement methods. In order to characterize the capability of the vortex fiber, at first the theoretical properties of the guided modes like ERI and the modal field distribution are derived from the measured RI profile by numerical investigations. The modeled RI distribution from Fig. 5.1 (b) was used to determine the mode fields and eigenvalues by solving the coupled mode equation given by Eq. (2.3)

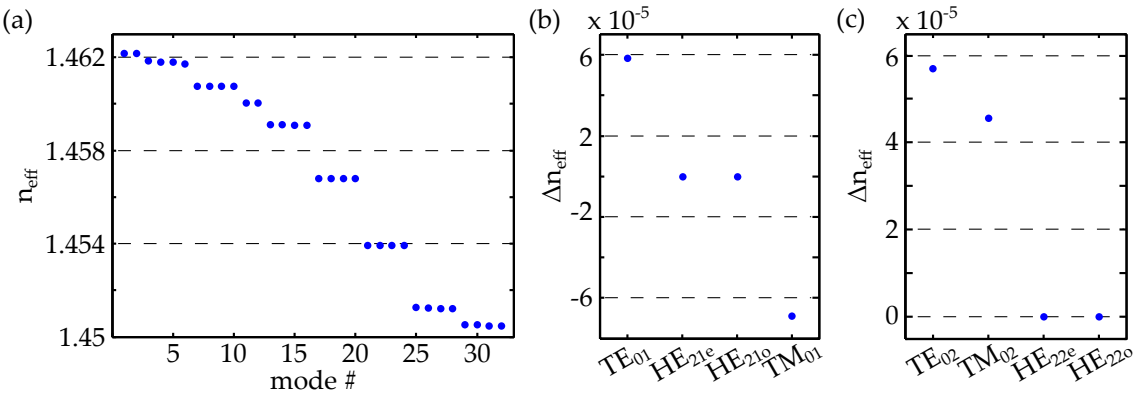

Figure 5.2: Effective refractive index spectrum of the vortex fiber at 786 nm (a) for all guided modes; the effective refractive index difference within the (b) TM_{01} and (c) TM_{02} mode group.

p.10, with a full vectorial finite element mode solver such as the one provided by Comsol Multiphysics®. The resulting ERI spectrum is depicted in Fig. 5.2 (a) and shows the appearance of 32 guided modes in contrast to only six at 1550 nm [19]. Interestingly, two mode groups containing a mode with the wanted radial polarization distribution occur, namely the TM_{01} mode and the higher radial order TM_{02} mode. For the illustration of the degeneracy lift within the corresponding mode groups, the ERI difference with respect to the hybrid modes HE_{21} and HE_{22} is plotted in Fig. 5.2 (b) and (c), respectively. In comparison, the ERI difference of 1.6×10^{-4} given in literature [128] for 1550 nm is reduced to only about 0.6×10^{-4} and 1.5×10^{-5} for the TM_{01} and the TM_{02} mode, respectively. From investigations of polarization maintaining fibers and higher order mode coupling in LMA fibers a ERI difference of 10^{-4} was identified as a reasonable proxy for mode stability [89, 128]. This condition is well fulfilled at the design wavelength but is now violated especially for the TM_{02} mode. Nevertheless, for the task of stable radially polarized mode propagation, the TM_{01} mode might be sufficiently separated since it is still close to the coupling limit, and only short fiber lengths of about one meter are of interest.

The intensity distributions together with the polarization distribution for a selection of the guided modes are depicted in Fig. 5.3, where the boundaries of the core and ring structure are highlighted by dashed circles. The spatially resolved

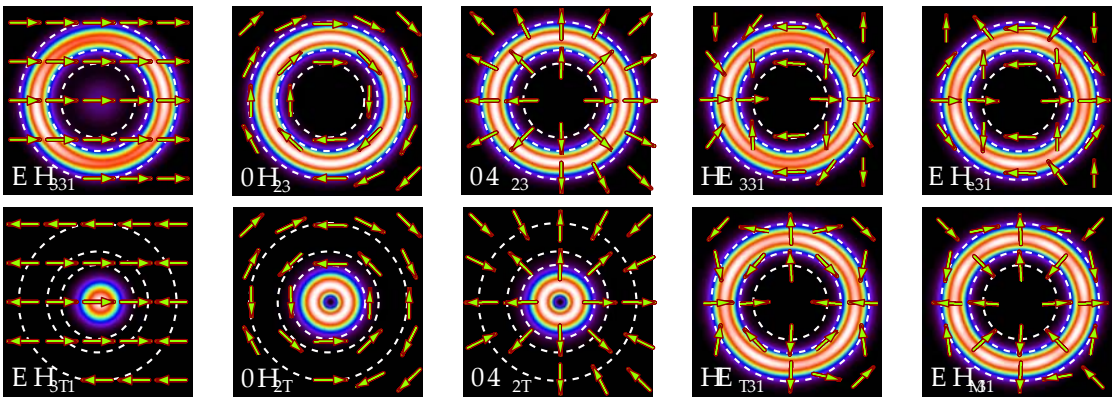

Figure 5.3: Intensity and polarization distribution of some selected vortex fiber modes, the dashed circles indicates the boundaries of the core and ring structure, respectively.

polarization state is indicated by the green arrows. It can clearly be seen that the modes of the lowest radial order are well confined in the outer ring structure. Only the fundamental mode has some small amount of energy guided in the core, but the original design goal of a Gaussian like intensity distribution for low-loss mode coupling is no longer achieved for applications at 784 nm. In contrast, the guided modes of higher radial order are nearly completely confined in the inner core structure and the occurring HE_{12} modes show the typical Gaussian like intensity distribution of a fundamental step index fiber mode. An interesting feature of the calculated mode set are the nearly indistinguishable intensity distributions of the higher order azimuthal modes guided within the ring. The appearance of modes, which are either guided in the ring or the core, indicates a decoupling of these two basic elements of the RI distribution. Hence, only the modes guided within the ring structure can extract an advantage from the new fiber design, whereas for the modes guided in the core, a step-index fiber mode like behavior is expected.

5.2 Creation and Detection of Vector Modes

For the characterization of strong guiding fibers, the real hybrid modes with their spatially varying polarization distributions have to be taken in account. However, the pure holographic correlation filter method described in Sec. 2.3 pp. 19, even

with the Stokes vector extension introduced in Sec. 2.3.4 pp. 27, yields only an indirect access to vector modes. For that the complete vectorial field has to be reconstructed and subsequently decomposed in the vector mode set. The following section points out a way to overcome this indirect description by the usage of non-uniform anisotropic wave plates, so called q-plates, which enables in combination with the holographic CF a direct decomposition into the real hybrid fiber modes. The working principle of q-plates in general is described and their implementation for beam shaping and modal decomposition procedures is discussed.

5.2.1 Vectorial Manipulation with Q-Plates

In classical optics the polarization state of a scalar beam is manipulated with an anisotropic wave plate, which introduces a phase difference between the polarization components aligned with the fast and slow axes of the typically used birefringent crystal. Since in the ideal case such crystals have a uniform birefringence, they can not be used directly for the spatially varying manipulation of the polarization distribution. A variety of approaches were proposed to overcome this limitation including segmented classical wave plates, digitally controlled liquid crystal devices or sub-wavelength gratings, to name only a few.

The usage of space-variant dielectric sub-wavelength gratings for the manipulation of the spatial polarization distribution was proposed by Bomzon et al. [129] for the generation of radially and azimuthally polarized beams. Further investigations of the mode transformation properties of such non-uniform anisotropic elements were done by the investigation of the optical spin-to-orbital angular momentum conversion [130].

For the transformation of a linear polarized beam into a vector beam with spatially varying but locally linearly polarization distribution, a spatially varying lambda half-wave plate with a local fast axis orientation α of

$$\alpha(r, \theta) = q\theta + \alpha_0 \tag{5.1}$$

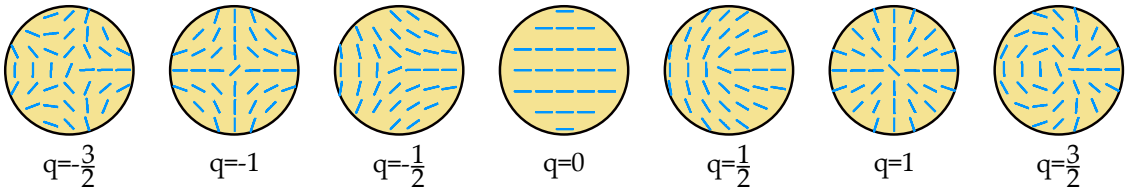

Figure 5.4: Example for the local orientation of the optical axis for q-plates with charge $q \in \left[-\frac{3}{2}, \frac{3}{2}\right]$, the offset angle $\alpha_0 = 0$.

is required, where θ is the azimuthal angle and q and α_0 are constants. Considering the π periodicity for the optical axis orientation of a half-wave plate, q has integer or semi-integer values to preserve the rotation symmetry of the system. Here, the charge q defines the azimuthal order of the resulting beam, whereas the angle α_0 defines the azimuthal orientation of the entire structure. In literature, these type of elements are called q-plates [130] with respect to the characterizing charge parameter q. In order to describe the effect of such a q-plate on a beam its Jones matrix can be calculated by pointwise rotation of a half-wave plate

$$M_q(\alpha_0) = \mathbf{R}(-\alpha)\begin{pmatrix} 1 & 0 \\ 0 & -1 \end{pmatrix}\mathbf{R}(\alpha) \tag{5.2}$$

$$= \begin{pmatrix} \cos\left[2(q\theta + \alpha_0)\right] & \sin\left[2(q\theta + \alpha_0)\right] \\ \sin\left[2(q\theta + \alpha_0)\right] & -\cos\left[2(q\theta + \alpha_0)\right] \end{pmatrix}, \tag{5.3}$$

with $\mathbf{R}(\alpha)$ the standard 2×2 rotation matrix by an angle α. Figure 5.4 depicts a selection of q-plates for $q \in [-\frac{3}{2}, \frac{3}{2}]$, where the blue strokes indicate the orientation of the local optical axis. The offset angle α_0 was set to zero. For $q = 0$, no spatial variation occurs and the element represents a classical half-wave plate with a Jones-matrix given by

$$M_{\frac{\lambda}{2}}(\alpha_0) = \begin{pmatrix} \cos(2\alpha_0) & \sin(2\alpha_0) \\ \sin(2\alpha_0) & -\cos(2\alpha_0) \end{pmatrix}, \tag{5.4}$$

with α_0 the orientation angle of the optical axis.

The effect of a q-plate on a uniformly polarized input beam can be understood

by applying the Jones calculus, where an arbitrary beam is expressed by its Jones vector

$$\mathbf{E}(\mathbf{r}) = A(\mathbf{r}) \begin{pmatrix} c_x \\ c_y \end{pmatrix}. \tag{5.5}$$

Here, $A(\mathbf{r})$ denotes a normalized complex field function, and c_x and c_y define the horizontal and vertical field strength, respectively. The transmitted field after the q-plates follows by matrix multiplication to

$$\mathbf{E}_{out}(\mathbf{r}) = M_q(\alpha_0)\mathbf{E}_{in}(\mathbf{r}) = A(\mathbf{r}) \begin{pmatrix} c_x \cos\left[2(q\theta + \alpha_0)\right] + c_y \sin\left[2(q\theta + \alpha_0)\right] \\ c_x \sin\left[2(q\theta + \alpha_0)\right] - c_y \cos\left[2(q\theta + \alpha_0)\right] \end{pmatrix} \tag{5.6}$$

and shows a polarization distribution, which is in general dependent on the azimuth angle θ. For suitable combinations of the input polarization state defined by c_x and c_y, and q-plate parameters q and α_0, the generation of well known polarization distributions becomes possible, e.g. of cylindrical vector beams. For example, a horizontally polarized input beam with $c_x = 1$ and $c_y = 0$ and a q-plate with a charge $q = 0.5$ and an orientation angle $\alpha_0 = 0$ results in an output beam of

$$\mathbf{E}_{out}(\mathbf{r}) = A(\mathbf{r}) \begin{pmatrix} \cos\theta & \sin\theta \\ \sin\theta & -\cos\theta \end{pmatrix} \begin{pmatrix} 1 \\ 0 \end{pmatrix} = A(\mathbf{r}) \begin{pmatrix} \cos(\theta) \\ \sin(\theta) \end{pmatrix}, \tag{5.7}$$

which is the well known radially polarized beam. With the same q-plate configuration but an input beam polarized in the vertical direction, $c_x = 0$ and $c_y = 1$, a azimuthal polarized beam can be generated. In addition to the control of the local polarization distribution the azimuthal phase structure associated with the orbital angular momentum (OAM) can be manipulated. For that, circularly polarized input states are required. For example, a left-circularly polarized input beam

with $c_x = 1$ and $c_y = i$ results in an output beam of

$$\mathbf{E}_{out}(\mathbf{r}) = A(\mathbf{r}) \begin{pmatrix} \cos\left[2q\theta\right] + i \sin\left[2q\theta\right] \\ \sin\left[2q\theta\right] - i \cos\left[2q\theta\right] \end{pmatrix} = A(\mathbf{r}) e^{i2q\theta} \begin{pmatrix} 1 \\ -i \end{pmatrix}, \tag{5.8}$$

which is now right-circular polarized, and shows the occurrence of an additional azimuthal angle dependent phase term of $e^{i2q\theta}$. This spiraling phase term represents an optical vortex of charge $2q$ and changes accordingly the carried OAM value of the transmitted beam. Hence, q-plates allow the conversion of spin-to-orbital angular momentum. Also the first case can be understood in this frame by dividing the linearly polarized input beam into an equal superposition of a left and a right handed circularly polarized beam which transfers to a left and right circularly polarized beam with opposite signed phase vortex orientations afterwards

$$\mathbf{E}_{out}(\mathbf{r}) = \frac{A(\mathbf{r})}{\sqrt{2}} \left[e^{i\theta} \begin{pmatrix} 1 \\ -i \end{pmatrix} + e^{-i\theta} \begin{pmatrix} 1 \\ i \end{pmatrix} \right] = A(\mathbf{r}) \begin{pmatrix} \cos(\theta) \\ \sin(\theta) \end{pmatrix}. \tag{5.9}$$

This ability to manipulate the spatial phase and polarization distributions makes q-plates a powerful tool for the shaping of complex light distributions in a plethora of applications including microscopy [131], optical communication [125], and quantum optics [132], to note only a few.

The q-plates used in this thesis were realized by femto-second laser pulse written nano gratings, which allow a quasi-continuous variation of the local optical axis. An example raster electron microscopic image of such a nano-grating structure is depicted in Fig. 5.5 (a) for a q-plate with charge $q = 1$ and $\alpha_0 = \frac{\pi}{4}$ given by a spiraling orientation of the local optical axis. The designed orientation of the optical axis for the depicted structure is shown in Fig. 5.5 (b) and enables the transformation of a circularly polarized beam into a radially polarized one. The depicted grating was written by an 800 fs pulse laser at 1550 nm with a pulse energy of about 1 μJ. The shown q-plate as well as the used one were fabricated at the Institute of Applied Physics.

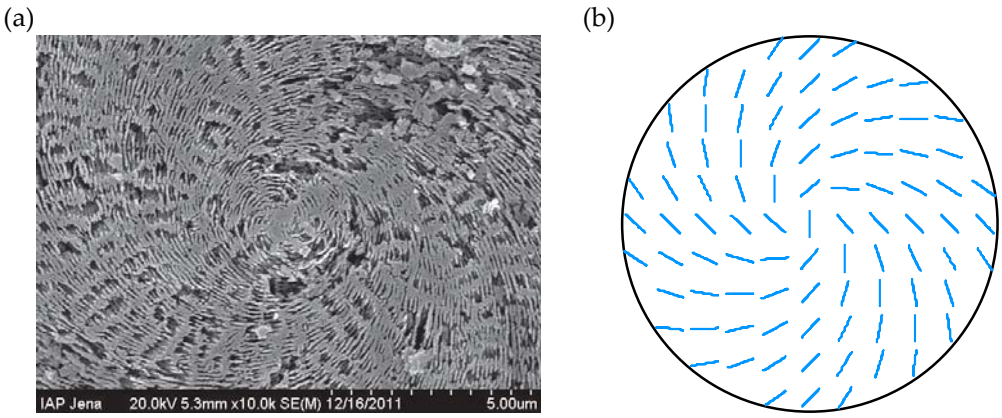

Figure 5.5: Example of a written nano grating structure for a q-plate with charge $q = 1$ and $\alpha_0 = \frac{\pi}{4}$ for the transformation of a circularly polarized beam into a radially polarized beam; (a) raster electron microscope image and (b) draft of the indented grating orientation.

The manufacturable q-value range of the fabricated q-plates was limited to positive values only due to mechanical limitations of the femto-second laser writing stage. In order to apply also negative valued q-plates, a combination of the q-plate with positive charge and a half-wave plate was used. Aligning both elements with orientation $\alpha_0 = 0$ leads by matrix multiplication of Eq. (5.3) and Eq. (5.4) to a combined Jones-matrix of

$$M_{-q} = M_{\frac{\lambda}{2}} M_q = \begin{pmatrix} 1 & 0 \\ 0 & -1 \end{pmatrix} \begin{pmatrix} \cos(2q\theta) & \sin(2q\theta) \\ \sin(2q\theta) & -\cos(2q\theta) \end{pmatrix} \tag{5.10}$$

$$= \begin{pmatrix} \cos(-2q\theta) & \sin(-2q\theta) \\ \sin(-2q\theta) & -\cos(-2q\theta) \end{pmatrix}, \tag{5.11}$$

which represents a q-plate with an opposite signed charge. This procedure reduces the demand on specially fabricated elements and was applied in this thesis to emulate negative valued q-plates for the vectorial manipulation.

5.2.2 Vectorial Beam Shaping

The generation of the vectorial mode functions is one of the key components for the investigation of the fiber's modal transmission properties. In contrast to the

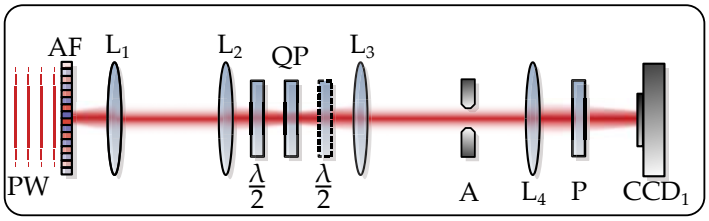

Figure 5.6: Setup for the generation of vector modes; PW, plane wave; AF, amplitude filter; L_{1-4} lenses, $\frac{\lambda}{2}$, half wave plate; QP, q-plate; A, aperture; P, polarizer; CCD, camera.

beam shaping strategies introduced in Sec. 2.2 pp. 16, which enable the creation of arbitrary amplitude and phase distributions, an additionally realization of the characteristic modal polarization distribution is necessary. This task can be tackled by incorporating the above introduced q-plates into the mode forming process. For fibers supporting only a few low order modes and showing a Gaussian like fundamental mode, the selective vector mode excitation is typically performed by a q-plate only with a Gaussian input beam illumination [66, 125]. This excitation procedure is not applicable for the investigation of the vortex fiber at 784 nm due to the occurrence of higher order radial modes and strong deviations from typically Gaussian-like mode profiles, as discussed in Sec. 5.1.

In order to ensure the excitation of pure fiber modes a combination of amplitude as well as polarization distribution field shaping is required, especially for addressing selectively modes of the same azimuthal but different radial mode order. Therefore, the modes are shaped by using a combination of an amplitude filter and a q-plate as depicted in Fig.5.6. At first the amplitude filter under plane wave illumination attenuated the transmitted light according to the needed radial mode profile. In a second step the azimuthal field dependence, represented by the polarization distribution, is achieved after transmission through a q-plate with an appropriate charge. The input polarization state was switchable by a half-wave plate in front of the q-plate. An optionally insertable second half-wave plate after the q-plate could be used to invert the effective sign of the q-plate. Both shaping steps were combined by a 1:1 telescopic setup in $4f$ configuration ($f_{L_1} = f_{L_1} = 180$ mm). Afterwards, the shaped field was imaged onto a camera behind a rotatable

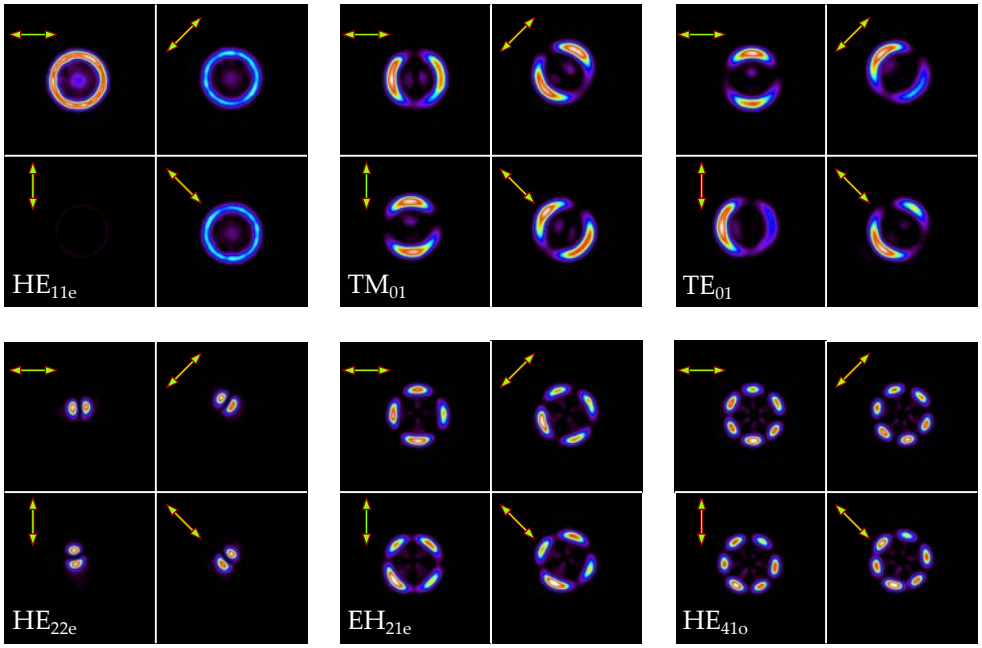

Figure 5.7: Example of generated vector beams by the vectorial shaping technique combining amplitude filter and q-plate. The arrow indicates the orientation of the polarizer at 0°. 45°, 90° and 135°, respectively.

polarizer by a second telescopic setup in $4f$ configuration ($f_{L_3} = 375$ mm, $f_{L_3} = 180$ mm) to evaluate the quality of the created vector beams. In the Fourier plane of the second telescope, an aperture was inserted to block stray light from the shaped beam.

Figure 5.7 depicts a selection of vectorially shaped modes, analyzed with a polarizer at various azimuthal orientations, i.e. at 0°, 45°, 90° and 135°, respectively, to prove the vector character of the light field. For the fundamental mode HE_{11e} shaped by the amplitude filter, only the typical scalar behavior can be observed, i.e. the shape of the intensity distribution is invariant for different polarizer orientations and only the amount of transmitted light varies. The maximum transmission at 0° and minimum transmission at 90° identify this mode as x-polarized. Otherwise, for higher order modes, by incorporating the q-plates for beam shaping, the changing intensity pattern for different polarizer orientations illustrates the spatially varying polarization distribution. It can be seen that the TM_{01} mode shows always a two-lobe structure parallel to the polarizer orientation indicating the radial polarization of this mode. In the same way, the azimuthal

polarization distribution can be revealed for the TE_{01} mode where the two-lobe intensity structure is always orthogonal to the polarizer orientation. An example of a hybrid mode is given by the HE_{22e} mode, where the two-lobe structure rotates against the direction of polarizer rotation. In this case a q-plate with charge $q = \frac{1}{2}$ was applied, where an additional half-wave plate was used for the HE_{22e}. Modes of azimuthal order two and three, like the depicted EH_{21e} and HE_{41o} modes, are characterized by their four- and six-lobe structured transmitted intensity distribution, respectively. It has to be noted that due to manufacturing imperfection, the applied q-plates have some non-uniform transmission characteristics which results in a non perfect rotation symmetric intensity distribution, especially for the TE_{01} mode observable as the occurring asymmetry between the lobes. However, since the basic modal characteristics (i.e. the azimuthal polarization distribution and the radial mode profile) are realized, the shaped field can still be used for fiber mode excitation.

5.2.3 Vectorial Correlation Analysis

In addition to the creation of vector modes with non-uniform polarization distribution, q-plates can be also used to decompose general vector beams emerging from optical fibers in terms of hybrid modes. Similar to the scalar CFM, the inner product relation between the investigated beam $\mathbf{U}(\mathbf{r})$ and the vectorial mode functions $\psi(\mathbf{r})$ has to be performed optically and evaluated. As mentioned in Sec. 2.3.4 pp. 27 with the holographic CF, it is not possible to encode the polarization information of the optical fields into the chromium holograms. However, the aforementioned q-plates hold this lacking capability and therefore in combination with the holographic techniques enable the realization of the needed transverse vectorial field distributions for the transmission function. In order to encode the modal field distribution into the vectorial CF, the mode function is separated into an azimuthally and a radially dependent part, $\Phi(\phi)$ and $R(r)$, respectively. Such a separation is always possible for cylindrical symmetric problems, like the currently investigated vortex fiber.

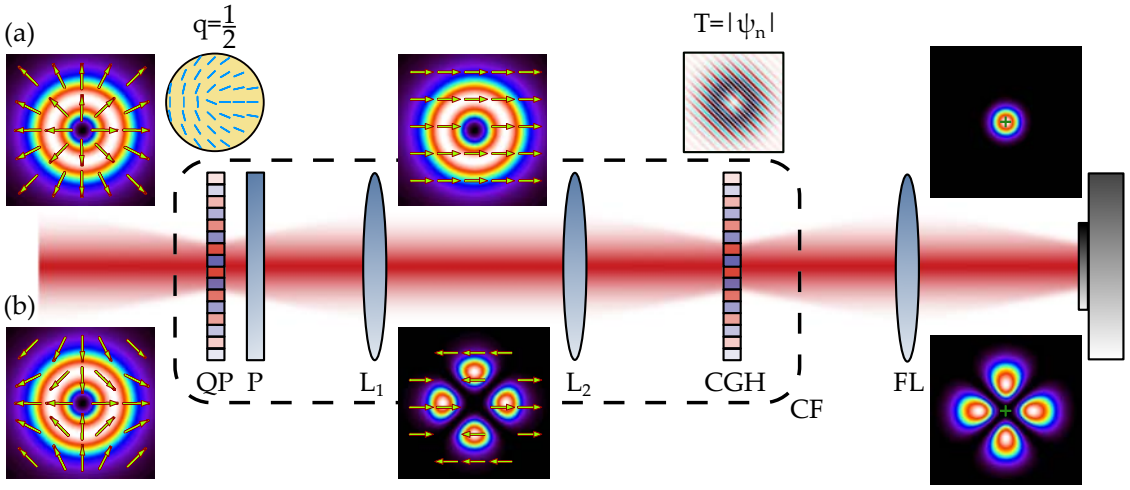

Figure 5.8: Principle working scheme of the vector mode correlation filter consistent of two parts, the q-plate (QP) for the azimuthal and the computer generated hologram (CGH) for the radial correlation. (a) intensity patterns of an illuminating TE_{01} mode and (b) for the HE_{21e} mode

A principle working scheme of the vectorial CF is depicted in Fig 5.8, where the splitting of the transmission function into an azimuthal and a radial dependent part realized by a q-plate in combination with a polarizer and the computer generated hologram (CGH) is shown. Both parts are combined by a 1:1 telescopic setup in $4f$ configuration and together with a Fourier lens in $2f$ configuration enable the all-optical performance and detection of the inner product relation. Figure 5.8 (a) shows the TM_{01} mode as the illuminating beam and an accordingly matched transmission function of the q-plate – polarizer combination, which results in a homogeneously polarized beam without any further azimuthal dependence. After additional correlation with the radial field distribution provided by the CGH, a bright spot on the optical axis indicates the successful detection of the mode. Figure 5.8 (b) shows a negative example for a non matching illuminating mode. There, the field distribution after passing the q-plate and the polarizer still shows an azimuthal dependence resulting into a non detectable intensity in the detection plane after the CGH. Similar to the scalar modal decomposition scheme discussed in Sec. 2.3 pp. 19, the completeness of the mode set enables the determination of the relative modal power strengths by measuring the correlation signals of all possible guided modes and subsequent normalization of the obtained power

spectrum.

It has to be noted that with this type of correlation filter, no phase measurement between the measured modes and an arbitrary reference mode is possible as with the scalar decomposition scheme. But for most applications like the evaluation of the transmission purity, the determinable modal power spectrum already contains all needed information. In addition, due to the lack of phase information complete optical field reconstruction was not possible. However, in cases directed on the reconstructed field distribution, the projection of the vector modes onto its LP mode counter parts and a subsequent modal resolved Stokes-parameter measurement is still possible, as discussed in Sec. 2.1.2 pp. 12 and Sec. 2.3.4 pp. 27.

5.3 Vector Mode Transmission Matrix

In this section the multiple-input-multiple-output (MIMO) measurement procedure introduced in Sec.3.1.2 pp. 34 will be applied on the vortex fiber. Due to the removal of the eigenvalue degeneracy between modes of the same azimuthal order, the LP mode approximation is no longer valid for the description of the modal propagation effects. Hence, the adapted measurement procedure introduced in Sec. 5.2 for the excitation and decomposition of the hybrid fiber modes will used. Afterwards the achieved results will be discussed with respect to the transmitted mode purity and compared with qualitative polarization measurements.

5.3.1 Measurement Procedure

For the characterization of the propagation properties of the vortex fiber by MIMO measurements, the vector mode excitation and decomposition strategies introduced in Sec. 5.2.2 and Sec. 5.2.3, respectively, will be applied. The setup containing the three steps; selective excitation, transmission, and modal decomposition is depicted in Fig. 5.9. In the first step [Fig. 5.9(a)], the input mode profile is generated by illuminating a plane wave onto an amplitude filter, which transmits only the desired amplitude distribution by spatial variant attenuation. Afterwards,

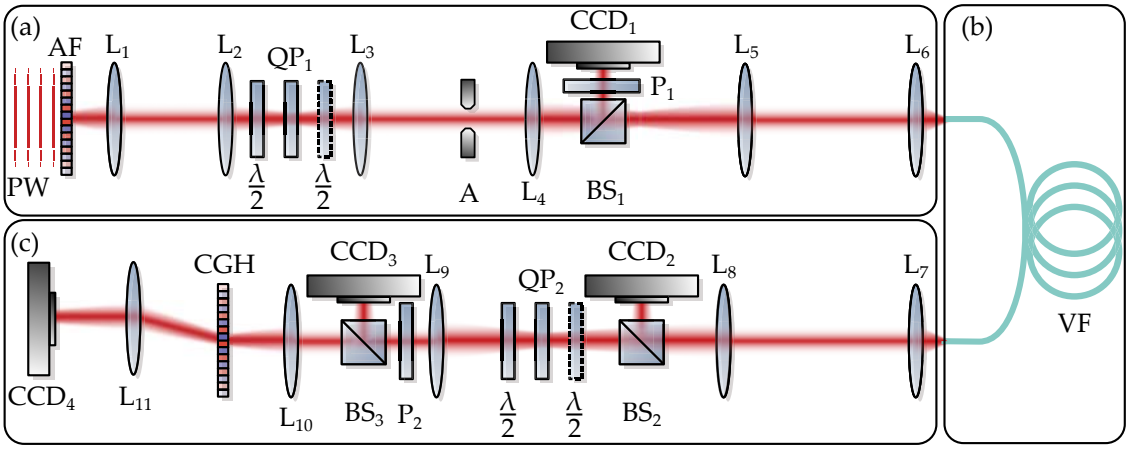

Figure 5.9: Setup for the determination of the vector mode transmission matrix with (a) the beam shaping, (b) the fiber transmission and (c) the vector mode decomposition. PW, plane wave; AF, amplitude filter; L_{1-11} lenses; $\frac{\lambda}{2}$, half-wave plate; $QP_{1,2}$, q-plate; A, aperture; BS_{1-3}, beam splitter; $P_{1,2}$, polarizer; CCD_{1-4}, camera; VF, vortex fiber; CGH, computer generated hologram.

the shaped amplitude profile is imaged by a telescopic setup in $4f$ configuration (f_{L_1}=180 mm and f_{L_2}=180 mm) onto a q-plate QP_1, which performs the shaping of the azimuthal polarization distribution. For addressing all four modes of each mode group, two additional half-wave plates are placed before and behind the q-plate to change the illuminating polarization direction and the sign of the effectively applied q-value, respectively. The shaped field is then de-magnified by two cascaded $4f$ telescopes (f_{L_3}=375 mm, f_{L_4}=180 mm, f_{L_5}=400 mm and f_{L_6}=4 mm) to match the scale of the vortex fiber. In the Fourier-plane of the first telescope, an aperture was placed to remove disturbing stray light from the beam shaping elements. Separated by the beam splitter, the quality of the shaped field could be monitored in the intermediate image plane between the two telescopes behind a rotatable polarizer with the camera CCD_1. The resulting shaped and de-magnified mode fields are coupled into the vortex fiber under test and transmitted through a 1.2 m long fiber piece. Afterwards, the beam was out-coupled and 150 times magnified and imaged simultaneously onto the correlation filter setup and CCD_2 separated by a beam splitter. To achieve this magnification the lenses L_7 and L_8 in a telescopic $4f$ configuration were used (f_{L_7}=4 mm and f_{L_8}=600

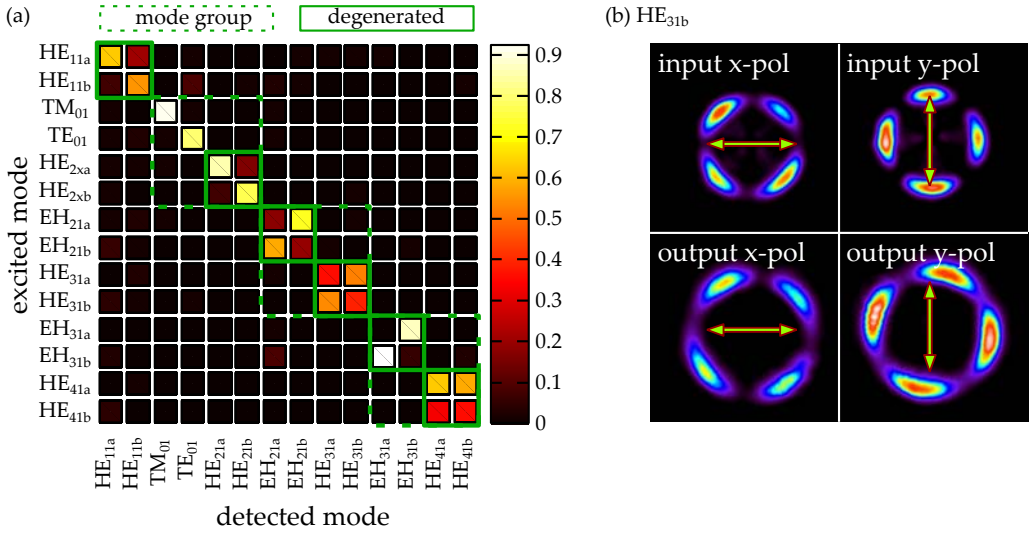

Figure 5.10: Transmission matrix of the vortex fiber (a) for modes guided in the ring structure i.e. radial order one, (b) example of mode rotation due to mode coupling between degenerated modes.

mm). The correlation filter setup consisted of the q-plate QP_2 together with two half-wave plates, a polarizer and a Lee-coded amplitude hologram CGH representing the azimuthal and radial parts of the transmission function. Both building blocks were connected by a 1:1 telescopic setup in $4f$ configuration (f_{L_9}=180 mm and $f_{L_{10}}$=180 mm). After optical Fourier-transformation of the transmitted light with lens L_{11} in $2f$ configuration, the correlation signal could be detected with the camera CCD_4. This combination of vectorial beam shaping for selective fiber mode excitation and complete vector modal decomposition allowed the determination of the fiber transmission matrix and thus the evaluation of the purity of the excited and propagated vector modes.

5.3.2 Determination of Modal Transmission Purity

At first the transmission properties for the azimuthal modes of radial order one, which are guided in the ring structure of the fiber, were determined to characterize the general crosstalk behavior of the vortex fiber concept at a wavelength of 784 nm. The response of each shaped and injected vector mode was recorded by the previously introduced vectorial modal decomposition scheme. The result-

ing transmission matrix is depicted in Fig. 5.10 (a), where each mode group or degenerated mode pair is highlighted by a green dashed or solid box, respectively. It can be seen that the transmission behavior is represented by a nearly pure diagonal matrix with respect to the degenerated mode pairs. This confirms the successful removal of the near degeneracy within the mode groups of the ring type fiber concept also at the 784 nm wavelength. However, between the degenerated mode pairs themselves crosstalk still occurs due to fiber imperfections and external perturbations, which can not be avoided even by this special fiber design. Due to the degeneracy of the coupling modes, nearly no additional phase differences between them will occur. This results in a preservation of the locally linear polarization distribution which is only rotated with respect to the initial coordinate system. This can be seen in Fig. 5.10 (b) for the example of the HE_{31b} mode, where the input and output beam is imaged behind a polarizer in x and y orientation, respectively. For the input modes, the polarizer orientation is parallel to the connection between opposing minima or maxima of the lobe like intensity distributions. In contrast to this, the maxima and minima of the output intensity distributions are rotated by about 10° with respect to the polarizer orientation, indicating mode coupling. However, the preservation of the lobe like structure reveals the local near linear polarization distribution of the transmitted beam.

After examining the nearly crosstalk free transmission of the modes guided in the ring structure, additionally the transmission purities of the modes of the second radial order were investigated, which are guided in the central core of the fiber structure. The achieved results are shown in Fig. 5.11, where the transmission matrix for the two mode groups containing the two radially polarized modes TM_{01} and TM_{02} is shown. The mode groups and degenerated mode pairs are highlighted by green dashed and solid boxes, respectively. It can be seen again that the mode group guided in the ring structure, which contains the TM_{01} mode, shows nearly no crosstalk. This demonstrates the ability to transmit the radially polarized mode TM_{01} nearly without perturbations and with an output mode purity of about 94 %. In contrast, the next higher order radial mode group which

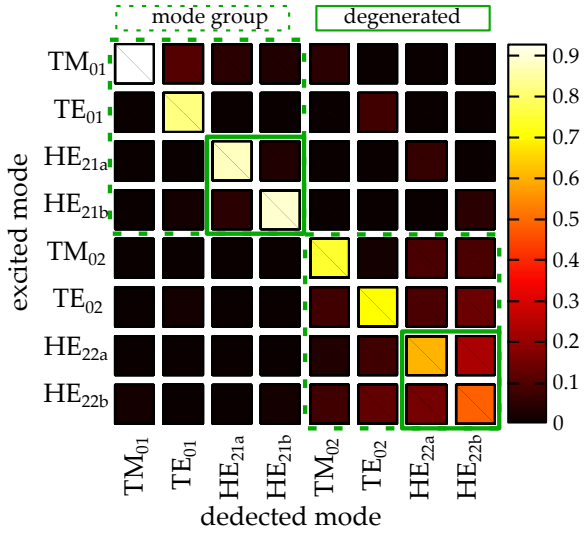

Figure 5.11: Transmission matrix of the vortex fiber for the two mode groups of azimuthal order one containing the radially polarized modes.

contains the TM_{02} mode shows a considerable amount of crosstalk within the group. Thus the output purity of the TM_{02} mode is only about 74 %, resulting in a strong perturbation of the intended radial polarization distribution. This emphasizes the benefit of the ring structure in comparison to standard single core fiber structures for the transmission of pure hybrid vector modes since the TM_{01} guided in the high index ring is transmitted nearly crosstalk free, whereas the TM_{02} mode guided in the inner core is strongly perturbed.

For a more intuitive and qualitative picture of the occurring perturbations the output beams for TM_{01} and TM_{02} illumination were additionally decomposed into a corresponding set of LP modes. Using this new mode set and performing a modal resolved Stokes measurement, as introduced in Sec. 2.3.4 pp. 27, enables the reconstruction of the spatial polarization distribution of the transmitted beam. The appropriate LP mode set was built by a suitable superposition of the natural hybrid modes. It has to be noted that despite the fact that those LP modes are no longer eigenfunctions of the fiber and therefore not matched for describing propagation effects, they can still be used to reconstruct the full field information since the built mode set is nonetheless complete and orthogonal. Figure 5.12 (a) and (f) show the reconstructed intensity and polarization distribution of the fiber

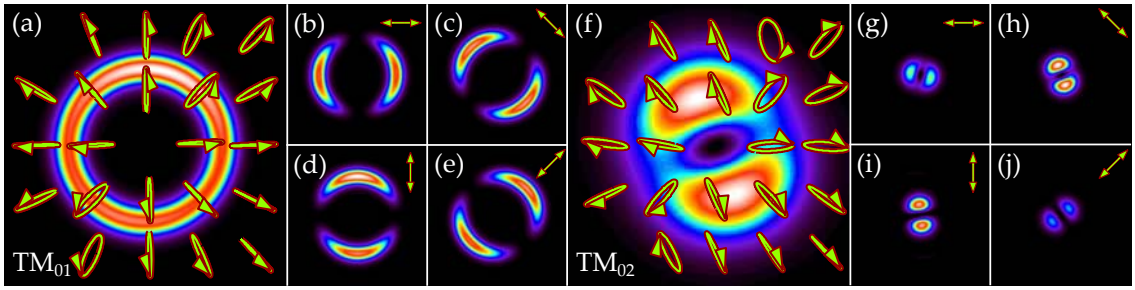

Figure 5.12: Image of the fiber output after injection of the radially polarized modes, (a) intensity and polarization distribution for TM_{01} excitation, (b)-(e) corresponding intensity distribution for various polarization orientation; (f) intensity and polarization distribution for TM_{02} excitation, (g)-(j) corresponding intensity distribution for various polarization orientations. Insets indicate the orientation of the polarizer.

output after TM_{01} and TM_{02} excitation, respectively. In case of the TM_{01} mode a nearly perfect radial polarization distribution can be observed, whereas the low modal crosstalk causes only some limited ellipticity of the local polarization states. In contrast, the polarization distribution after the TM_{02} excitation deviates notably from the expected radial one. In addition to the disturbed polarization distribution of the transmitted beam, the intensity distribution is no longer ring shaped as expected for a pure mode.

The comparison of both results for the TM_{01} and TM_{02} mode highlights the advantage of the ring-structure for the transmitted mode purity. The lower order modes, which are completely confined in the outer ring, preserve their propagation stability even at 784 nm operation wavelength with a mode purity of about 12 dB. In contrast, the mainly core guided higher order mode TM_{02} do not benefit by the ring structure and therefore show a high amount of mode coupling, resulting in a reduced mode purity of only 4.5 dB. However, the here observed mode purity of 12 dB for the TM_{01} mode is about two orders of magnitude lower as reported for the design wavelength at 1550 nm [66]. This indicates the occurrence of modal crosstalk within the mode group due to the reduced eigenvalue spacing corresponding to the shorter working wavelength.

Chapter Summary

This chapter dealt with the direct modal decomposition into the hybrid vector modes of an optical vortex fiber. At first the modal properties and field distributions of this fiber were determined and discussed. Afterwards, the concept of the q-plate as a non-uniform anisotropic wave plate was outlined and its capability to shape complex vector fields was shown. An extension of the previously described correlation filter method (Ch.2) for vector mode detection utilizing the additional capability of the q-plates was also introduced. In particular this new approach enabled to the first time the differentiation of vector modes with the same azimuthal but different radial order. In the last part the application of the developed vector mode creation and detection scheme was demonstrated for the characterization of the transmission properties of the vortex fiber. It could be shown that of the two guided radially polarized modes, only the TM_{01}, which was guided in the ring structure, was transmitted nearly without perturbations, resulting in a mode purity of 12 dB. In contrast, the core guided higher order TM_{02} mode was strongly distorted by crosstalk and only a mode purity of 4.5 dB was achievable. In conclusion, the investigated vortex fiber can be used for the transmission of radially polarized light beams at 784 nm in cases where the TM_{01} mode can be selectively excited.

6 | Conclusion

The main objective of this work was to develop a universally applicable modal decomposition technique to characterize light propagation in multi-mode fibers. To reach this aim, the correlation filter method was applied, modified, and extended to enable a complete modal analysis under arbitrary quasi monochromatic conditions, independent of the state of coherence or the kind of the underlying mode set.

Chapter 2 first introduced the mode picture in terms of hybrid and linear polarized eigenfunctions of optical fibers and discussed their principle properties and interrelations. In a second part of Ch. 2, the experimental principles for creation and decomposition of mode fields and their superpositions by holographic filter functions were outlined. Afterwards, the aforementioned techniques were applied for the investigation of scalar fiber beams in Ch. 3. It was shown that the effect of the fiber on light propagation can be characterized by multiple-input-multiple-output experiments and signal pre- or post-processing becomes possible by evaluation of the obtained fiber's transmission matrix. Additionally, the ability to decompose optical beams in arbitrary mode sets was used to investigate the overlap relation between free-space and step-index fiber modes which led to the high quality excitation of fiber modes direct by a digitally controlled solid-state laser source. Finally, a proof of principle realization of the first passively combined fiber–free-space link for modally multiplexed optical communication was performed.

In Ch. 4, the evaluation procedure of the correlation filter method was modified to enable the generalized decomposition and reconstruction of general partial coherent fiber beams. Therefore, additional interferometric filter functions were implemented which enabled the determination of the mutual modal degree of coherence. Besides the characterization of partial coherent fiber beams, the new

capability was used to investigate the effect of fiber propagation on the state of modal coherence. The measurement of the decreasing modal coherence with increasing propagation distance led to the determination of the modal coherence length caused by the modal dispersion in optical fibers. In further experiments, this approach can be used to determine the effective refractive index difference between modes by using a calibrated light source with a well known coherence length. Additionally, the effect of mode coupling onto the degree of modal coherence was investigated and a crosstalk induced increase of modal coherence could be demonstrated. Simultaneously, a decreasing degree of polarization of the coupled modes could be observed and quantified. This ability to control the degree of coherence of fiber beams by mode coupling might be useful to build light sources with adjustable coherence properties.

So far, only scalar mode sets were considered for the description of fiber beams. To overcome this limitation and enabling the direct investigation of light propagation in terms of the natural fiber modes, additional non-uniform anisotropic phase plates were incorporated into the correlation filter setup in Ch. 5. They enabled the performance of correlation analysis with respect to modes with a spatially varying polarization distribution, which was not possible before. The potential of this new vectorial correlation filter method was demonstrated by the quantitative determination of the mode transmission purity of a strong guiding vortex fiber. It was shown that the intended crosstalk free mode transmission properties of this fiber concept can be at least partially transferred from the design wavelength to significantly shorter wavelengths, which enables a plethora of possible applications besides fiber optical communication.

It should be emphasized at this point that the main objective to develop a universally applicable modal decomposition tool is completely achieved. With the further developed correlation filter method, now all kinds of quasi-monochromatic fiber beams can be modally resolved and characterized whiteout limitations regarding the state of coherence or the underlying modal basis. All the given examples demonstrate the versatility and the capabilities of the correlation filter method to investigate fiber beams and to characterize the impact of fiber propagation on the light field.

Bibliography

[1] D. J. Richardson, "Filling the light pipe," Science **330**, 327–328 (2010).

[2] J. Nilsson and D. N. Payne, "High-power fiber lasers," Science **332**, 921–922 (2011).

[3] N. Savage, "Supercontinuum sources," Nat Photon **3**, 114–115 (2009).

[4] J. Peterson and G. Vurek, "Fiber-optic sensors for biomedical applications," Science **224**, 123–127 (1984).

[5] G. Gagliardi, M. Salza, S. Avino, P. Ferraro, and P. De Natale, "Probing the ultimate limit of fiber-optic strain sensing," Science **330**, 1081–1084 (2010).

[6] N. Coluccelli, M. Cassinerio, B. Redding, H. Cao, P. Laporta, and G. Galzerano, "The optical frequency comb fibre spectrometer," Nat Commun **7**, 12995 (2016).

[7] T. Cizmar and K. Dholakia, "Exploiting multimode waveguides for pure fibre-based imaging," Nat Commun **3**, 1027 (2012).

[8] H. Defienne, M. Barbieri, I. A. Walmsley, B. J. Smith, and S. Gigan, "Two-photon quantum walk in a multimode fiber," Sci Adv **2**, E1501054 (2016).

[9] D. Gloge, "Weakly guiding fibers," Appl. Opt. **10**, 2252–2258 (1971).

[10] M. D. Feit and J. A. Fleck, "Light propagation in graded-index optical fibers," Appl. Opt. **17**, 3990–3998 (1978).

[11] B. Shalaby, V. Kermene, D. Pagnoux, A. Desfarges-Berthelemot, A. Barthelemy, A. Popp, M. Abdou Ahmed, A. Voss, and T. Graf, "19-cores yb-fiber laser with mode selection for improved beam brightness," Applied Physics B: Lasers and Optics **100**, 859–864 (2010).

[12] P. Russell, "Photonic crystal fibers," Science **299**, 358–362 (2003).

[13] J. C. Knight, "Photonic crystal fibres," Nature **424**, 847–851 (2003).

[14] A. Tünnermann, T. Schreiber, and J. Limpert, "Fiber lasers and amplifiers: an ultrafast performance evolution," Appl. Opt. **49**, F71–F78 (2010).

[15] D. J. Richardson, J. M. Fini, and L. E. Nelson, "Space-division multiplexing in optical fibres," Nat Photon **7**, 354–362 (2013).

[16] F. Poletti, N. V. Wheeler, M. N. Petrovich, N. Baddela, E. N. Fokoua, J. R. Hayes, D. R. Gray, Z. Lia, R. Slavik, and D. J. Richardson, "Towards high-capacity fibre-optic communications at the speed of light in vacuum," Nat Photon **7**, 279–284 (2013).

[17] C. Koebele, M. Salsi, D. Sperti, P. Tran, P. Brindel, H. Mardoyan, S. Bigo, A. Boutin, F. Verluise, P. Sillard, M. Astruc, L. Provost, F. Cerou, and G. Charlet, "Two mode transmission at 2x100Gb/s, over 40km-long prototype few-mode fiber, using LCoS-based programmable mode multiplexer and demultiplexer," Opt. Express **19**, 16593–16600 (2011).

[18] N. Bai, E. Ip, Y.-K. Huang, E. Mateo, F. Yaman, M.-J. Li, S. Bickham, S. Ten, J. L. nares, C. Montero, V. Moreno, X. Prieto, V. Tse, K. M. Chung, A. P. T. Lau, H.-Y. Tam, C. Lu, Y. Luo, G.-D. Peng, G. Li, and T. Wang, "Mode-division multiplexed transmission with inline few-mode fiber amplifier," Opt. Express **20**, 2668–2680 (2012).

[19] N. Bozinovic, Y. Yue, Y. Ren, M. Tur, P. Kristensen, H. Huang, A. E. Willner, and S. Ramachandran, "Terabit-scale orbital angular momentum mode division multiplexing in fibers," Science **340**, 1545–1548 (2013).

[20] J. Li, F. Ren, T. Hu, Z. Li, Y. He, Z. Chen, Q. Mo, and G. Li, "Recent progress in mode-division multiplexed passive optical networks with low modal crosstalk," Optical Fiber Technology **35**, 28–36 (2016).

[21] T. Eidam, C. Wirth, C. Jauregui, F. Stutzki, F. Jansen, H.-J. Otto, O. Schmidt, T. Schreiber, J. Limpert, and A. Tünnermann, "Experimental observations of

the threshold-like onset of mode instabilities in high power fiber amplifiers," Opt. Express **19**, 13218–13224 (2011).

[22] H.-J. Otto, F. Stutzki, F. Jansen, T. Eidam, C. Jauregui, J. Limpert, and A. Tünnermann, "Temporal dynamics of mode instabilities in high-power fiber lasers and amplifiers," Opt. Express **20**, 15710–15722 (2012).

[23] A. V. Smith and J. J. Smith, "Steady-periodic method for modeling mode instability in fiber amplifiers," Opt. Express **21**, 2606–2623 (2013).

[24] C. Jauregui, H.-J. Otto, S. Breitkopf, J. Limpert, and A. Tünnermann, "Optimizing high-power yb-doped fiber amplifier systems in the presence of transverse mode instabilities," Opt. Express **24**, 7879–7892 (2016).

[25] T. Kaiser, D. Flamm, S. Schröter, and M. Duparré, "Complete modal decomposition for optical fibers using CGH-based correlation filters," Opt. Express **17**, 9347–9356 (2009).

[26] C. Schulze, D. Naidoo, D. Flamm, O. A. Schmidt, A. Forbes, and M. Duparré, "Wavefront reconstruction by modal decomposition," Opt. Express **20**, 19714–19725 (2012).

[27] C. Schulze, S. Ngcobo, M. Duparré, and A. Forbes, "Modal decomposition without a priori scale information," Opt. Express **20**, 27866–27873 (2012).

[28] D. Flamm, C. Schulze, R. Brüning, O. A. Schmidt, T. Kaiser, S. Schröter, and M. Duparré, "Fast M^2 measurement for fiber beams based on modal analysis," Appl. Opt. **51**, 987–993 (2012).

[29] C. Schulze, A. Lorenz, D. Flamm, A. Hartung, S. Schröter, H. Bartelt, and M. Duparré, "Mode resolved bend loss in few-mode optical fibers," Opt. Express **21**, 3170–3181 (2013).

[30] C. Schulze, A. Dudley, D. Flamm, M. Duparré, and A. Forbes, "Measurement of the orbital angular momentum density of light by modal decomposition," New J. Phys. **15**, 073025 (2013).

[31] A. E. Siegman, *Lasers* (University Science Books, 1986).

[32] M. Born and E. Wolf, *Principles of Optics* (Pergamon Press, 1991), 6th ed.

[33] J. Durnin, "Exact solutions for nondiffracting beams. i. the scalar theory," J. Opt. Soc. Am. A **4**, 651–654 (1987).

[34] M. A. Bandres and J. Gutiérrez-Vega, "Ince gaussian beams," Opt. Lett. **29**, 144–146 (2004).

[35] A. W. Snyder and J. D. Love, *Optical Waveguide Theory* (Chapman & Hall, 1996).

[36] P. S. Russell, "Photonic-crystal fibers," J. Lightwave Technol. **24**, 4729–4749 (2006).

[37] J. D. Joannopoulos, S. G. Johnson, J. N. Winn, and R. D. Meade, *Photonic Crystals: Molding the Flow of Light* (Princeton University Press, 2008), 2nd ed.

[38] A. Yariv, *Optical Electronics in Modern Communications*, The Oxford series in electrical engineering (Oxford University Press, 1997), 5th ed.

[39] U. Röpke, H. Bartelt, S. Unger, K. Schuster, and J. Kobelke, "Two-dimensional high-precision fiber waveguide arrays for coherent light propagation," Opt. Express **15**, 6894–6899 (2007).

[40] T. P. White, B. T. Kuhlmey, R. C. McPhedran, D. Maystre, G. Renversez, C. M. de Sterke, and L. C. Botten, "Multipole method for microstructured optical fibers. I. Formulation," J. Opt. Soc. Am. B **19**, 2322–2330 (2002).

[41] B. T. Kuhlmey, T. P. White, G. Renversez, D. Maystre, L. C. Botten, C. M. de Sterke, and R. C. McPhedran, "Multipole method for microstructured optical fibers. II. Implementation and results," J. Opt. Soc. Am. B **19**, 2331–2340 (2002).

[42] A. B. Fallahkhair, K. S. Li, and T. E. Murphy, "Vector finite difference modesolver for anisotropic dielectric waveguides," J. Lightwave Technol. **26**, 1423–1431 (2008).

[43] F. Brechet, J. Marcou, D. Pagnoux, and P. Roy, "Complete analysis of the characteristics of propagation into photonic crystal fibers, by the finite element method," Optical Fiber Technology **6**, 181 – 191 (2000).

[44] H. Uranus and H. Hoekstra, "Modelling of microstructured waveguides using a finite-element-based vectorial mode solver with transparent boundary conditions," Opt. Express **12**, 2795–2809 (2004).

[45] J. P. Kirk and A. L. Jones, "Phase-only complex-valued spatial filter," J. Opt. Soc. Am. **61**, 1023–1028 (1971).

[46] J. A. Davis, D. M. Cottrell, J. Campos, M. J. Yzuel, and I. Moreno, "Encoding amplitude information onto phase-only filters," Appl. Opt. **38**, 5004–5013 (1999).

[47] V. Soifer, *Methods for Computer Design of Diffractive Optical Elements* (John Wiley & Sons, 2002).

[48] V. Arrizón, U. Ruiz, R. Carrada, and L. A. González, "Pixelated phase computer holograms for the accurate encoding of scalar complex fields," J. Opt. Soc. Am. A **24**, 3500–3507 (2007).

[49] W. H. Lee, "Sampled Fourier transform hologram generated by computer," Appl. Opt. **9**, 639–643 (1970).

[50] C. B. Burckhardt, "A simplification of Lee's method of generating holograms by computer," Appl. Opt. **9**, 1949–1949 (1970).

[51] G. N. Watson, *A treatise on the Theory of Bessel functions* (Cambridge University Press, 1995).

[52] P. A. Bélanger and C. Paré, "Optical resonators using graded-phase mirrors," Opt. Lett. **16**, 1057–1059 (1991).

[53] I. A. Litvin and A. Forbes, "Intra–cavity flat–top beam generation," Opt. Express **17**, 15891–15903 (2009).

[54] I. A. Litvin and A. Forbes, "Gaussian mode selection with intracavity diffractive optics," Opt. Lett. **34**, 2991–2993 (2009).

[55] J. R. Leger, D. Chen, and Z. Wang, "Diffractive optical element for mode shaping of a nd:yag laser," Opt. Lett. **19**, 108–110 (1994).

[56] J. R. Leger, D. Chen, and K. Dai, "High modal discrimination in a nd:yag laser resonator with internalphase gratings," Opt. Lett. **19**, 1976–1978 (1994).

[57] A. J. Caley, M. J. Thomson, J. Liu, A. J. Waddie, and M. R. Taghizadeh, "Diffractive optical elements for high gain lasers with arbitrary output beam profiles," Opt. Express **15**, 10699–10704 (2007).

[58] I. A. Litvin, L. Burger, and A. Forbes, "Petal–like modes in porro prism resonators," Opt. Express **15**, 14065–14077 (2007).

[59] D. Naidoo, K. Aït-Ameur, M. Brunel, and A. Forbes, "Intra-cavity generation of superpositions of laguerre-gaussian beams," Applied Physics B: Lasers and Optics **106**, 683–690 (2012).

[60] J. Bourderionnet, A. Brignon, J.-P. Huignard, A. Delboulbé, and B. Loiseaux, "Spatial mode control of a diode-pumped nd:yag laser by an intracavity liquid-crystal light valve," Opt. Lett. **26**, 1958–1960 (2001).

[61] S. Ngcobo, I. Litvin, L. Burger, and A. Forbes, "A digital laser for on-demand laser modes," Nat Commun **4**, 2289 (2013).

[62] Arrizón, "Optimum on-axis computer-generated hologram encoded into low-resolution phase-modul ation devices," Opt. Lett. **28**, 2521–2523 (2003).

[63] J. W. Nicholson, A. D. Yablon, S. Ramachandran, and S. Ghalmi, "Spatially and spectrally resolved imaging of modal content in large-mode-area fibers," Opt. Express **16**, 7233–7243 (2008).

[64] D. N. Schimpf, R. A. Barankov, and S. Ramachandran, "Cross-correlated (C2) imaging of fiber and waveguide modes," Opt. Express **19**, 13008–13019 (2011).

[65] Y. Z. Ma, Y. Sych, G. Onishchukov, S. Ramachandran, U. Peschel, B. Schmauss, and G. Leuchs, "Fiber-modes and fiber-anisotropy characterization using low-coherence interferometry," Appl. Phys. B: Lasers Opt. **96**, 345–353 (2009).

[66] P. Gregg, M. Mirhosseini, A. Rubano, L. Marrucci, E. Karimi, R. W. Boyd, and S. Ramachandran, "Q-plates as higher order polarization controllers for orbital angular momentum modes of fiber," Opt. Lett. **40**, 1729–1732 (2015).

[67] L. Yan, R. Barankov, P. Steinvurzel, and S. Ramachandran, "Modal-weight measurements with fiber gratings," J. Lightwave Technol. **33**, 2784–2790 (2015).

[68] O. Shapira, A. F. Abouraddy, J. D. Joannopoulos, and Y. Fink, "Complete modal decomposition for optical waveguides," Phys. Rev. Let. **94**, 143902 (2005).

[69] R. Brüning, P. Gelszinnis, C. Schulze, D. Flamm, and M. Duparré, "Comparative analysis of numerical methods for the mode analysis of laser beams," Appl. Opt. **52**, 7769–7777 (2013).

[70] H. Lü, P. Zhou, X. Wang, and Z. Jiang, "Fast and accurate modal decomposition of multimode fiber based on stochastic parallel gradient descent algorithm," Appl. Opt. **52**, 2905–2908 (2013).

[71] Y. Li, J. Guo, L. Liu, T. Wang, and J. Shao, "Linear equations method for modal decomposition using intensity information," J. Opt. Soc. Am. A **30**, 2502–2509 (2013).

[72] M. Paurisse, L. Lévèque, M. Hanna, F. Druon, and P. Georges, "Complete measurement of fiber modal content by wavefront analysis," Opt. Express **20**, 4074–4084 (2012).

[73] F. K. Fatemi and G. Beadie, "Rapid complex mode decomposition of vector beams by common path interferometry," Opt. Express **21**, 32291–32305 (2013).

[74] M. A. Golub, A. M. Prokhorov, I. N. Sisakian, and V. A. Soifer, "Synthesis of spatial filters for investigation of the transverse mode composition of coherent radiation," Soviet Journal of Quantum Electronics **9**, 1866–1868 (1982).

[75] V. A. Soifer and M. Golub, *Laser Beam Mode Selection by Computer Generated Holograms* (CRC Press, 1994).

[76] L. Huang, S. Guo, J. Leng, H. Lü, P. Zhou, and X. Cheng, "Real-time mode decomposition for few-mode fiber based on numerical method," Opt. Express **23**, 4620–4629 (2015).

[77] R. Brüning, D. Flamm, C. Schulze, O. A. Schmid, and M. Duparré, "Comparison of two modal decomposition techniques," in "Proc. SPIE 8236, Laser Resonators, Microresonators, and Beam Control XIV," (2012), 82360I.

[78] C. Jollivet, D. Flamm, M. Duparré, and A. Schülzgen, "Detailed characterization of optical fibers by combining s^2 imaging with correlation filter mode analysis," Journal of Lightwave Technology **32**, 1068–1074 (2014).

[79] H. G. Berry, G. Gabrielse, and A. E. Livingston, "Measurement of the Stokes parameters of light," Appl. Opt. **16**, 3200–3205 (1977).

[80] Q. Zhan, "Cylindrical vector beams: from mathematical concepts to applications," Adv. Opt. Photon. **1**, 1–57 (2009).

[81] M. A. Ahmed, M. Haefner, M. Vogel, C. Pruss, A. Voss, W. Osten, and T. Graf, "High-power radially polarized Yb:YAG thin-disk laser with high efficiency," Opt. Express **19**, 5093–5103 (2011).

[82] D. Flamm, O. A. Schmidt, C. Schulze, J. Borchardt, T. Kaiser, S. Schröter, and M. Duparré, "Measuring the spatial polarization distribution of multimode

beams emerging from passive step-index large-mode-area fibers," Opt. Lett. **35**, 3429–3431 (2010).

[83] R. Paschotta, *Encyclopedia of Laser Physics and Technology* (Wiley-VCH, Berlin, 2008).

[84] T. Eidam, S. Hädrich, F. Jansen, F. Stutzki, J. Rothhardt, H. Carstens, C. Jauregui, J. Limpert, and A. Tünnermann, "Preferential gain photonic-crystal fiber for mode stabilization at high average powers," Opt. Express **19**, 8656–8661 (2011).

[85] J. P. Koplow, D. A. V. Kliner, and L. Goldberg, "Single-mode operation of a coiled multimode fiber amplifier," Opt. Lett. **25**, 442–444 (2000).

[86] D. Flamm, K.-C. Hou, P. Gelszinnis, C. Schulze, S. Schröter, and M. Duparré, "Modal characterization of fiber-to-fiber coupling processes," Opt. Lett. **38**, 2128–2130 (2013).

[87] A. D. Yablon, *Optical Fiber Fusion Splicing* (Springer, 2005).

[88] M. A. A. Neil, R. Juakaitis, M. J. Booth, T. Wilson, T. Tanaka, and S. Kawata, "Adaptive aberration correction in a two-photon microscope," J. Microsc. **200**, 105–108 (2000).

[89] S. Ramachandran, J. Fini, M. Mermelstein, J. Nicholson, S. Ghalmi, and M. Yan, "Ultra-large effective-area, higher-order mode fibers: a new strategy for high-power lasers," Laser & Photonics Reviews **2**, 429 – 448 (2008).

[90] S. V. Karpeev, V. S. Pavelyev, S. N. Khonina, N. L. Kazanskiy, A. V. Gavrilov, and V. A. Eropolov, "Fibre sensors based on transverse mode selection," J. Mod. Opt. **54**, 833–844 (2007).

[91] A. V. Newkirk, J. E. Antonio-Lopez, G. Salceda-Delgado, M. U. Piracha, R. Amezcua-Correa, and A. Schülzgen, "Multicore fiber sensors for simultaneous measurement of force and temperature," IEEE Photonics Technology Letters **27**, 1523–1526 (2015).

[92] J. Villatoro, A. Van Newkirk, E. Antonio-Lopez, J. Zubia, A. Schülzgen, and R. Amezcua-Correa, "Ultrasensitive vector bending sensor based on multicore optical fiber," Opt. Lett. **41**, 832–835 (2016).

[93] J. L. Rodgers and W. A. Nicewander, "Thirteen ways to look at the correlation coefficient," The American Statistician **42**, 59–66 (1988).

[94] H. Yoda, P. Polynkin, and M. Mansuripur, "Beam quality factor of higher order modes in a step-index fiber," J. Lightwave Technol. **24**, 1350 (2006).

[95] C. Schulze, A. Dudley, D. Flamm, M. Duparré, and A. Forbes, "Reconstruction of laser beam wavefronts based on mode analysis," Appl. Opt. **52**, 5312–5317 (2013).

[96] C. Schulze, A. Dudley, R. Brüning, M. Duparré, and A. Forbes, "Measurement of the orbital angular momentum density of bessel beams by projection into a laguerré gaussian basis," Appl. Opt. **53**, 5924–5933 (2014).

[97] R. Brüning, D. Flamm, S. S. Ngcobo, A. Forbes, and M. Duparré, "Rapid measurement of the fiber's transmission matrix," in "Proc. SPIE 9389, Next-Generation Optical Communication: Components, Sub-Systems, and Systems IV," (2015), 93890N-7.

[98] D. Flamm, "The modal transmission function of optical fibers," Ph.D. thesis, Friedrich Schiller University Jena (2013).

[99] J. Carpenter, B. J. Eggleton, and J. Schröder, "110x110 optical mode transfer matrix inversion," Opt. Express **22**, 96–101 (2014).

[100] D. Flamm, C. Schulze, D. Naidoo, S. Schröter, A. Forbes, and M. Duparré, "All-digital holographic tool for mode excitation and analysis in optical fibers," J. Lightwave Technol. **31**, 1023 –1032 (2013).

[101] R. Brüning, Y. Zhang, M. McLaren, M. Duparré, and A. Forbes, "Overlap relation between free-space laguerre gaussian modes and step-index fiber modes," J. Opt. Soc. Am. A **32**, 1678–1682 (2015).

[102] R. Brüning, S. Ngcobo, M. Duparré, and A. Forbes, "Direct fiber excitation with a digitally controlled solid state laser source," Opt. Lett. **40**, 435–438 (2015).

[103] J. Demas, L. Rishøj, and S. Ramachandran, "Free-space beam shaping for precise control and conversion of modes in optical fiber," Opt. Express **23**, 28531–28545 (2015).

[104] D. M. Spirit, A. D. Ellis, and P. E. Barnsley, "Optical time division multiplexing: systems and networks," IEEE Communications Magazine **32**, 56–62 (Dec. 1994).

[105] A. Banerjee, Y. Park, F. Clarke, H. Song, S. Yang, G. Kramer, K. Kim, and B. Mukherjee, "Wavelength-division-multiplexed passive optical network (wdm-pon) technologiesfor broadband access: a review [invited]," J. Opt. Netw. **4**, 737–758 (2005).

[106] C. Herard and A. Lacourt, "New multiplexing technique using polarization of light," Appl. Opt. **30**, 222–231 (1991).

[107] B. J. Puttnam, R. S. Luís, W. Klaus, J. Sakaguchi, J. M. D. Mendinueta, Y. Awaji, N. Wada, Y. Tamura, T. Hayashi, M. Hirano, and J. Marciante, "2.15 pb/s transmission using a 22 core homogeneous single-mode multi-core fiber and wideband optical comb," in "2015 European Conference on Optical Communication (ECOC)," (2015), PDP.3.1.

[108] D. Soma, K. Igarashi, Y. Wakayama, K. Takeshima, Y. Kawaguchi, N. Yoshikane, T. Tsuritani, I. Morita, and M. Suzuki, "2.05 peta-bit/s super-nyquist-wdm sdm transmission using 9.8-km 6-mode 19-core fiber in full c band," in "2015 European Conference on Optical Communication (ECOC)," (2015), PDP.3.2.

[109] E. Leitgeb, M. Gebhart, and U. Birnbacher, "Optical networks, last mile access and applications," Journal of Optical and Fiber Communications Reports **2**, 56–85 (2005).

[110] Q. Liu, C. Qiao, G. Mitchell, and S. Stanton, "Optical wireless communication networks for first- and last-mile broadband access[invited]," J. Opt. Netw. **4**, 807–828 (2005).

[111] H. Huang, G. Xie, Y. Yan, N. Ahmed, Y. Ren, Y. Yue, D. Rogawski, M. J. Willner, B. I. Erkmen, K. M. Birnbaum, S. J. Dolinar, M. P. J. Lavery, M. J. Padgett, M. Tur, and A. E. Willner, "100 tbit/s free-space data link enabled by three-dimensional multiplexing of orbital angular momentum, polarization, and wavelength," Opt. Lett. **39**, 197–200 (2014).

[112] K. Sasaki, N. Minato, T. Ushikubo, and Y. Arimoto, "First OCDMA experimental demonstration over free space and optical fiber link," in "OSA Technical Digest (CD)," (Optical Society of America, San Diego, California, 2008), OMR8.

[113] R. M. Sova, J. E. Sluz, D. W. Young, J. C. Juarez, A. Dwivedi, N. M. Demidovich III, J. E. Graves, M. Northcott, J. Douglass, J. Phillips, D. Driver, A. McClarin, and D. Abelson, "80 gb/s free-space optical communication demonstration between an aerostat and a ground terminal," in "Proc. SPIE 6304, Free-Space Laser Communications VI," (2006), 630414.

[114] R. Brüning, B. Ndagano, M. McLaren, S. Schröter, J. Kobelke, M. Duparré, and A. Forbes, "Data transmission with twisted light through a free-space to fiber optical communication link," Journal of Optics **18**, 03LT01 (2016).

[115] J. Kobelke, J. Bierlich, K. Wondraczek, C. Aichele, Z. Pan, S. Unger, K. Schuster, and H. Bartelt, "Diffusion and interface effects during preparation of all-solid microstructured fibers," Materials **7**, 6879 (2014).

[116] J. Carpenter, B. C. Thomsen, and T. D. Wilkinson, "Degenerate mode-group division multiplexing," J. Lightwave Technol. **30**, 3946–3952 (2012).

[117] F. Ferreira and M. Belsley, "Holographic spatial coherence analysis of a laser," Opt. Lett. **38**, 4350–4353 (2013).

[118] H. Laabs and B. Ozygus, "Excitation of Hermite Gaussian modes in end-pumped solid-state lasers via off-axis pumping," Optics & Laser Technology **28**, 213 – 214 (1996).

[119] C. Schulze, R. Brüning, S. Schröter, and M. Duparré, "Mode coupling in few-mode fibers induced by mechanical stress," J. Lightwave Technol. **33**, 4488–4496 (2015).

[120] K. S. Youngworth and T. G. Brown, "Focusing of high numerical aperture cylindrical-vector beams," Opt. Express **7**, 77–87 (2000).

[121] W. Chen and Q. Zhan, "Numerical study of an apertureless near field scanning optical microscope probe under radial polarization illumination," Opt. Express **15**, 4106–4111 (2007).

[122] B. N. Tugchin, N. Janunts, A. E. Klein, M. Steinert, S. Fasold, S. Diziain, M. Sison, E.-B. Kley, A. Tünnermann, and T. Pertsch, "Plasmonic tip based on excitation of radially polarized conical surface plasmon polariton for detecting longitudinal and transversal fields," ACS Photonics **2**, 1468–1475 (2015).

[123] Q. Zhan, "Trapping metallic rayleigh particles with radial polarization," Opt. Express **12**, 3377–3382 (2004).

[124] Y. Zhao, Q. Zhan, Y. Zhang, and Y.-P. Li, "Creation of a three-dimensional optical chain for controllable particle delivery," Opt. Lett. **30**, 848–850 (2005).

[125] G. Milione, M. P. J. Lavery, H. Huang, Y. Ren, G. Xie, T. A. Nguyen, E. Karimi, L. Marrucci, D. A. Nolan, R. R. Alfano, and A. E. Willner, "4 x 20 gbit/s mode division multiplexing over free space using vector modes and a q-plate mode (de)multiplexer," Opt. Lett. **40**, 1980–1983 (2015).

[126] Q. Zhan, "Evanescent bessel beam generation via surface plasmon resonance excitation by a radially polarized beam," Opt. Lett. **31**, 1726–1728 (2006).

[127] M. A. Ahmed, A. Voss, M. M. Vogel, and T. Graf, "Multilayer polarizing grating mirror used for the generation of radial polarization in Yb:YAG thin-disk lasers," Opt. Lett. **32**, 3272–3274 (2007).

[128] S. Ramachandran and P. Kristensen, "Optical vortices in fiber," Nanophotonics **2**, 455–474 (2014).

[129] Z. Bomzon, G. Biener, V. Kleiner, and E. Hasman, "Radially and azimuthally polarized beams generated by space-variant dielectric subwavelength gratings," Opt. Lett. **27**, 285–287 (2002).

[130] L. Marrucci, C. Manzo, and D. Paparo, "Optical spin-to-orbital angular momentum conversion in inhomogeneous anisotropic media," Phys. Rev. Lett. **96**, 163905 (2006).

[131] L. Yan, P. Gregg, E. Karimi, A. Rubano, L. Marrucci, R. Boyd, and S. Ramachandran, "Q-plate enabled spectrally diverse orbital-angular-momentum conversion for stimulated emission depletion microscopy," Optica **2**, 900–903 (2015).

[132] S. K. Goyal, F. S. Roux, A. Forbes, and T. Konrad, "Implementing quantum walks using orbital angular momentum of classical light," Phys. Rev. Lett. **110**, 263602 (2013).

List of Figures

2.1 Intensity and polarization distributions of the lowest order hybrid modes of a step index fiber. . . . 12
2.2 Intensity and Phase distribution of the ten lowest order LP modes of a typical step index fiber. . . . 14
2.3 Interferometric relation between LP and hybrid modes to form the corresponding mode set. . . . 15
2.4 Coding principle of the phase-only coding technique for extra-cavity beam shaping. . . . 17
2.5 Working principle of the zero order coding technique for intra-cavity beam shaping. . . . 18
2.6 Scheme of the correlation filter principle. . . . 22
2.7 Working principle of the Lee coding technique. . . . 25
2.8 Correlation signals in the Fourier plane of a spatially multiplexed correlation filter. . . . 26
2.9 Superposition of different polarized LP modes. . . . 28

3.1 Model decomposition and field reconstruction of a step-index fiber beam. . . . 33
3.2 Principle scheme of the MIMO measurements for the determination of the fiber's transmission matrix. . . . 34
3.3 Setup for the determination of the fiber's transmission matrix. . . . 35
3.4 Fiber transfer matrix representing the linear transmission properties of a fiber with V$\approx$ 7. . . . 37
3.5 Signal correction by pre- and post processing applying the inverted transfer matrix. . . . 38

3.6 Setup for the determination of the size depending overlap between corresponding LG and LP modes. 44
3.7 Comparison between the theoretically and experimentally determined overlap relation between LG and the corresponding LP modes of a step index fiber with $V = 4.72$. 45
3.8 Size dependent overlap relations for modes with increasing radial and azimuthal order. 46
3.9 V parameter dependence of the overlap relation between the LP and corresponding LG modes. 47
3.10 Setup for the selective excitation of fiber modes by a intra-cavity beam shaping and its characterization. 48
3.11 Results of the intra-cavity beam shaping. 50
3.12 LP mode spectrum of the digital controlled laser cavity. 51
3.13 Refractive index profile of the parabolic graded index fiber. 55
3.14 Setup for the data transmission through a free-space to fiber communication link. 56
3.15 Transmission matrices of the combined free-space fiber link. 57
3.16 MDM scheme for the transmission of a gray scaled image of Einstein. 58

4.1 Example of modal superposition of LP_{01}, LP_{11e} and LP_{11o} modes with increasing degree of coherence 63
4.2 Example of a two mode interferogram with denoted measured visibility in comparison to the expected one for a coherent superposition 64
4.3 Setup for the determination of the modal degree of coherence. . . . 67
4.4 Partial coherent modal decomposition and reconstruction. 68
4.5 Simulation of the modal dispersion induced decrease of the degree of mutual coherence. 70
4.6 The dependency of the mutual degree of coherence on the fiber length. 72
4.7 Reconstructed intensity distributions of perturbed and unperturbed fiber. 75

5.1 Refractive index profile of the vortex fiber. 79

5.2 Effective refractive index spectrum of the vortex fiber. 80
5.3 Intensity and polarization distribution of some selected vortex fiber modes. 81
5.4 Example for the local orientation of the optical axis for q-plates. . . 83
5.5 Example of a written nano grating structure for a q-plate with charge $q = 1$ and $\alpha_0 = \frac{\pi}{4}$. 86
5.6 Setup for the generation of vector modes 87
5.7 Example of generated vector beams. 88
5.8 Principle working scheme of the vector mode correlation filter. . . . 90
5.9 Setup for the determination of the vector mode tranmission matrix. 92
5.10 Transmission matrix of the vortex fiber. 93
5.11 Transmission matrix of mode gropus of azimuthal order one. . . . 95
5.12 Image of the fiber output after injection of the radially polarized modes. 96

List of Own Publications

Peer-review Articles

1. Robert Brüning, Bienvenu Ndagano, Melanie McLaren, Siegmund Schöter, Jens Kobelke, Michael Duparré, Andrew Forbes, "Data transmission with twisted light through a freespace to fiber optical communication link," Journal of Optics 18, 03LT01 (2016)

2. Diego Guzman-Silva, Robert Brüning, Felix Zimmermann, Christian Vetter, Markus Gräfe, Matthias Heinrich, Stefan Nolte, Michael Duparré, Andrea Aiello, Marco Ornigotti, Alexander Szameit, "Demonstration of local teleportation using classical entanglement," Laser & Photonics Reviews 10, 317-321 (2016)

3. Christian Schulze, Robert Brüning, Siegmund Schröter, and Michael Duparré, "Mode Coupling in Few-Mode Fibers Induced by Mechanical Stress," J. Lightwave Technol. 33, 4488-4496 (2015)

4. Robert Brüning, Sandile Ngcobo, Michael Duparré, and Andrew Forbes, "Direct fiber excitation with a digitally controlled solid state laser source," Opt. Lett. 40, 435-438 (2015)

5. Bienvenu Ndagano, Robert Brüning, Melanie McLaren, Michael Duparré, and Andrew Forbes, "Fiber propagation of vector modes," Opt. Express 23, 17330-17336 (2015)

6. Robert Brüning, Yingwen Zhang, Melanie McLaren, Michael Duparré, and Andrew Forbes, "Overlap relation between free-space Laguerre Gaussian modes and step-index fiber modes," J. Opt. Soc. Am. A 32, 1678-1682 (2015)

7. C. Schulze, A. Dudley, R. Brüning, M. Duparré, A. Forbes, „Measurement of the orbital angular momentum density of Bessel beams by projection into a Laguerre-Gaussian basis“, Appl. Opt. 53, 5924-5933 (2014)

8. C. Schulze, J. Wilde, R. Brüning, S. Schröter, M. Duparré, "Measurement of the effective refractive index differences in multimode optical fibers based on modal decomposition", Opt. Lett. 39, 5810-5813 (2014)

9. R. Brüning, P. Gelszinnis, C. Schulze, D. Flamm and M. Duparré, „Comparative Analysis of Numerical Methods for the Mode Analysis of Laser Beams,“ Appl. Opt. 52, 7769-7777 (2013)

10. D. Flamm, C. Schulze, R. Brüning, O. Schmidt, T. Kaiser, S. Schröter, and M. Duparré, "Fast M2 measurement for fiber beams based on modal analysis," Appl. Opt. 51, 987-993 (2012).

11. O. Schmidt, C. Schulze, D. Flamm, R. Brüning, T. Kaiser, S. Schröter, and M. Duparré, "Realtime determination of laser beam quality by modal decomposition," Opt. Express 19, 6741-6748 (2011)

Conference Contributions

1. Robert Brüning, Daniel Flamm, Luise Lukas, Julian Lenz, Michael Duparré, "Determination of the physical fiber modes," Proc. SPIE 9389, Next-Generation Optical Communication: Components, Sub-Systems, and Systems IV, 93890O (2015)

2. Robert Brüning, Daniel Flamm, Sandile S. Ngcobo, Andrew Forbes, Michael Duparré, "Rapid measurement of the fiber's transmission matrix," Proc. SPIE 9389, Next- Generation Optical Communication: Components, Sub-Systems, and Systems IV, 93890N (2015)

3. Robert Brüning, Christian Schulze, Daniel Flamm, Andrew Forbes, Michael Duparré, "Characterization of OAM carrying beams by means of holo-

graphic correlation filters," Proc. SPIE 9379, Complex Light and Optical Forces IX, 93790K (2015)

4. Johannes Wilde, Christian Schulze, Robert Brüning, Michael Duparré, Siegmund Schröter, "Selective higher order fiber mode excitation using a monolithic setup of a phase plate at a fiber facet," Proc. SPIE 9343, Laser Resonators, Microresonators, and Beam Control XVII, 93431P (2015)

5. R. Brüning, D. Flamm, C. Schulze, O.Schmidt, M. Duparré, „Comparison of two modal decomposition techniques“, Proc. SPIE 8236, Laser Resonators, Microresonators, and Beam Control XIV, 82360I (2012);

Danksagung

Am Ende meiner Arbeit ist es mir ein Anliegen und eine Freude, all jenen meinen Dank auszusprechen, die mich während der Entstehung dieser Arbeit maßgeblich unterstützt haben. Beginnen möchte ich dabei mit Herrn Professor Dr. Richard Kowarschik, an dessen Institut ich die Möglichkeit erhielt diese Arbeit zu entwickeln. Auch nach seiner Emeritierung setzte er sich dafür ein, dass ich meine begonnene Dissertaion am Institut für Angewandte Optik erfolgreich beenden konnte.

Meinen besonderen Dank möchte ich Herrn Dr. Michael Duparré aussprechen. Er war mir während meine gesamten Zeit in seiner Arbeitsgruppe ein herausragender Betreuer und Mentor, der mir stets mit hilfreichen Diskussionen und Ratschlägen zur Seite stand. Dabei genoss ich stets ein großes Maß an persönlicher Freiheit und Vertrauen bei der Ausgestaltung und Verfolgung meiner Forschungsschwerpunkte, was mir ein völlig selbständiges wissenschaftliches Arbeiten ermöglichte. Ihm verdanke ich zudem die Möglichkeit, an internationalen Tagungen teilzunehmen und meine Ergebnisse zu präsentieren und zu publizieren. Besonders dankbar bin ich für die Ermöglichung meiner Auslandsaufenthalte, während derer ich wertvolle Erfahrungen in fremder Umgebung sammeln konnte.

Meinen ehemaligen Kollegen, den Herren Dr. Daniel Flamm und Dr. Christian Schulze, möchte ich an dieser Stelle dafür danken mich in das Thema der Modenanalyse eingeführt und damit den Grundstein für meinen eigenen Beitrag zu diesem Thema gelegt zu haben. Die vielfältigen Diskussionen und die gemeinsamen Arbeiten waren stets Quell neuer Inspiration und Motivation beim Identifizieren und Lösen neuer Probleme.

Herzlich danken möchte ich Herrn Dr. Sigmund Schröter und Herrn Rüdiger Pöhlmann vom Leibniz Institut für Photonische Technologie in Jena für die Herstellung der hochwertigen Amplitudenhologramme, welche ein wesentliches

Messwerkzeug meiner Arbeit darstellten und diese somit in der vorliegenden Form erst ermöglichten. Herrn Dr. Jens Kobelke, ebenfalls vom Leibniz Institut für Photonische Technologie in Jena, möchte ich für die Herstellung einer speziellen Faser danken, welche mir interessante Experimente ermöglichte. Ebenfalls zu Dank verpflichtet bin ich Herrn Felix Zimmermann vom Institut für Angewandte Physik für die Herstellung von speziellen Phasenelementen, die wesentlich zum Fortschritt meiner Themenstellung beigetragen haben.

Professor Dr. Andrew Forbes vom CSIR, National Laser Center Pretoria, und der School of Physics, Universtity of the Witwatersrand Johannesburg, gebührt mein Dank für die exzellente Betreuung während meiner Aufenthalte in Südafrika und die Möglichkeit, wesentliche Teile meiner Arbeit in seinen Laboren realisieren zu können. In diesem Zusammenhang möchte ich auch den vielen Kollegen in Pretoria und Johannesburg danken, welche mich direkt und indirekt im Labor oder bei vielfältigen Diskussionen unterstützt haben. Insbesondere seien hier genannt Dr. Melanie McLaren, Bienvenu Ndagano, Dr. Darryl Naidoo, Dr. Angela Dudley, Dr. Yingwen Zhang und Dr. Sandile Ngcobo.

Danken möchte ich auch Herrn Thomas Kaiser, Frau Bayarjargal Narantsatsralt und Dr. Norik Janunts für die gemeinsame Arbeit an speziellen Fasern, welche zu einer wesentlichen Weiterentwicklung meiner Themenstellung führte.

Professor Alexander Szameit, Dr. Marco Ornigotti und Diego Guzman-Silva danke ich für die Zusammenarbeit während unseres gemeinsamen Projektes und für die Möglichkeit, meine Messtechnik in einem neuen Kontext einsetzen zu können.

Meinen Kollegen Eugene Wong und Andreas Stark danke ich für das angenehme Arbeitsklima am Insitut und vor allem für das aufmerksame Korrekturlesen meiner Arbeit. Dankbar bin ich der Graduiertenakademie der Universität Jena, mir ein dreijähriges Promotionsstipendium gewährt zu haben.

Abschließend geht ein besonderer Dank an meine Frau Christiane Brüning für ihre immerwährende Unterstützung, ihr Verständnis und ihre Geduld während meiner gesamten Promotion. Ohne ihren Rückhalt wäre meine Arbeit in dieser Form nicht möglich gewesen.

Curriculum vitae

Personal information	
Surename	Brüning
First name	Robert
Date of birth	10.08.1988
Place of birth	Jena
School education	
1995-1999	Elementary school "An der Ringwiese", Jena
1999-2007	Secondary school (Gymnasium) "Ernst-Abbe-Gymnasium", Jena
June 2007	Abitur
Course of studies	
2008-2011	Study of Physics at the Friedrich Schiller University Jena
2011	Bachelor of Science ("Modal field characterization of LMA fibers using a phase retrieval algorithm")
2011-2013	Study of Physics at the Friedrich Schiller University Jena
2013	Master of Science ("Characterization of OAM carrying beams by means of holographic correlation filters")

Doctoral studies

2013-2016	Doctoral studies at the Institute of Applied Optics of the Friedrich Schiller University Jena with the topic "Characterization of Laser Light Propagation in Fibers using Optical Correlation Filters"
January 2014	Grant of a scholar ship "Landesgraduiertenstipendium" given by the Graduate Academy of the University of Jena
February-March 2014	Research stay at the National Laser Center, Council for Scientific and Industrial Research, Pretoria, South Africa
August/December 2014	Research stay at the Institute of Applied Physics, Friedrich Schiller University Jena, Germany
April-May 2015	Research stay at the School of Physics, University of the Witwatersrand, Johannesburg, South Africa

Professional experiences

December 2007-January 2009	Assistant at the Fraunhofer Institute for Applied Optics and Precisions Engineering
2009-2013	Employment as a student researcher at the Friedrich-Schiller University Jena, area of responsibility: correction of exercises
October 2010	Teaching at the Friedrich Schiller University Jena: holding the seminar "Pre-sessional mathematics course"

2010-2013	Employment as a student researcher at the Institute of Applied Optics of the Friedrich Schiller University Jena, area of responsibility: characterization of laser beams by holographic optical methods
February-April 2012	Employment as student researcher at the Institute for Optics and Quantum Electronics of the Friedrich Schiller University Jena, area of responsibility: Laser driven proton acceleration
2014-2015	Teaching at the Friedrich Schiller University Jena: holding the seminar "Experimental Physics 2" (summer term 2014) and "Optic and Waves" (summer term 2015)

Jena, 29. März 2017 Robert Brüning, M.Sc.

Ehrenwörtliche Erklärung

Ich erkläre hiermit ehrenwörtlich, dass ich die vorliegende Arbeit selbstständig, ohne unzulässige Hilfe Dritter und ohne Benutzung anderer als der angegebenen Hilfsmittel und Literatur angefertigt habe. Die aus anderen Quellen direkt oder indirekt übernommenen Daten und Konzepte sind unter Angabe der Quelle gekennzeichnet. Bei der Auswahl und Auswertung folgenden Materials haben mir nachstehend aufgeführte Personen in der jeweils beschriebenen Weise unentgeltlich geholfen:

1. Bernd Höfer: Durchführung der Messung des Brechungsindexprofils dargestellt in Abbildung 3.13 (a), S.55

2. Dr. Johannes Nold: Durchführung der Messung des Brechungsindexprofils dargestellt in Abbildung 5.1, S. 79

3. Felix Zimmer: Durchführung der REM Messung dargestellt in Abbildung 5.5 (a), S. 86

Weitere Personen waren an der inhaltlich-materiellen Erstellung der vorliegenden Arbeit nicht beteiligt. Insbesondere habe ich hierfür nicht die entgeltliche Hilfe von Vermittlungs- bzw. Beratungsdiensten (Promotionsberatern oder anderer Personen) in Anspruch genommen. Niemand hat von mir unmittelbar oder mittelbar geldwerte Leistungen für Arbeiten erhalten, die im Zusammenhang mit dem Inhalt der vorgelegten Dissertation stehen. Die Arbeit wurde bisher weder im Innoch im Ausland in gleicher oder ähnlicher Form einer anderen Prüfungsbehörde vorgelegt. Die geltende Promotionsordnung der Physikalisch-Astronomischen Fakultät is mir bekannt. Ich versichere ehrenwörtlich, dass ich nach bestem Wissen und Gewissen die reine Wahrheit gesagt und nichts verschwiegen habe.

Jena, 29. März 2017 Robert Brüning, M.Sc.